

University of Alberta

RELATIVISTIC SELF-FOCUSING, MAGNETIC FIELD GENERATION
AND PARTICLE ACCELERATION IN UNDERDENSE PLASMAS

by

Neda Naseri

A thesis submitted to the Faculty of Graduate Studies and Research
in partial fulfillment of the requirements for the degree of

Doctor of Philosophy

Department of Physics

© Neda Naseri

Fall 2010
Edmonton, Alberta

Permission is hereby granted to the University of Alberta Libraries to reproduce single copies of this thesis and to lend or sell such copies for private, scholarly or scientific research purposes only. Where the thesis is converted to, or otherwise made available in digital form, the University of Alberta will advise potential users of the thesis of these terms.

The author reserves all other publication and other rights in association with the copyright in the thesis and, except as herein before provided, neither the thesis nor any substantial portion thereof may be printed or otherwise reproduced in any material form whatsoever without the author's prior written permission.

Examining Committee

Wojciech Rozmus, Physics

Sharon Morsink, Physics

Richard Sydora, Physics

Robert Fedosejevs, Electrical and Computer Engineering

Denis Pesme, Physics, Ecole Polytechnique, France

ABSTRACT

In this thesis the following problems are studied:

1-Relativistic self-focusing and channelling of intense laser pulses have been studied in underdense plasma using 2D PIC simulations, for different laser powers and plasma densities. Analytical solutions for the stationary evacuated channels have been recovered in PIC simulations. It is shown that otherwise stable channels can accelerate electrons due to surface waves on the walls of the channels. Relativistic filaments with finite electron density are unstable to transverse modulations which lead in the nonlinear stage to the break-up of laser pulses into independent filaments.

2-Although 3D simulations are limited, they are more realistic. Azimuthal stability of the laser pulses in interaction with underdense plasma can only be studied in 3D geometry. Relativistic self-focusing and channelling of intense laser pulses have been studied in underdense plasma using 3D PIC simulations, for different laser powers and plasma densities. Analytical solutions for the stationary evacuated channels and ring structure have been recovered in PIC simulations. The stability of ring structure due to azimuthal perturbations has been studied both in theory and in simulations. The gain length of such instability is smaller at higher densities ($> 0.1n_{cr}$). It is shown that the azimuthal perturbation can break up the azimuthal symmetry of the laser pulse.

3-Working with circularly polarized laser pulses, gave us a motivation to study Inverse Faraday Effect in interaction of circularly polarized laser pulses with

plasma. Axial magnetic field generation by intense circularly polarized laser beams in underdense plasmas has been studied with 3D particle-in-cell (PIC) simulations and by means of theoretical analysis. The source of azimuthal nonlinear currents and of the axial magnetic field depends on the transverse inhomogeneities of the electron density and laser intensity. The fields reach maximum strength of several tens of MG for laser pulses undergoing relativistic self-focusing and channelling in moderately relativistic regime.

4-Electron wakefield acceleration was studied in support of the experiment which was carried on using 7 TW laser beam at Canadian Advanced Laser Light source facility. 2D simulations were performed to study this problem. The energy the electrons gained in the process was peaked at 20-30 MeV close to the experimental results.

ACKNOWLEDGMENTS

I offer my regards to all of those who supported me in any respect. First and foremost I want to thank my supervisor Wojciech Rozmus. I appreciate all his contributions of time, ideas, and funding to make my Ph.D. experience productive and stimulating.

My special thanks go to Valery Yu. Bychenkov. I had the pleasure of working with him on inverse Faraday effect in interaction of circularly polarized laser pulses with underdense plasmas.

During this work I have collaborated with many colleagues for whom I have great regard, Robert Fedosejevs and his group in the Department of Electrical and Computer Engineering.

Special thanks to my supervisory committee, Sharon Morsink, Richard Sydora, Robert Fedosejevs and my external examiner Denis Pesme for reading my thesis and for their useful comments.

I would also like to thank James McKinnon which his help made computational part of the work easier, Dimitry Romanov and specially Konstantin Popov, for their help with particle in cell codes and Jon Johanson for letting me use their facility.

I wish to thank my parents for their constant love and support and encouragement in all my life. Finally, I wish to express my gratitude to my husband Abdi for his continuous moral support.

Contents

Table of Contents	vii
List of Figures	x
1 Introduction	1
1.1 Relativistic Self-Focusing	3
1.2 Magnetic Field Generation by Circularly Polarized Laser Pulses in Underdense Plasmas	8
1.3 Laser-Plasma Accelerators	12
1.4 Thesis Outline	15
2 Self-Channelling of Relativistic Laser Pulses in Large-Scale Underdense Plasmas	23
2.1 Introduction	23
2.2 Relativistic Self-Focusing - theory and simulations	27
2.2.1 Theoretical Model	28
2.2.2 RSF - Stationary Solution	30
2.2.3 PIC Simulations	31
2.2.4 Stability of RSF Filaments	34

2.3	Channelling of the Laser Pulse	36
2.3.1	Analytical Theory	36
2.3.2	PIC Simulations	38
2.3.3	Surface Waves Excitation	43
2.3.4	High Density Regime	49
2.4	Conclusions	51
3	Self-Focusing, Channeling and Particle Acceleration by Relativistic Laser Pulses in 3D Geometry	57
3.1	Introduction	57
3.2	A Theoretical Model	59
3.3	Channelling	61
3.4	Single Fully Evacuated Channels-PIC Simulation Results	63
3.5	Surface Wave Excitation	70
3.6	Ring Structure	75
3.6.1	Ring Structure- Theoretical Review	75
3.7	Ring Structure-Simulations	77
3.8	Stability Analysis	78
3.8.1	Stability Analysis-Single Channel	78
3.8.2	Stability Analysis (symmetric perturbation)-Ring Structure	80
3.8.3	Stability Analysis (asymmetric perturbation)-Ring Structure	82
3.9	Evolution of Laser Pulses at Higher Plasma Densities	83
3.10	Conclusions	88
4	Axial Magnetic Field Generation in Interaction of Intense Circularly Polarized Laser with Underdense Plasma	94

4.1	A Model of the IFE	98
4.2	3D Simulation Results	103
4.2.1	A Single Channel Self-Focusing	104
4.2.2	Ring Structure of the Laser Pulse	111
4.2.3	Channelling Regime	114
4.2.4	Time Evolution of the Magnetic Field	116
4.3	Discussion and Summary	120
5	Quasi-Monoenergetic Electron Beams Generated From 7TW Laser Pulses in N₂ and He Gas Targets	126
5.1	Introduction	126
5.2	Experiment	128
5.3	Results and Analysis	129
5.4	Modelling of the Results	137
5.5	Conclusion	146
6	Summary	150
6.1	Channeling in 2D Slab Geometry	150
6.2	Channeling in 3D	151
6.3	Magnetic Field Generation	152
6.4	Electron Acceleration	152

List of Figures

2.1	Contour plot of laser intensity (a). Comparison between analytical solution and simulation result (b), intensity calculated from analytical solution (solid curve) and laser intensity taken from transverse cut in simulation box (dashed curve). Contour plot of electron charge density normalized by n_c after propagating 1976 fs (c). Electron density calculated from analytical solution (solid-curve) and electron density taken from transverse cut in simulation box (dashed curve) (d)-straight lines show the position of the cut in the simulation box.	32
2.2	Dimensionless power ($\int_{-\infty}^{\infty} a^2 dy$) as a function of η . Graph shows the locus of stationary RSF solutions. The single point corresponds to the stationary PIC simulation solution from Fig. 2.1. The location of this point was calculated from the numerical results.	33
2.3	Gain coefficient (Γ) as a function of wavenumber for $\eta = 1.3$ (solid curve), 1.4 (dashed curve) and 1.49 (dotted curve).	35
2.4	Schematic graph of analytical single channel solution, showing intensity distribution (solid curve) and electron density normalized by n_0 (dashed-curve).	38

-
- 2.5 Solid line shows the exact analytical solution and circles show the simulation results for one channel. Numbers 1 and 2 corresponds to two simulations illustrated in Sec. 2.3.2. 39
- 2.6 (Color online) Contours of laser intensity (a,c) and electron charge density (b,d) normalized by n_c for $t=1411$ fs and $t=2540$ fs. Solid curve in (e) shows the analytical solution of P/Pch vs full channel width y in μm for corresponding plasma density. The triangle shows the input parameters: laser power and FWHM of the laser intensity and the triangle is the calculated power and channel width taken from transverse cut at $x = 408\mu m, t=2540$ fs. 40
- 2.7 Lineouts of laser intensity and electron density normalized by N_0 along transverse direction (cut at $x = 408\mu m, t=2540$ fs). Solid curves show the exact analytical solutions and dashed curves are calculated laser intensity and electron density taken from transverse cut in simulation box. 42
- 2.8 Contours of laser intensity (a,c) and electron charge density (b,d) normalized by n_c for $t=1693$ fs and $t=2823$ fs. Solid curve in (e) shows the P/Pch vs full channel width y in μm for corresponding plasma density. The star shows the input parameters: laser power and FWHM of the laser intensity and the triangle is the calculated power and channel width taken from transverse cut at $x = 200\mu m, t = 1693fs$ 43

2.9	Solid line shows the input intensity of the laser and the dash-dotted line taken from a transverse cut ($x = 200\mu m, t = 1693fs$) in simulation box at showing the intensity of the laser in plasma. The dashed curve is the electron charge density taken from the same cut, clearly shows the evacuated channel.	44
2.10	(Color online) Longitudinal momentum of electrons in units of mc in $x - y$ plane for $t=847$ fs (a) and longitudinal momentum of electrons in units of mc averaged over x in transverse direction at $t=1695$ fs (b).	49
2.11	P/P_{ch} vs channel width y_d in μm for plasma densities $0.001n_{cr}$ (dash-dotted curve), $0.01n_{cr}$ (dashed curve) and $0.1n_{cr}$ (solid curve).	51
2.12	(Color online) Contour plot of laser intensity at $t=846$ fs (a) and Lineouts of laser intensity along transverse direction at $t=560$ fs ($x=119\mu m$,dashed curve) and $t=846$ fs ($x=181\mu m$) (b).	52
2.13	(Color online) Contour plots of laser intensity at $t=1411$ fs and 2540 fs. Plots show filamentation and bending of the laser light.	53
3.1	P/P_{cr} as a function of evacuated channel radius in units of $[k_L\sqrt{n_0}]^{-1}$ (calculated from theoretical model). Points show the simulation results (Fig.1-a). P/P_{cr} as a function of radius of evacuated channel in μm for plasma densities $0.1, 0.01, 0.005 n_{cr}$ (solid, dashed, dashed-dotted), calculated from theoretical model (Fig.1-b).	64
3.2	(Color online) Contours of laser intensity (a-c) and electron charge density (d-f) normalized to n_c	67

3.3	Comparison of theoretical solutions for laser intensity and electron density (solid curves) and simulation (dashed curves). Data taken from simulation in x-y plane at $x=90 \mu m$ ($t=633$ fs).	68
3.4	(Color online) Contours of laser intensity (a-c) and electron charge density (b-d) normalized to n_c	69
3.5	P/P_{cr} vs channel radius R in μm for plasma density $0.001n_{cr}$ (calculated from theoretical model). Star shows the initial FWHM of the laser intensity. Circle shows the calculated power and channel radius from simulation at $x = 90\mu m$ and $t=600$ fs.	70
3.6	(Color online) Contour plots of laser intensity (a-c) and electron charge density (d-f) normalized to n_c	71
3.7	(Color online) a,b) Contour plot of longitudinal momentum of electrons normalized to mc after propagating for $80 \mu m$ and $240 \mu m$ vs longitudinal direction x in μm . c) Contour plot of longitudinal momentum of electrons normalized to mc in the x-y plane.	72
3.8	Contour plots of a) longitudinal electric field of the surface waves b) transverse field E_y c) electron charge densities and d) laser intensities in xy plane at $t=1070$ fs.	74
3.9	Longitudinal (solid) and transverse (dashed) electric fields at $x = 297\mu m$ at $t=1070$ fs in xy plane.	75
3.10	Schematic graph showing the ring structure solution. The solid curve is the amplitude of the laser and the dashed curve is the electron density calculated for $\kappa = 0.3$	77
3.11	(Color online) Contour plots of laser intensity at different times.	78

3.12 (Color online) Contour plots of laser intensity (a) and electron charge density (b) in y - z plane at $x=95 \mu m$ and $t=400$ fs.	79
3.13 Amplitude of the laser (a) and electron density (b), solid curves are the theoretical solutions and dashed curves are taken from simulation in y - z plane at $x=95 \mu m$	80
3.14 The solid curve shows the power as a function of κ for single channel solution. The dashed curve shows the minimum power required to obtain ring structure as a function of κ . The total power as a function of κ for partial evacuation is shown in the inset.	81
3.15 Growth rate of transverse instability δ as a function of $\kappa - 1$ for ring structure $m = 1, 2$	83
3.16 (Color online) Contour plots of laser intensity after propagating for $300 \mu m$	84
3.17 (Color online) Contour plots of laser intensity in x - y plane at $t=464$ and 943 fs.	85
3.18 (Color online) Contour plots of laser intensity (a) and electron charge density (b) in yz plane at $x=17 \mu m$ and $t=133$ fs.	86
3.19 (Color online) contour plots of laser intensity showing in y - z plane, cuts at $x=21, 44$ and $70 \mu m$ at $t=580$ fs.	87

4.1	The radial distributions of axial magnetic field induced by interaction of circularly polarized laser pulse with plasma. Figure (a) shows the solutions obtained from Eq. (4.7) for wide channels ($k_p r_0 = 14.7$ and $k_p r_0 = 9$) and (b) shows the same solution for narrow channels ($k_p r_0 = 1.8$ and $k_p r_0 = 0.9$). The dashed curves in (a) and (b) correspond to expressions given by Eqs. (4.8) and (4.9) for $k_p r_0 = 14.7$ and $k_p r_0 = 0.9$, respectively.	102
4.2	Comparison of the solution to Eq. (4.7) (solid curve) with B-field profiles from Refs. [2, 6, 9](dotted curve) and results from Ref. [11] (dashed curve).	103
4.3	Quasi-static magnetic field calculated from probes located at $x = 85 \mu m$ in simulation box. Initial peak laser intensity is $4.7 \times 10^{19} W/cm^2$. The initial FWHM of the laser intensity is $5 \mu m$ and the background plasma density is $0.1 n_{cr}$. Circles and triangles correspond to $\lambda = \pm 1$	105
4.4	(Color online) Contour plots of a) laser intensity and b) electron charge density at $x=32 \mu m$ for a single channel.	106
4.5	Distributions of laser beam intensity and electron density across the propagation direction at $x=32 \mu m$ (the dashed curves) for a single channel self-focusing. Solid curves show the analytical functions used for fitting and later in the numerical solutions of Eq. (4.7).	107
4.6	Comparison of the quasi-static magnetic field profiles for a single channel obtained from PIC simulation (dots) and by the analytical IFE theory (solid curve) using the intensity and density profiles shown in Figs. 4.4 and 4.5.	107

4.7	Contour plots of a) laser intensity and b) electron charge density at $x=51 \mu m$ for a single channel self-focusing.	109
4.8	Distributions of laser beam intensity and electron density for single channel across propagation direction at $x=51 \mu m$ (the dashed curves). Solid curves show the analytical functions used for fitting.	110
4.9	Comparison of the quasi-static magnetic field profiles for a single channel self-focusing from PIC simulation (dots) and by the analytical IFE approach (solid curve) for the intensity and density profiles shown in Figs. 4.7 and 4.8.	110
4.10	Contour plots of a) laser intensity and b) electron charge density at $x=18 \mu m$ for ring structure case.	111
4.11	Distributions of laser beam intensity and electron density for ring structure across propagation direction at $x=18 \mu m$ (the dashed curves). Solid curves show the analytical functions used for fitting.	112
4.12	Comparison of the quasi-static magnetic field profiles for a case of the self-focusing leading to ring like field distribution obtained in PIC simulation (dots) and by the analytical theory of the IFE (solid curve) for the intensity and density profiles shown in Figs. 4.10 and 4.11. . .	113
4.13	(Color online) Contour plots of a) laser intensity and b) electron charge density at $x=30 \mu m$ for the cavitation regime.	114
4.14	Distributions of laser beam intensity and electron density for cavitation regime across propagation direction at $x=30 \mu m$ (the dashed curves). Solid curves show the analytical functions used for fitting.	115

4.15	Comparison of the quasi-static magnetic field profiles for the cavitation regime calculated from the PIC simulation (dots) and by the analytical IFE theory (solid curve) for the intensity and density profiles shown in Figs. 4.13 and 4.14.	116
4.16	a) Distributions of laser beam intensity and b) Distribution of electron density across propagation direction at $x=25 \mu\text{m}$ at $t=160 \text{ fs}$. Dashed curves represent the lineouts from simulation and solid curves show the analytical functions used for fitting. c) Comparison of the quasi-static magnetic field profiles obtained in PIC simulation (dots) and the analytical theory of the IFE (solid curve) for the intensity and density profiles shown in (a) and (b).	118
4.17	a) Distributions of laser beam intensity and b) Distribution electron density across propagation direction at $x=25 \mu\text{m}$ at $t=332 \text{ fs}$. Dashed curves represent the lineouts from simulation and solid curves show the analytical functions used for fitting. c) Comparison of the quasi-static magnetic field profiles obtained in PIC simulation (dots) and the analytical theory of the IFE (solid curve) for the intensity and density profiles shown in (a) and (b).	119
5.1	(Color online) Experimental set up.	128
5.2	Typical gas density profile measured by the interferometer when nitrogen gas backing pressure was 1000 psi. The gas jet was generated by a supersonic nozzle which was connected to the gas reservoir with its pressure adjustable from 100 to 1200 psi. The profile shows a steep gradient at the edge and a good flat top in the center of the jet. . . .	130

5.3	(color online) Energetic electron beam angular profile in the forward laser direction, integrated with 1640 shots when optimum conditions were adjusted to obtain mono-energetic electron beams. It was measured by RCF (inner frame) with nitrogen gas at about 360 psi and laser at the peak power. The laser beam forward direction is at 0° . . .	131
5.4	Typical single-shot electron energy distributions generated from nitrogen gas targets, measured by a Lanex fluorescent screen coupled to the electron spectrometer. Typical results are shown in (a) for pure N ₂ at 500 psi backing pressure and (b) for N ₂ with 10% H ₂ at 360 psi. An example of an infrequent very high electron energy shot is shown in (c) for N ₂ with 10% H ₂ at 360 psi. The dashed lines show the location and width of the lead slit used to define the spectrometer entrance aperture.	132
5.5	Typical single-shot electron energy distributions generated from helium gas targets, measured by a Lanex fluorescent screen coupled to the electron spectrometer. Typical results are shown in (a) and (b) for pure He at 900 psi backing pressure. An example of an infrequent very high electron energy shot is shown in (c) for He at 900 psi. The dashed lines show the location and width of the lead slit used to define the spectrometer entrance aperture.	133

- 5.6 Electron energy spectra obtained from the magnetic spectrometer images: (a) from a single shot in nitrogen with 10% hydrogen at 360 psi (Fig. 5.4(b)) integrated over 1.6 mrad of angular spread vertically, (b) from a single shot in helium at 900 psi (Fig. 5.5(a)) integrated over 10.6 mrad of angular spread vertically, (c) by averaging 26 shots from nitrogen gas with 10% hydrogen at 360 psi and 19 shots from helium gas at 900 psi, integrated over 19.2 mrad of angular spread vertically and (d) energy spectra from the shots shown in Figs. 5.4(c) and 5.5(c) showing the infrequent high energy electron bunches for nitrogen with 10% hydrogen and helium respectively integrated over 1.6 mrad of angular spread vertically. The response of the system has been calculated based on the camera response and fluorescence efficiency of the Lanex screen giving approximately one count generated in the image for each incident electron with energy from 10 MeV to 200 MeV. 135
- 5.7 Laser pulse from 2D3V PIC simulations at different time a) $t=180\text{fs}$, b) $t=425\text{fs}$ and c) $t=606\text{fs}$, and 2D spectra of the laser pulse at the same times (d-f). 138
- 5.8 Electron density (in units n_c) for different times: a) $t = 425 \text{ fs}$, b) $t = 790 \text{ fs}$, and c) $t = 1273 \text{ fs}$ 140

5.9	Lineouts of the longitudinal field, E_x , (dash-dot), laser field, E_y , (dotted) normalized to mc/e and electron charge density (solid line) normalized to critical density along the x axis at two different times: (a) at $t=849$ fs after propagating 180 microns in homogeneous plasma and (b) at $t=1091$ fs when the wake is already broken and trapped-electrons are accelerated in the accelerating field. The ponderomotive force also accelerates electrons in front of the laser pulse (snowplow).	142
5.10	Energy spectrum of electrons inside the first wakefield cavity for 2 different times: 1273 fs and 1335 fs.	143

Chapter 1

Introduction

Since the invention of the chirped pulse amplification technique in 1985 [1], there has been a constant progress in short pulse laser technology and applications. Pulse durations have come down from picoseconds to a few femtoseconds in durations and focused laser intensities have risen to $10^{21} - 10^{22} \text{ W/cm}^2$. High intensities of laser pulses can be several orders of magnitude above the relativistic threshold ($I_{rel}\lambda_L^2 \geq \zeta 1.37 \times 10^{18} \text{ W/cm}^2 \cdot \mu\text{m}^2$) where $\zeta = 1$ for linear and $\zeta = 2$ for circular polarization [2]. The relativistic threshold is reached when the dimensionless light amplitude $eA_L/m_e c^2 = 1$, i.e. when the quiver velocity of electron approaches c . Here λ_L is the laser wavelength, e and m_e are the electron charge and mass respectively, A_L is the wave vector potential and c is the speed of light in vacuum. Such large intensities have opened new research areas in laser plasma interactions. The physics of interaction of laser pulses with plasmas can be characterized by distinct physical processes depending on plasma density. In underdense targets where the electron density is less than the critical density laser pulses can penetrate and nonlinearly couple with a plasma while in overdense targets where electron density is larger

than the critical density, laser interaction takes place in the narrow region of the skin layer. When laser pulses are at intensities $10^{18} - 10^{21} \text{ W/cm}^2$ the interaction physics is dominated by nonlinear processes such as electron acceleration, self-focusing and channelling of the laser pulse and magnetic field generation, to list just a few.

This thesis is devoted to the interaction of intense laser pulses with underdense plasmas based on three published papers (Chapters 2,4,5) and one to be submitted (Chapter 3). The following problems have been studied:

Channelling and relativistic self-focusing of intense circularly polarized laser pulses. Theoretical models and Particle-In-Cell (PIC) simulations in two (2D) and three (3D) spatial dimensions are used to investigate the channelling mechanism in underdense plasma. Long range interaction of intense laser pulses with underdense plasma is studied using 2D PIC code (Chapter 2). The simulations are carried out for a wide range of plasma densities and laser powers. The results of the simulations have been compared with a theoretical model. The mechanisms that disrupt the channelling process such as surface wave excitation and transverse instability are described. The results of realistic 3D simulations are illustrated in Chapter 3. Azimuthal behavior of the laser pulse such as ring formation and azimuthal instability can only be studied in 3D geometry. It has been shown that the azimuthal instability can break up the laser pulse. These are the subjects of Chapters 2 and 3.

In Chapter 4, the excitation of a magnetic field during the interaction of a circularly polarized laser pulse with an underdense plasma has been studied. It is known that a circularly polarized laser pulse can induce a magnetic field in the plasma. Building on the results of Chapters 2 and 3 about relativistic self-focusing and channelling we have analyzed the excitation of an axial magnetic field that accompanies the laser pulse self-focusing in underdense plasmas. The radial distribution of the axial mag-

netic field was calculated by solving model equations and using the laser intensity and channel density profiles from simulations. These results have been compared with the magnetic field obtained in simulations.

Studies on electron wakefield acceleration using 2D PIC code were carried out in support of the experimental results and are the subject of Chapter 5. The experiments were performed using the 10 TW laser at the Canadian Advanced Laser Light Source facility.

1.1 Relativistic Self-Focusing

Propagation of intense laser pulses in underdense plasma has a variety of applications including laser plasma accelerators [3–5] and laser plasma channelling. For many of these applications, it is very important that the laser pulse propagates over large distances at high intensity. If there is no optical guiding, the interaction length will be limited to approximately the Rayleigh length. Self-focusing and channelling provide a possibility for nonlinear optical guiding of laser pulses in underdense plasma. Self-focusing can occur if the laser power exceeds the threshold power, P_{cr} , for self-focusing ($P > P_{cr}$). The required power for this effect, for densities $10^{18} - 10^{20} \text{ cm}^{-3}$ and laser wavelength of $1 \mu\text{m}$, is between 2 and 20 TW. Terawatt lasers became available in early 1990's. So the experimental studies of self-focusing has been started at that time. Several experiments have been carried out to investigate this process in recent years [9–13].

Lowering the plasma frequency is one of the relativistic features in laser plasma interaction. The plasma frequency is $\omega_p = \sqrt{\frac{4\pi e^2 n_e}{m}}$ which is determined by the electron density and electron mass. The dispersion relation of an electromagnetic wave in a

plasma is :

$$\omega^2 = \omega_p^2/\gamma + c^2k^2, \quad (1.1)$$

where γ is the relativistic factor ($\gamma = (1 + p^2/m^2c^2)^{1/2}$, $\mathbf{p} = \gamma m\mathbf{v}$ is the electron momentum), ω is the laser frequency, k is the wave number and ω_p is the plasma frequency. At relativistic laser intensities, the relativistic factor depends on the local intensity I . The increase of mass by the relativistic factor reduces the plasma frequency and this will affect the light propagation in plasma. Therefore the plasma index of refraction can be written as:

$$n_r = \sqrt{1 - (\omega_p/\gamma\omega)^2}. \quad (1.2)$$

Two main phenomena can be explained by the change of refractive index: the first one is the induced transparency where an overdense plasma can become transparent to radiation due to the relativistic decrease of the plasma frequency and the other one is relativistic self-focusing which is due to the modification of the refractive index. For a laser beam with an intensity profile peaked on axis ($r = 0$), the radial profile of γ will have an on-axis maximum ($\gamma(0) > \gamma(r)$). The index of refraction will have a maximum on axis and this causes the wavefront to curve inward and the laser pulse will converge. This will result in optical guiding of the laser light. The laser pulse phase velocity depends on the refractive index ($v_\phi = c/n_r$) and therefore on the laser intensity. Local variation of the phase velocity will change the shape of the laser pulse. The phase speed of the laser pulse will decrease in regions of higher laser intensity. This has the effect of focusing of the laser pulse. Thus The plasma acts as a positive lens, focusing the laser to smaller spot size and increasing the peak laser intensity. Variations in the plasma density can also change the refractive index. The transverse ponderomotive force can push some electrons out of the central axis, making an

electron density channel with minimum density on axis. This will make a radially dependent refractive index and will help focusing of the laser pulses. The first model of relativistic self-focusing was developed by Litvak [14] and Max *et. al* [15]. Sprangle *et. al* [16] has evaluated the thresholds for relativistic self-focusing using analytical methods. Kurki-Suonio *et. al* [19] have developed stationary analytical solution to nonlinear Schrodinger equation for one dimensional geometry. Later Sun *et. al* [6] derived a 2D (r,z) the nonlinear Schrodinger equation considering combined effects of relativistic nonlinearity and charge displacement in homogeneous plasma. This work presented the numerical evaluation of the threshold of relativistic self-focusing, the value which has been approximately estimated in earlier work. Feit *et. al* [20] later showed that this model doesn't satisfy the global charge conservation. Feit solved this problem by introducing electron temperature effects which were supposed to be calculated from experimental conditions. Cattani *et. al* [7] and Kim *et. al* [8] have obtained stationary solutions for channeling and multi-channeling in 2D and 3D cylindrical geometry. Their solutions satisfy the global charge conservation through Poisson equation. We proceed with a general theoretical model which will be used later for comparison with simulations (Chapters 2 and 3). For linear polarization, the analysis is more complicated due to the second harmonic density response [15, 22]. Using dimensionless variables: $\mathbf{a} = e\mathbf{A}/mc^2$, $\phi = e\Phi/mc^2$, $\mathbf{p} = \mathbf{P}/mc$ and $n = N_e/N_0$, where N_0 is background plasma density, \mathbf{A} is a vector potential, Φ is a scalar potential, \mathbf{P} is the momentum and N is the electron density. The Maxwell's equations for the normalized vector and scalar potentials in Coulomb gauge assuming fixed ions are:

$$\nabla^2 \mathbf{a} - \frac{1}{c^2} \frac{\partial^2 \mathbf{a}}{\partial t^2} = \frac{1}{c} \frac{\partial \nabla \phi}{\partial t} + \frac{\omega_p^2}{c^2} \frac{n \mathbf{p}}{\gamma}, \quad (1.3)$$

$$\nabla^2 \phi = \frac{\omega_p^2}{c^2} (n - 1). \quad (1.4)$$

The equation of motion for cold electron fluid is:

$$\left(\frac{\partial}{\partial t} + (\mathbf{v} \cdot \nabla)\right)\mathbf{P} = -e\left(-\frac{1}{c}\frac{\partial \mathbf{A}}{\partial t} - \nabla\Phi + \frac{\mathbf{v}}{c} \times (\nabla \times \mathbf{A})\right). \quad (1.5)$$

Using the equality

$$\mathbf{v} \times (\nabla \times \mathbf{p}) = c\nabla\gamma - (\mathbf{v} \cdot \nabla)\mathbf{p}, \quad (1.6)$$

and rewriting (1.5) as the equation for the canonical momentum $\mathbf{P}_c = \mathbf{p} - \frac{e}{c}\mathbf{A}$,

$$\frac{\partial \mathbf{P}_c}{\partial t} - \mathbf{v} \times (\nabla \times \mathbf{P}_c) = -mc^2\nabla\gamma + e\nabla\varphi. \quad (1.7)$$

Operating with $\nabla \times$ on Eq. (1.7) we derive the equation for the generalized vorticity,

$$\mathbf{\Omega} = \nabla \times \mathbf{P}_c,$$

$$\frac{\partial \mathbf{\Omega}}{\partial t} - \nabla \times (\mathbf{v} \times \mathbf{\Omega}) = \mathbf{0}. \quad (1.8)$$

It can be shown [23,24] using Eq. (1.8) that if $\mathbf{\Omega} = \mathbf{0}$ everywhere at some initial time then $\mathbf{\Omega}$ remains zero at later times. The generalized vorticity vanishes initially in our cold electron plasma in the absence of a laser pulse. Because $\nabla \times (\mathbf{p} - \frac{e}{c}\mathbf{A}) = 0$ we can introduce a scalar function ψ ,

$$\gamma m \mathbf{v} = \frac{e}{c}\mathbf{A} + \nabla\psi, \quad (1.9)$$

$$\frac{\partial \psi}{\partial t} = e\varphi - mc^2(\gamma - 1), \quad (1.10)$$

The laser pulse is short enough to neglect the ion motion, and we assume that the plasma will approach a quasi-stationary and homogeneous state where $\psi = 0$. Therefore $\mathbf{p} = \mathbf{a}$, also $\gamma = \sqrt{1 + p^2}$. Here we will derive the threshold power for self-focusing of a weakly relativistic laser pulse in an underdense plasma for circularly polarized laser pulses using paraxial approximation. Considering $\mathbf{a} = 1/2((\mathbf{e}_y + i\mathbf{e}_z)a(r, x)e^{i\xi} + c.c)$ and taking time and space derivatives, we obtain:

$$i\omega \frac{\partial a}{\partial t} + ic^2k \frac{\partial a}{\partial x} - \frac{c^2}{2}\nabla_{\perp}^2 a - \frac{\omega_p^2}{2}\left(1 - \frac{n}{\gamma}\right)a = 0. \quad (1.11)$$

Transforming time and space variables to a frame moving with the group velocity of the pulse ($V_g = c^2k/\omega$), $\xi = x - V_g t$, $t = \tau$, simplifies the above equation to:

$$i\omega \frac{\partial a}{\partial \tau} = c^2 \nabla_{\perp}^2 \frac{a}{2} + \omega_p^2 \left(1 - \frac{n}{\gamma}\right) \frac{a}{2}. \quad (1.12)$$

Now normalizing time to $\omega_p^2 \tau / \omega$ and r to $k_p r$ where $k_p = \omega_p / c$:

$$\frac{\partial a}{\partial t} + \frac{i}{2} \nabla_{\perp}^2 a + \frac{i}{2} \left(1 - \frac{n}{\gamma}\right) a = 0. \quad (1.13)$$

Equation (1.13) describes the evolution of the laser pulse as it propagates through plasma. Assuming that the plasma density is homogeneous $n = 1$, for weakly nonlinear circularly polarized laser pulse:

$$\gamma^{-1} \simeq 1 - \frac{|a|^2}{4}. \quad (1.14)$$

Substituting Eq. (1.14) into Eq. (1.13) yields a nonlinear Schrodinger equation (NLSE):

$$\frac{\partial a}{\partial t} = -\frac{i}{2} \nabla_{\perp}^2 a - \frac{i}{8} |a|^2 a, \quad (1.15)$$

This equation has been studied extensively in the literature [25, 26]. Some conserved quantities can be derived from Eq. (1.15). Multiplying both sides by a^* and adding the complex conjugate of the result ($a \times \partial / \partial a^*$) gives:

$$\frac{\partial}{\partial t} |a|^2 = \frac{i}{2} a \nabla_{\perp}^2 a^* - \frac{i}{2} a^* \nabla_{\perp}^2 a, \quad (1.16)$$

Integrating the left hand side of Eq. (1.16) in cylindrical geometry:

$$\int_0^{\infty} \frac{\partial}{\partial t} |a|^2 d^2 r = 0. \quad (1.17)$$

Equation (1.17) implies that the normalized beam power is conserved. Many other conserved quantities can be derived but one of the most important ones is the Hamiltonian $H \equiv 1/2 \nabla_{\perp}^2 |a|^2 - 1/16 |a|^4$ which is globally conserved. For a Gaussian laser

beam $a(r) = a_0 \exp(-r^2/2\sigma_0^2)$ where σ_0 is the nominal spot size in vacuum, i.e. the radius at which the intensity is $1/e$ times its peak value, the Hamiltonian is:

$$H = \frac{\pi a_0^2}{2} \left(1 - \frac{a_0^2 \sigma_0^2}{16}\right). \quad (1.18)$$

Self-focusing occurs when focusing has balanced diffraction. This is equivalent to $H = 0$ and we obtain $a_0^2 \sigma_0^2 = 16$. This presents a threshold power in normalized unit: $P_c = 16\pi$ which in dimensional unit is:

$$P_{cr} \simeq 17.5 \left(\frac{\omega}{\omega_p}\right)^2 GW. \quad (1.19)$$

This is the usual expression for threshold power for self-focusing [14–16]. It has been shown that the condition for self-focusing in 2D slab geometry is $\sqrt{2}a_0^2 \sigma_0^2 = 16$ [17,18].

1.2 Magnetic Field Generation by Circularly Polarized Laser Pulses in Underdense Plasmas

When a laser pulse irradiates a plasma, the laser electric and magnetic field are propagating into the medium. The laser magnetic field amplitude is given by [28]:

$$B_L(\text{Gauss}) = 9.2 \times 10^6 \left(\frac{I_L}{10^{16} W/cm^2}\right)^{1/2} \quad (1.20)$$

where I_L is the laser intensity. The laser frequency sets the scale for high-frequency phenomena. The period of one laser oscillation is about 3.3 fs for a laser with wavelength of 1 μm . One of the features of high intensity laser plasma interaction is its potential for generation of large magnetic fields in the megagauss range. One of the mechanisms that lead to generation of quasi-static magnetic field in a plasma is the inverse Faraday effect (IFE) which corresponds to the generation of magnetic field

in the plasma by a circularly polarized laser pulse. During the interaction of the plasma electrons with the circularly polarized laser pulse, azimuthal electron current is produced which leads to generation of axial magnetic field. We will focus on studying the generation of magnetic field during interaction of circularly polarized laser pulses with plasma in Chapter 4. A large number of papers on the generation of axial magnetic field due to IFE exist [29–34]. However there is no agreement on the predicted strength of the excited axial magnetic field at moderate and relativistic intensities. The strength of the axial magnetic field in interaction of low-energy laser light with initially homogeneous plasma is proportional to the fourth power of the laser amplitude [31, 35]. However as predicted in [36, 37] the strength of the magnetic field increases linearly with the field amplitude. On the other hand, most authors [31, 38–41] concluded that the strength of the axial magnetic field should saturate at relativistic amplitudes of the laser light. A nonlinear model for excitation of quasi-static magnetic field in electron cavitated channels of a circularly polarized long laser pulse was studied numerically by Kim *et. al* [41]. Frolov [42] investigated the IFE of a circularly polarized laser pulses in plasma channels with radially nonuniform electron density distribution. His analytical analysis is based on relativistic hydrodynamic equations for cold plasma. To study the propagation of a laser pulse in plasma, we consider a plasma channel with electron density $N_e(r)$ and the laser pulse is propagating along the channel axis, x direction. The electric field of the pulse is [42]:

$$\mathbf{E}_L(r, t) = \frac{1}{2}(\mathbf{e}_y + i\lambda\mathbf{e}_z + \frac{i\mathbf{e}_x}{k_0}(\frac{\partial}{\partial y} + i\lambda\frac{\partial}{\partial z}))E_0(r, \xi) \exp i(k_0x - \omega_0t) + c.c \quad (1.21)$$

where ω_0 and k_0 are laser frequency and laser wavenumber. $E_0(r, \xi)$ is the amplitude of the laser field and $\xi = x - V_g t$ is longitudinal coordinate moving with the

pulse group velocity $V_g = c^2 k_0 / \omega_0$. $\lambda = \pm 1$ for circularly polarized and $\lambda = 0$ for linearly polarized laser pulse. The electric field of the pulse has a component along the direction of propagation comes from the fact that the laser radiation is a transverse electromagnetic field. We use Maxwell's equations for quasi-static electric and magnetic fields together with relativistic hydrodynamic equations for a cold electron fluid,

$$\nabla \times \mathbf{E} = -\frac{1}{c} \frac{\partial \mathbf{B}}{\partial t}, \quad (1.22)$$

$$\nabla \times \mathbf{B} = \frac{1}{c} \frac{\partial \mathbf{E}}{\partial t} + \frac{4\pi e}{m_e c \gamma} N_e(r) \mathbf{p} + \frac{4\pi}{c} \mathbf{j}, \quad (1.23)$$

$$\nabla \cdot \mathbf{B} = 0, \quad (1.24)$$

$$\frac{\partial \mathbf{p}}{\partial t} + (\mathbf{v} \cdot \nabla) \mathbf{p} = e \mathbf{E} + \frac{e}{c} \mathbf{v} \times \mathbf{B}. \quad (1.25)$$

where \mathbf{j} and \mathbf{p} are the nonlinear current density and momentum of the electrons ($\mathbf{p} = \gamma m \mathbf{v}$) and γ is the relativistic factor. The nonlinear current density is the averaged product of fast varying electron velocity and electron density ($e \langle \delta N_L \cdot \mathbf{v}_L \rangle$, where L denotes the laser). Using Eq. (1.9), we find

$$\mathbf{B} = -\frac{c}{e} \nabla \times \mathbf{p}, \quad (1.26)$$

Substituting Eq. (1.26) into (1.25) gives,

$$\mathbf{E} = mc \nabla \gamma + \frac{1}{e} \frac{\partial \mathbf{p}}{\partial t}. \quad (1.27)$$

Using the continuity equation:

$$\frac{\partial}{\partial t} \delta N_L + \nabla \cdot (N_e(r) \mathbf{v}_L) = 0, \quad (1.28)$$

the following expression can be found for fast oscillating electron density and electron velocity:

$$\delta N_L(r, t) = \frac{e E_0(r, \xi)}{2 m_e \omega_0^2} \left(\frac{\partial}{\partial y} + i \lambda \frac{\partial}{\partial z} \right) \left(\frac{N_e(r)}{\gamma} \right) \exp(-i \omega_0 t + i k_0 x) + c.c., \quad (1.29)$$

$$\mathbf{v}_L(r, t) = \frac{ie}{2m_e\omega_0\gamma}((\mathbf{e}_y + i\lambda\mathbf{e}_z) + \frac{i\mathbf{e}_x}{k_0}(\frac{\partial}{\partial y} + i\lambda\frac{\partial}{\partial z}))E_0(r, \xi) \exp(-i\omega_0 t + ik_0 x) + c.c. \quad (1.30)$$

Using the above equations, we find that the nonlinear current density has only an azimuthal component:

$$j_\phi = -\frac{\lambda e^3 E_0^2(r, \xi)}{2m_e^2 \omega_0^3 \gamma} \frac{\partial}{\partial r} \left(\frac{N_e(r)}{\gamma} \right). \quad (1.31)$$

This equation shows that j_ϕ and subsequently B_x is zero for linearly polarized laser light. Eliminating the electric and magnetic fields in Eqs.(1.22-1.25), we find an equation for the slowly varying electron momentum:

$$\left(\frac{\partial^2}{\partial \xi^2} + \frac{k_p^2(r)}{\gamma} \right) \mathbf{p} + \nabla \times \nabla \times \mathbf{p} = -\frac{4\pi e}{c^2} \mathbf{j} + m_e V_g \frac{\partial}{\partial \xi} \nabla \gamma \quad (1.32)$$

where $k_p(r) = \omega_p(r)/c$ is the plasma wavenumber. Note that low frequency electron density variation is assumed to be small and ignored. The electron momentum components are:

$$\frac{\partial^2 p_x}{\partial r \partial \xi} + \frac{k_p^2(r)}{\gamma} p_r = m_e c \frac{\partial^2 \gamma}{\partial r \partial \xi} \quad (1.33)$$

$$\left(\frac{\partial^2}{\partial \xi^2} + \frac{k_p^2(r)}{\gamma} \right) p_x + \frac{1}{r} \frac{\partial}{\partial r} r \left(\frac{\partial p_r}{\partial \xi} - \frac{\partial p_x}{\partial r} \right) = m_e c \frac{\partial^2 \gamma}{\partial \xi^2} \quad (1.34)$$

$$\frac{k_p^2(r)}{\gamma} p_\phi - \frac{\partial}{\partial r} \frac{1}{r} \frac{\partial}{\partial r} (r p_\phi) = -\frac{4\pi e}{c^2} j_\phi \quad (1.35)$$

Here the group velocity of the laser light was assumed to be equal to the speed of light c . This assumption is correct for $\omega_0 \gg \omega_p(r)$. We are interested in the interaction between an underdense plasma and an intense and long circularly polarized laser light pulse such that the pulse duration time exceeds the electron oscillation time ($\tau \gg \omega_{pe}^{-1}$ where τ is pulse duration). In this case only the axial component of the magnetic field is excited:

$$\frac{1}{r} \frac{d}{dr} \left(\frac{r\gamma}{k_p^2(r)} \frac{d}{dr} (B_x) \right) - B_x = -\frac{\lambda e c}{2m_e \omega_0^3} \frac{d}{dr} \left(\frac{r E_0^2(r)}{N_e(r)} \frac{d}{dr} \left(\frac{N_e(r)}{\gamma} \right) \right) \quad (1.36)$$

where magnetic field is normalized to $mc\omega/e$. In deriving Eq. (1.36), $\mathbf{B} = -\frac{c}{e}\nabla \times \mathbf{p}$ (1.26) is used. Eq. (1.36) shows that the magnetic field depends on the gradient of $N_e(r)/\gamma$. The solution to Eq. 1.36 gives the distribution of quasi-static magnetic field. A detailed study of magnetic field generation during interaction of circularly polarized laser pulses with underdense plasma is presented in Chapter 4.

1.3 Laser-Plasma Accelerators

Acceleration of charged particles using electromagnetic fields has been studied for about one hundred years. One of the methods to generate big accelerating fields and to achieve high particle energies is using laser-plasma interactions. In recent years, the invention of the chirped pulse amplification technique allowed the generation of intense laser pulses of ultra short durations and created new opportunities in laser plasma acceleration. In 1979 Tajima and Dawson [43] proposed a new method to accelerate charged particles using laser-plasma interaction. In their model, a short laser pulse interacts with an underdense plasma and generates a strong oscillating field in its wake. The generated electrostatic field by such a process can accelerate electrons. Net acceleration happens when the electrons are injected into the wakefield with velocities close to the phase velocity of the wave. The phase velocity of the excited wake is equal to the group velocity of the laser pulse [43]. In the non-relativistic case $v_g = c\sqrt{1 - \omega_p^2/\omega_0^2}$ where ω_p is the plasma frequency and ω_0 is the laser frequency. For relativistic circularly polarized laser pulse $v_g = c\sqrt{1 - \omega_p^2/\gamma\omega_0^2}$ where γ is the relativistic factor. It can be seen that the required velocity for injection of electrons into the wakefield is lower for higher plasma densities. Once the electrons are trapped by the wakefield, they undergo acceleration. However there are limits on the maximum

energy that the electrons can attain. One limiting factor is the maximum electric field that the plasma can support. For linear wakefields, the maximum electric field that can be obtained is $E_0 = 4\pi en_0 c / \omega_p$ where n_0 is the uniform background density. For relativistic cases ($a_0 \geq 1$), nonlinear-wakes, the limiting field using 1D cold fluid equations is higher and is given by [44] $E_w^{max} = \sqrt{2(\gamma_{ph} - 1)} E_0$ where $\gamma_{ph} = (1 - v_{ph}^2/c^2)^{-1/2}$ is the relativistic factor of the wake with phase velocity $v_{ph} < c$. However, plasma finite temperature effect can reduce this field [45].

Once the electron is trapped and accelerated by the wakefield, the velocity of the electron in the wakefield will increase and eventually overtake the wake wave which is moving with $v_{ph} < c$. Finally the electron will get to the regions in the wakefield where it will be decelerated by the electrostatic fields. This is the maximum energy that the electrons can attain. The distance over which this process happens is called dephasing length L_d . This distance can be estimated $L_d \approx \gamma_{ph}^2 \lambda_p$. For $\gamma_{ph} \gg 1$ the maximum energy gain is [43] $W_{max} \approx 2\pi \gamma_{ph}^2 (E_{max}/E_0) m_e c^2$ where E_{max} is the maximum electric field of the wakefield. A detailed analysis of the maximum energy of an electron trapped in the wakefield has been presented for example in Ref. [46]. An estimate for the dephasing length is given by [46]:

$$L_d \cong \gamma_{ph}^2 \lambda_{Np} \begin{cases} 2/\pi & \text{for } E_{max}/E_0 \ll 1 \\ 1/2 & \text{for } E_{max}/E_0 \gg 1 \end{cases} \quad (1.37)$$

where λ_{Np} is the nonlinear wavelength given by:

$$\lambda_{Np} \cong \lambda_{Np} \begin{cases} 1 & \text{for } E_{max}/E_0 \ll 1 \\ (2\pi) E_{max}/E_0 & \text{for } E_{max}/E_0 \gg 1 \end{cases} \quad (1.38)$$

As the laser pulse propagates into the plasma, it loses energy due to the absorption in the plasma. The laser pulse depletion length can be estimated [47] $d_{dl} \approx L(\omega_0/\omega_p)^2$

where L is the pulse length. If the depletion length is shorter than the dephasing distance, the maximum attainable energy for the electron will be reduced. The reason is that the laser pulse is being absorbed by the plasma over this distance. The depletion length of a circularly polarized square laser pulse of length $L \approx \lambda_{Np}/2$ is [47–49]:

$$l_{dl} \cong (\omega_p/\omega)^2 \lambda_p \begin{cases} a_0^{-2} & \text{for } a_0 \ll 1 \\ a_0/3\pi & \text{for } a_0 \gg 1 \end{cases} \quad (1.39)$$

One dimensional laser pulse was considered up to here. In three dimensions, the laser pulse is focused and defocused. The length over which a Gaussian shaped laser pulses defocus in vacuum is the Rayleigh length [50]. If the waist size of the laser w_0 is very small, the Rayleigh length can be smaller than the dephasing length and this will limit the maximum energy that the electron can get. However, fulfilling the condition for optical guiding of the laser pulse into the plasma is a solution for this. Self-focusing can occur for laser pulses in which $L > \lambda_p$ [15] or in a performed plasma channel [51]. The critical power for self-focusing is $P_{cr} \approx 17(\lambda_p/\lambda_0)^2$ GW. But even with relativistic self-focusing a laser pulse can bend away from the pulse direction due to hosing instability. This has been shown both theoretically [52] and experimentally [53] and it will limit the distance over which acceleration can occur. Moreover it has been shown that for ultrashort laser pulses in which $L \leq \lambda_p$, relativistic self-focusing is ineffective [51].

Acceleration of self-trapped electrons has been observed in experiments [5, 54–60].

In Chapter 5, we study electron wakefield acceleration using 2D PIC code in support of the experiment which was carried on at Canadian Advanced Laser Light Source (ALLS) facility [61]. The experiment was performed using 10 TW laser pulses. Parameters corresponding to the experimental conditions were used in 2D PIC sim-

ulations. The maximum energy of electron bunch of 30 MeV was measured from the simulations which is close to the experimental result. The detailed description is the subject of Chapter 5.

1.4 Thesis Outline

In this thesis the interaction of intense laser pulses with underdense plasma is studied. Theoretical and numerical modelling (2D and 3D Particle-in-Cell code) were used to investigate the different physical processes in the field of laser plasma interaction. The work in this thesis covers areas related to self-focusing and channeling of the strong laser pulses in underdense plasma, magnetic field generation due to inverse Faraday effect during interaction of the laser pulses with plasma and electron wakefield acceleration. The thesis is organized as follows:

-Chapter 2 presents the self-focusing and channeling of intense laser pulses in underdense plasma in details. Numerical results of interaction of laser pulses with plasma in large scale from the 2D PIC code Mandor [27] are presented and compared with theoretical results.

-Chapter 3 investigates the self-focusing and channeling of the laser pulse in underdense plasma using the 3D PIC code Mandor. The numerical and theoretical results are compared.

-Chapter 4 focuses on magnetic field generation due to the inverse Faraday effect in laser plasma interaction. The relevant equations are solved numerically and the results are compared with 3D simulations.

-Chapter 5 describes the electron wakefield acceleration in laser interaction with underdense plasma. This Chapter splits to two Sections discussing the experiments and

supporting simulation results. One of the motivations for this work was to interpret the results obtained from the experiment.

-**Chapter 6** summarizes and concludes the work described in the thesis.

Bibliography

- [1] D. Strickland and G. Mourou, *Op. Commun.* **56**, 219 (1985).
- [2] S.-W. Bahk, P. Rousseau, T. A. Planchon, V. Chvykov, G. Kalintchenko, A. Mak-simchuk, G. A. Mourou and V. Yanovsky. *Opt. Lett.* **29**, 2837 (2004).
- [3] E. Esarey, P. Sprangle, J. Krall, and A. Ting, *IEEE Trans. Plasma Sci.* **PS-24**, 252 (1996).
- [4] C. Coverdale, C. B. Darrow, C. D. Decker, W. B. Mori, K. C. Tzeng, K. A. Marsh, C. E. Clayton, and C. Joshi, *Phys. Rev. Lett.* **74**, 4659 (1995).
- [5] A. Modena, Z. Najmudin, A. E. Dangor, C. E. Clayton, K. A. Marsh, C. Joshi, V. Malka, C. B. Darrow, C. Danson, D. Neely and F. N. Walsh, *Nature* **337**, 606 (1995).
- [6] em, O. B. Shiryayev, A. McPherson, K. Boyer, and C. K. Rhodes, *J. Opt. Soc. Am. B* **11**, 1941 (1994).
- [6] Gou Zheng Sun, E. Ott, Y. C. Lee and P. Gudzar, *Phys. Fluids* **30**, 526 (1987).
- [7] F. Cattani, A. Kim, D. Anderson, and M. Lisak, *Phys. Rev. E.* **64**, 016412 (2001).

-
- [8] A. Kim, M. Tushentsov, F. Cattani, D. Anderson, and M. Lisak, *Phys. Rev. E.* **65**, 036416 (2002).
- [9] A. B. Borisov, X. Shi, V. B. Karpov, V. V. Korobin, J. C. Sol
- [10] P. Monot, T. Auguste, P. Gibbon, F. Jackober, G. Mainfray, A. Dulieu, M. Louis-Jacquet, G. Malka, and J. L. Miquel, *Phys. Rev. Lett.* **74**, 2953 (1995).
- [11] R. Wagner, S.-Y. Chen, A. Maksimonchuk, and D. Unstadter, *Phys. Rev. Lett.* **78**, 3125 (1997).
- [12] K. Krushelnick, S. Ting, C. I. Moore, H. R. Burris, E. Esarey, P. Sprangle, and M. Baine, *Phys. Rev. Lett.* **78**, 4047 (1997).
- [13] P. Chessa, P. Mora, Thomas M. Antonsen, Jr. *Phys. Plasmas*, **5**, 3451 (1998).
- [14] A. G. Litvak, *Sov. Phys. JETP* **30**, 344 (1970).
- [15] C. E. Max, J. Arons and A. B. Langdon, *Phys. Rev. Lett.* **33**, 209 (1974).
- [16] P. Sprangle, CM. Tang, and E. Esarey, *IEEE Trans. on Plasma Sci.* **15**, 145 (1987).
- [17] K.-C. Tzeng and W. B. Mori, *Phys. Rev. Lett.* **81**, 104 (1998).
- [18] C. D. Decker, W. B. Mori, K. C. Tzeng, and T. Katsouleas, *Phys. Plasmas* **3**, 2047 (1996).
- [19] T. Kurki-Suonio, P. J. Morrison, and T. Tajima, *Phys. Rev. A.* **40**, 32302 (1989).

-
- [20] M. D. Feit, A. M. Komashko, S. L. Musher, A. M. Rubenchik, and S. K. Turitsyn, *Phys. Rev. E* **57**, 7122 (1998).
- [21] M. Tabak, J. Hammer, M. E. Glinsky, W. L. Kruer, S. C. Wilks, J. Woodworth, E. M. Campbell, M. D. Perry, and R. J. Mason, *et al.*, *Phys. Plasmas* **1**, 1626 (1994).
- [22] W. B. Mori, C. Joshi, J. M. Dawson, D. W. Forsland and J. M. Kindel, *Phys. Rev. Lett.* **60**, 1298 (1989).
- [23] I. D. Kaganovich, G. Shvets, E. Stratsev, and R. C. Davidson, *Phys. Plasmas* **8**, 4180 (2001).
- [24] X. L. Chen and R. N. Sudan, *Phys. Fluids. B* **5**, 1336 (1993).
- [25] P. K. Shukla, N. N. Rao, M. Y. Yu and N. L. Tsintsadze, *Phys. Rep.* **138**, 1 (1986).
- [26] A. Decoster, *Phys. Rep.* **47**, 285 (1978).
- [27] D. Romanov, V. Yu. Bychenkov, W. Rozmus, C. E. Capjack and R. Fedosejevs, *Phys. Rev. Lett* **93**, 215004 (2004).
- [28] S. Eliezer, *Interaction of High-Power Lasers With Plasmas*, (Institute of Physics Publishing , 2002), p. 144.
- [29] A. Sh. Abdullaev and A. A. Frolov, *Sov. Phys. JETP Letters* **33**, 101 (1981)
- [30] Yu. M. Aliev, V. Yu. Bychenkov, and A. A. Frolov, Quasi-static magnetic fields generation in a plasma with strong electromagnetic radiation, In book: Nonlin-

- ear Theory of Strong Electromagnetic Wave-Plasma Interactions, Nova Science Publ., Ed. O.N.Krokhin 1993, p. 87.
- [31] V. Yu. Bychenkov and V. T. Tikhonchuk, *Laser and Particle Beams* **14**, 55 (1996).
- [32] C. Y. Zheng, X. T. He and S. P. Zhu, *Phys. Plasmas*. **12**, 044505 (2005).
- [33] T. Lehner, *Physica Scr.* **49**, 704 (1994).
- [34] V. I. Berezhiani, S. M. Mahajan, and N. L. Shatashvili, *Phys. Rev. E*. **55**, 995 (1997). *Rev. E* **55**, 995 (1997).
- [35] Z. M. Sheng and J. Meyer-ter-Vehn, *Phys. Rev. E*. **54**, 1883 (1996).
- [36] Z. Najmudin, M. Tatarakis, A. Pukhov, E. L. Clark, R. J. Clarke, A. E. Dangor, J. Faure, V. Malka, D. Neely, M. I. K. Santala, and K. Krushelnick, *Phys. Rev. Lett.* **87** 215004 (2001).
- [37] S. P. Zhu, C. Y. Zheng, and X. T. He, *Phys. Plasmas*. **10**, 4166 (2003).
- [38] G. Zeng, *Phys. Rev. E* **60**, 5950 (1999).
- [39] G. Zeng and X. He, *Phys. Plasmas*. **6**, 2954 (1999).
- [40] G. Zeng, *Phys. Plasmas*. **7**, 1539 (2000).
- [41] A. Kim, M. Tushentsov, D. Anderson and M. Lisak, *Phys. Rev. Lett.* **89**, 095003 (2002) **89**, 095003-1 (2002).
- [42] A. A. Frolov, *Plasma Phys. Reprts.* **30**, 698 (2003).
- [43] T. Tajima and J. M. Dawson, *Phys. Rev. Lett* **43**, 267 (1979).

- [44] A. I. Akhiezer and R. V. Polovin, *Sov. Phys. JETP* **3**, 696 (1956).
- [45] T. Katsouleas and W. B. Mori, *Phys. Rev. Lett* **61**, 90 (1988).
- [46] E. Esarey and M. Pilloff, *Phys. Plasmas* **2**, 1432 (1995).
- [47] S. V. Bulanov, I. N. Inovenkov, V. I. Kirsanov, N. M. Naumova and A. S. Sakharov, *Phys. Fluids. B.* **4**, 1935 (1992).
- [48] A. Ting, E. esarey and P. Sprangle, *Phys. Fluids. B* **2**, 1390 (1990).
- [49] D. G. Teychenne, G. Bonnaud and J. Bobin, *Phys. Plasmas* **1**, 1771 (1994).
- [50] H. Kogelnik and T. Li, *Appl. Optics* **5**, 1550 (1966).
- [51] P. Sprangle, E. Esarey, J. Krall and G. Joyce, *Phys. Rev. Lett* **69**, 2200 (1992).
- [52] N.M. Naumova, J. Koga, K. Nakajima, T. Tajima, T. Zh. Esirkepov, S. V. Bulanov, and F. Pegoraro, *Phys. Plasmas* **8**, 4149 (2001).
- [53] L. M. Chen, H. Kotaki, K. Nakajima, J. Koga, S. V. Bulanov, T. Tajima, Y. Q. Gu, H. S. Peng, X. X. Wang, T. S. Wen, H. J. Liu, C. Y. Jiao, C. G. Zhang, X. J. Huang, Y. Guo, K. N. Zhou, J. F. Hua, W. M. An, C. X. Tang, and Y. Z. Lin, *Phys. Plasmas* **14**, 040703-1 (2007).
- [54] R. Wagner, S. Y. Chen, A. Maksimchuk, and D. Umstadter, *Phys. Rev. Lett.* **78**, 3125 (1997).
- [55] K. Nakajima, D. Fisher, T. Kawakubo, H. Nakanishi, A. Ogata, Y. Kato, Y. Kitagawa, R. Kodama, K. Mima, H. Shiraga, K. Suzuki, K. Yamakawa, T. Zhang, Y. Sakawa, T. Shoji, Y. Nishida, N. Yugami, M. Downer, and T. Tajima, *Phys. Rev. Lett.* **75**, 984 (1995).

- [56] V. Malka, S. Fritzler, E. Lefebvre, M.-M. Aleonard, F. Burgy, J.-P. Chambaret, J.-F. Chemin, K. Krushelnick, G. Malka, S. P. D. Mangles, Z. Najmudin, M. Pittman, J.-P. Rousseau, J.-N. Scheurer, B. Walton, and A. E. Dangor, *Science*, **298**, 1596 (2002).
- [57] C. G. R. Geddes Cs. Toth, J. van Tilborg, E. Esarey, C. B. Schroeder, D. Bruhwiler, C. Nieter, J. Cary and W. P. Leemans, *Nature* **431**, 538 (2004).
- [58] S. P. D. Mangles, C. D. Murphy, Z. Najmudin, A. G. R. Thomas, J. L. Collier, A. E. Dangor, E. J. Divall, P. S. Foster, J. G. Gallacher, C. J. Hooker, D. A. Jaroszynski, A. J. Langley, W. B. Mori, P. A. Norreys, F. S. Tsung, R. Viskup, B. R. Walton and K. Krushelnick, *Nature* **431**, 535 (2004).
- [59] E. Miura, K. Koyama, S. Kato, N. Saito, M. Adachi, Y. Kawada, T. Nakamura and M. Tanimoto, *Appl. Phys. Lett.* **86**, 251501 (2005).
- [60] A. Yamazaki, H. Kotaki, I. Daito, M. Kando, S. V. Bulanov, T. Zh. Esirkepov, S. Kondo, S. Kanazawa, T. Homma, K. Nakajima, Y. Oishi, T. Nayuki, T. Fujii and K. Nemoto, *Phys. Plasmas* **12**, 093101 (2005).
- [61] Z. L. Chen, C. Unick, N. Vafaei-Najafabad, Y. Y. Tsui, R. Fedosejevs, N. Naseri, P. -E. Masson-Laborde and W. Rozmus, *laser and particle beams*, **26**, 147 (2008).

Chapter 2

Self-Channelling of Relativistic Laser Pulses in Large-Scale Underdense Plasmas

2.1 Introduction

The problem of intense short laser pulse propagation in a large scale underdense plasma continues to attract research interest. According to the inertial confinement fusion fast ignition scenario [1] the ignition pulse will propagate through a mm-scale underdense plasma. The nonlinear evolution of such a pulse involves relativistic self-focusing and channeling [2,3]. These processes define the optimal choice of the pulse energy and time duration [4]. Electron-free plasma channels formed by relativistic pulses have been considered as the medium enabling x-ray generation and guiding of

A version of this Chapter has been published. N. Naseri, S. G. Bochkarev and W. Rozmus, 2010. *Physics of Plasmas*. 17: 033107-(1-11).

x-ray radiation without losses [5]. Experiments with Peta-watt lasers have generated spectra of relativistic electrons [6] that are accelerated by the combined electromagnetic fields of the laser pulse and quasistationary fields in the electron evacuated channels. Acceleration mechanisms involve stochastic dynamics of electrons in nonlinear fields including the betatron resonance [7]. These recent studies [4–6] are examples of problems related to nonlinear propagation of relativistic laser pulses. Their solutions have involved particle-in-cell (PIC) simulations that are performed in two spatial dimensions. More realistic PIC simulations in 3D geometries are still difficult to perform because of the very high demands on the computer time and memory. Our paper will demonstrate by means of 2D PIC simulations that analytical stationary solutions of relativistic self-focusing (RSF) and plasma channelling can be achieved in laser plasma in a specific range of plasma densities, provided that the laser power is above the threshold value. We will investigate the stability of such solutions and define conditions under which the channels are destroyed by surface mode effects and hosing like instabilities. Our understanding of such interactions builds on numerous numerical and theoretical studies of channel dynamics [8,9], polarization effects [10] and early studies of laser pulse channelling and RSF [11–14]. Since the first paper on the optical self-focusing [15] and the subsequent discovery of soliton like solutions [16], electromagnetic wave self-focusing has been extensively studied in theory and experiments. The focal point of our paper is the regime where light self focuses due to the combined effects of ponderomotive and relativistic nonlinearities [17,18]. The first mechanism occurs because of the expulsion of electrons by the transverse ponderomotive force of the laser pulse. Due to this density modification, the refractive index becomes larger on the axis, making this region act as a positive lens. The relativistic self-focusing occurs as a result of the increase in electron mass in high

intensity regions, decreasing plasma frequency and therefore increasing the refractive index $n_r = \sqrt{1 - n_0/(n_{cr}\gamma)}$, where γ is the relativistic factor, n_{cr} is critical density and n_0 is the background plasma density. Early theoretical studies identified these as the two main mechanisms leading to self-focusing [19–22]. The critical power for self-focusing in three dimensions has been defined by balancing nonlinear and diffraction effects [23] $P_{cr} = 17(\omega_0^2/\omega_p^2) \text{ GW}$, where ω_0 is the laser frequency, $\omega_p = \sqrt{4\pi e^2 n_0/m}$ is the plasma frequency, and m is the electron rest mass. For the laser pulse powers above the critical power, the transverse ponderomotive force could be large enough to expel all the electrons from the high intensity region, thus generating a channel free of electrons with a positive charge of background ions. The threshold power for channelling was first calculated by Sun *et al.* [19] in a cylindrical geometry. However as Feit *et al.* [20] later showed, the solutions by Sun *et al.* [19] and Borisov *et al.* [12] did not satisfy global charge conservation. Feit *et al.* [20] removed this inconsistency by introducing electron temperature effects. However this procedure lacked self-consistency as the temperature was supposed to be calculated from experimental conditions. More recently Cattani *et al.* [24] and Kim *et al.* [25] have obtained exact stationary channelling solutions in 2D and in the cylindrical 3D geometry, respectively. Their solutions satisfy total charge conservation by explicitly satisfying Poisson’s equation. This has led to some differences between total laser powers necessary to support stationary fully evacuated channels in previous models [12, 19] and in charge conserving solutions of Refs. [24, 25].

Analytical results by Cattani *et al.* [24] in the 2D slab geometry have provided a theoretical framework for our numerical investigations. From these solutions we are able to evaluate the threshold power for complete electron evacuation, P_{ch} , as well as the channel width and make comparison with PIC simulation results. According to

the model when the incident power is above the channelling power, a single channel will form. Such channels display stationary behaviour and are very close to analytical solutions by Cattani *et al.* [24]. We have also investigated the stability of localized solutions without full evacuation. These nonlinear solutions are unstable with respect to transverse perturbations and are responsible in our simulations for breaking up the filaments into several independent filaments of a smaller size. Individual filaments in such self-focused pulses are similar to single channel stationary solutions in terms of trapped power and the size of the channel.

In this Chapter we study the propagation of intense circularly polarized laser pulses in large-scale length underdense plasmas by using the PIC code Mandor [26]. We will study conditions under which channelling can occur. Different parameters such as the laser power and plasma density are considered. We have found that for high plasma densities, $n_0 \geq 0.1n_{cr}$, the transverse instability dominates the long time evolution of these filaments and leads to splitting of the nonlinear solutions. At lower densities and for filaments with large transverse size, surface waves accelerate electrons and contribute to the destruction of the plasma channels. The rise time of the laser pulse plays an important role in the stability of these channels and the growth of surface modes.

The paper is organized as follows: First we review the theory of channelling (Sec. 2.2 and 2.3). We discuss the simulation results for partial evacuation in Subsec. 2.2.3 and complete evacuation in Subsec. 2.3.1. The stability of partially evacuated channels is discussed in Subsec. 2.2.4. We also address the effects of surface wake excitation (Subsec. 2.3.3) and we calculate the wavelength of the excited wakes.

2.2 Relativistic Self-Focusing - theory and simulations

Since the original publication by Litvak and Max *et al.* [17, 18] RSF has been extensively studied in theory and by means of numerical simulations. We will focus our study on the theoretical model [12, 19–22] which gives stationary solutions on the time scale of the electron response. Ions are assumed fixed in this theory. In particular we will compare 2D PIC simulations with theoretical predictions based on the 2D version of this model [24]. We will describe the regime of plasma parameters where stationary solutions can be reached in PIC simulations. The single channel stationary 2D solutions [24] have been reproduced in our simulations. They display stable behaviour except for electron acceleration related to surface modes and instabilities at higher densities. We will emphasize the regime of the full evacuation of electrons from plasma channels. However in this Section we will start with reviewing the main assumptions of the RSF model. We will compare PIC code results with localized RSF soliton-like solutions for the field and electron density without full electron evacuation. From the analytical localized stationary solution in 2D we will be able to calculate the necessary power for RSF to occur. We will analyze the stability of nonlinear stationary RSF filaments with respect to transverse perturbations. We have found that these solutions are linearly unstable. This is consistent with the results of PIC simulations and the observed break up of a broad laser filaments into several individual narrow structures. Our analysis is similar to the description of the azimuthal breakup of the RSF filaments in a cylindrical geometry [27, 28].

2.2.1 Theoretical Model

First, we summarize assumptions and basic equations of the theoretical model of RSF [12, 19–22] and their solutions in 2D by Cattani *et al.* [24]. The basic set of equations consists of Maxwell's equations in the Coulomb gauge and equation of motion for the cold electron plasma

$$\nabla^2 \mathbf{A} - \frac{1}{c^2} \frac{\partial^2 \mathbf{A}}{\partial t^2} = \frac{1}{c} \frac{\partial}{\partial t} \nabla \varphi + \frac{4\pi}{c} n e \mathbf{v}, \quad (2.1)$$

$$\nabla^2 \varphi = 4\pi e (n - n_0), \quad (2.2)$$

$$\frac{\partial \mathbf{p}}{\partial t} + (\mathbf{v} \cdot \nabla) \mathbf{p} = \frac{e}{c} \frac{\partial \mathbf{A}}{\partial t} + e \nabla \varphi - \frac{e}{c} \mathbf{v} \times (\nabla \times \mathbf{A}), \quad (2.3)$$

Using the equality

$$(\mathbf{v} \cdot \nabla) \mathbf{p} = m c^2 \nabla \gamma - \mathbf{v} \times (\nabla \times \mathbf{p}), \quad (2.4)$$

and combining (2.3) and (2.4) one obtains $\nabla \times (\mathbf{p} - \frac{e}{c} \mathbf{A}) = 0$. Therefore we can write

$$\gamma m \mathbf{v} = \frac{e}{c} \mathbf{A} + \nabla \psi, \quad (2.5)$$

$$\frac{\partial \psi}{\partial t} = e \varphi - m c^2 (\gamma - 1). \quad (2.6)$$

Here γ is the relativistic factor, n is the electron density, n_0 is equilibrium density, $-e$ is electron charge and m is the rest mass of an electron. \mathbf{A} is the electromagnetic vector potential, φ is the electrostatic scalar potential and ψ is a scalar function. Vortex-free motion for electrons is assumed. The laser pulse is short enough for ion motion to be neglected and we will look for a quasi-steady-state where we can ignore the time dependence in (2.6). At first electrons are assumed to be cold so they have zero velocity before laser pulse arrives, thus $\psi = 0$. The plasma is considered homogeneous. The normalized vector potential is assumed as

$$\frac{e \vec{A}}{m c^2} = \frac{1}{2} a(y) \exp(i(hx - \omega_0 t)) (\mathbf{e}_y + i \mathbf{e}_z) + c.c., \quad (2.7)$$

where x is direction of propagation h is the propagation constant and y is transverse direction. Using the paraxial approximations $k_{\perp} \ll h$ where k_{\perp} is the transverse component of the laser wavenumber, the system of (2.1-2.6) reads

$$\nabla_{\perp}^2 a + \left(1 - \frac{\eta n}{\gamma}\right) a = 0, \quad (2.8)$$

$$\nabla_{\perp}^2 \phi = \eta(n - 1), \quad (2.9)$$

$$\phi = \gamma - 1, \quad (\text{if } n \neq 0) \quad (2.10)$$

where $\nabla_{\perp} = d/dy$, relativistic factor $\gamma = (1 + |a|^2)^{1/2}$ and $\eta = (n_0/n_{cr})/(1 - h^2 c^2/\omega_0^2)$, n_{cr} is critical density. a and ϕ are normalized by mc^2/e and transverse length is normalized to $[k_0 \sqrt{1 - h^2/k_0^2}]^{-1}$, where k_0 is the laser vacuum wave number. Consider (2.8) to be an equation of motion for the laser plasma system. Equation (2.8) can be obtained from the Hamilton's principle and we can write the Lagrangian of the system as [21]

$$L = g(a) \frac{a'^2}{2} - V(a), \quad (2.11)$$

where $g(a)$ is a metric and $V(a)$ is potential of the system to be found and the prime indicates the derivative with respect to y . Using Lagrange's equation:

$$g(a)a'' + \frac{1}{2} \frac{dg(a)}{da} a'^2 + \frac{\partial V}{\partial a} = 0, \quad (2.12)$$

and manipulating (2.8), using $n = \nabla^2 \phi / \eta + 1$ and noting that $\phi'' = \gamma''$ gives:

$$\frac{a''}{\gamma^2} - \frac{aa'^2}{\gamma^4} - \frac{\eta a}{\gamma} + a = 0, \quad (2.13)$$

We can obtain $g(a)$ and $V(a)$ by comparing (2.12) and (2.13),

$$g(a) = \frac{1}{1 + a^2}, \quad (2.14)$$

and

$$V(a) = \frac{a^2}{2} - \eta \sqrt{1 + a^2}, \quad (2.15)$$

2.2.2 RSF - Stationary Solution

Using $g(a)$ and $V(a)$, we can rewrite the Hamiltonian as [21],

$$H = \frac{1}{2(1+a^2)}a'^2 - \frac{1}{2}(2\eta\sqrt{1+a^2} - a^2), \quad (2.16)$$

Both $a(y)$ and $a'(y)$ are zero as y goes to infinity. Therefore $H = -\eta$ and (2.16) becomes:

$$a'^2 + 2\eta(1+a^2) - (1+a^2)(2\eta\sqrt{1+a^2} - a^2) = 0, \quad (2.17)$$

Integrating (2.17) gives the exact analytical solution for $n \neq 0$ [24]:

$$a(y) = \frac{2\sqrt{\eta(\eta-1)}\cosh(\beta(y-y^{(0)}))}{\eta\cosh^2(\beta(y-y^{(0)})) - \beta^2}, \quad (2.18)$$

where $\beta = \sqrt{\eta-1}$ and $y^{(0)}$ indicates the peak position of $a(y)$. This is a soliton-like transversely localized solution for the vector potential which does not lead to the full evacuation of the plasma channel. The electron density is calculated from the Poisson equation. By using $\nabla_{\perp}^2\phi = \nabla_{\perp}^2(\gamma-1)$ and (2.9), we can write:

$$\eta(n-1) = \nabla_{\perp}^2\gamma = \frac{aa''}{\gamma} + \frac{a'^2}{\gamma} - \frac{(aa')^2}{\gamma^3}, \quad (2.19)$$

Substituting a'' from (2.13) and a' from (2.16) in (2.19) gives the electron density,

$$n(y) = 3(1+a^2) + \frac{2\sqrt{1+a^2}}{\eta}(-\eta - a^2), \quad (2.20)$$

The electron density has its minimum at $y = 0$, $n_{min} = 1 - 4(\eta - 1)^2$. The electron density becomes zero when $\eta = 1.5$. Therefore partial evacuation happens when $1 < \eta < 1.5$. Calculating the total power for $\eta = 1.5$ will give the threshold evacuation power for one channel formation, a channeling power, P_{ch} , in 2D planar geometry

$$P_{ch} = \frac{2.84 \times 10^{14}}{\lambda(\mu m)} \sqrt{\frac{3n_{cr}}{2n_0} - 1} \text{ W/cm}. \quad (2.21)$$

Larger values of η give negative values for electron density. These cases, corresponding to a complete evacuation of plasma channels require careful theoretical analysis in order to ensure global charge conservation [20,24]. We will examine them in the next Section. For now only localized RSF solutions are discussed.

2.2.3 PIC Simulations

All simulations were performed using the PIC code Mandor [26] in a 2D3V mode in Cartesian geometry. We have used a Gaussian laser profile with a rise time of 200 fs and a constant amplitude afterwards. The laser is focused $2 \mu m$ from the left boundary. The plasma is homogeneous with densities between $0.001n_{cr} - 0.1n_{cr}$, and laser wavelength is $1 \mu m$. The spatial resolution in all simulations that were performed is $\Delta x = \Delta y = \lambda/15$ (λ is laser wavelength). Lengths in all graphs are in units of μm and times in fs units. The laser intensity is normalized by $I_0 = (m\omega_0 c/e)^2 c/4\pi$. The laser pulse is circularly polarized. Light is assumed to propagate along the x direction. The dimension of simulation box is $X \times Y = 900\mu m \times 100\mu m$. We have calculated the ion plasma period for different plasma densities in simulations and have limited the propagation distance accordingly except for plasma densities $0.1n_{cr}$ where ions are considered mobile. To illustrate the localized solutions due to RSF we have performed simulations with the following parameters: the plasma is homogeneous with a density $0.001n_{cr}$. The peak intensity of the Gaussian laser pulse is $3.8 \times 10^{18} W/cm^2$ and the full-width-half-maximum of the laser intensity is $15\mu m$ ($P \sim 0.67P_{ch}$). The laser enters the plasma from the left boundary and evolves towards a stationary localized solution. The power of the laser pulse is below the channeling power, P_{ch} (2.21), necessary to evacuate electron density. Figure 2.1 (a) shows the

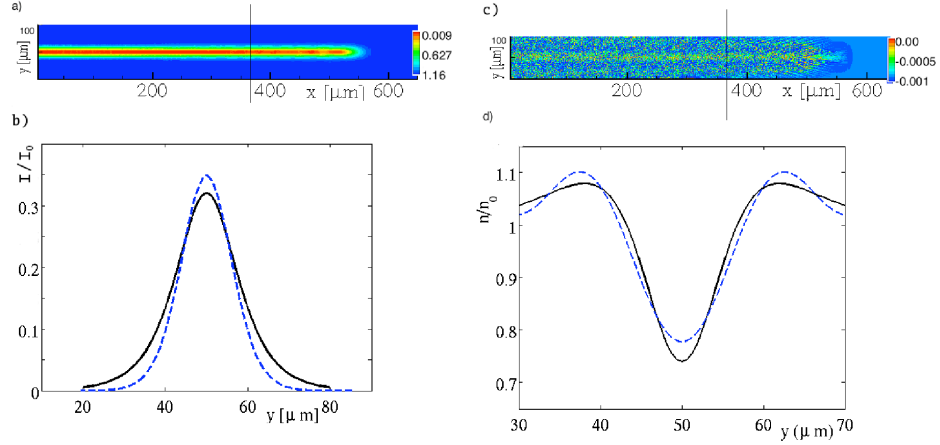


Figure 2.1 Contour plot of laser intensity (a). Comparison between analytical solution and simulation result (b), intensity calculated from analytical solution (solid curve) and laser intensity taken from transverse cut in simulation box (dashed curve). Contour plot of electron charge density normalized by n_c after propagating 1976 fs (c). Electron density calculated from analytical solution (solid-curve) and electron density taken from transverse cut in simulation box (dashed curve) (d)-straight lines show the position of the cut in the simulation box.

contour plot of the intensity profile of the laser pulse in the plasma at the time of 1976 fs. This panel displays the nonlinear state of the laser pulse of a constant cross-section supported by the density depletion shown in Fig. 2.1 (c). After the transient perturbations of the electron density and laser intensity in the front of the pulse which correspond to the rising pulse intensity, simulations show a stationary laser intensity profile. We have taken the transverse cross-section of intensity and density (at $x=370$ μm) and compared them with analytical solutions (2.18), (2.20) in Figs. 2.1b,d. As can be seen in the graphs, the channel is partially evacuated in the central region. The dashed-curve in (b) is the laser intensity taken from a transverse lineout in simulation box and the solid curve corresponds to the analytical solution (2.18). The dashed-

curve in (d) shows the electron density normalized by n_0 taken from simulations and the solid curve shows the corresponding analytical solution for electron density (2.20). The comparisons in Figs. 2.1 demonstrate good agreement between PIC simulations and theoretical results of Sec. 2.2.2. This is further confirmed in Fig. 2.2 where we have shown the location of stationary RSF solutions on the plane defined by two conserved quantities in the stationary model, constant η (minus Hamiltonian) (2.16) and the total power. The single point corresponds to the PIC simulation result from Fig. 2.1. In this particular case the initial power of the Gaussian beam has been almost completely captured in the nonlinear solution.

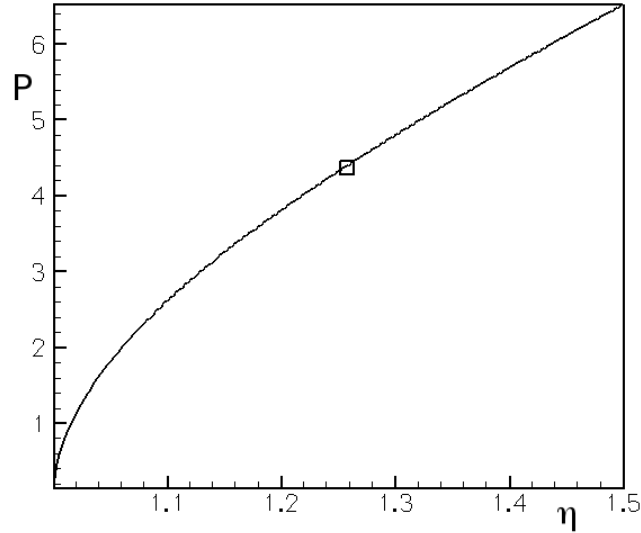


Figure 2.2 Dimensionless power ($\int_{-\infty}^{\infty} a^2 dy$) as a function of η . Graph shows the locus of stationary RSF solutions. The single point corresponds to the stationary PIC simulation solution from Fig. 2.1. The location of this point was calculated from the numerical results.

2.2.4 Stability of RSF Filaments

We have performed a linear stability analysis of the nonlinear stationary solutions for $a(y)$ (2.18) and $n(y)$ (2.20). Within the stationary approximation of Sec. 2.2.1 we rewrite the wave equation as:

$$i\frac{\partial a(x, y)}{\partial x} + \nabla_{\perp}^2 a(x, y) + \left(1 - \frac{\eta n}{\gamma}\right) a(x, y) = 0 \quad (2.22)$$

where x and y are in units of $[(k_0^2/2h)(n_0/n_{cr})]^{-1}$ and $[k_0\sqrt{1 - h^2/k_0^2}]^{-1}$ respectively and the amplitude $a(x, y)$ of the vector potential (2.7) varies also along x-direction.

We seek a solution to (2.22) in the following form:

$$a(x, y) = a_s(y) + a_+(x, y)e^{ily} + a_-(x, y)e^{-ily}, \quad (2.23)$$

where the amplitudes of the perturbations are small, $a_s(y) \gg |a_{\pm}(x, y)|$, l is a transverse wave vector and $a_s(y)$ is the analytical solution of the stationary model a (2.18) for $\eta < 1.5$. Substituting (2.23) in (2.22) and linearizing it gives two coupled differential equations for a_+ and a_- :

$$\begin{aligned} \left(i\frac{\partial}{\partial x} + R\frac{\partial^2}{\partial y^2} + Q\frac{\partial}{\partial y} - W\right)a_{\pm} &= \left((1 - R)\frac{\partial^2}{\partial y^2} \right. \\ &\left. + (2il - Q)\frac{\partial}{\partial y} - \left(W - l^2 + 1 - \frac{\eta n_s}{\gamma_s}\right)\right)a_{\mp}^* \end{aligned}$$

where $R = 1 - \eta(a_s(y)/\gamma_s)^2/2$ and the operators Q and W are defined by:

$$Q = 2il - \eta\frac{a_s(y)}{\gamma_s}\frac{\partial}{\partial y}\left(\frac{a_s(y)}{\gamma_s}\right) - il\eta\left(\frac{a_s(y)}{\gamma_s}\right)^2$$

$$W = l^2 - 1 - \frac{a_s^2(y)n_s}{2\gamma_s^3} + \frac{\eta a_s(y)}{2\gamma_s}\frac{\partial^2 a_s(y)}{\partial y^2} + il\eta\frac{a_s(y)}{\gamma_s}\frac{\partial a_s(y)}{\partial y} + \frac{\eta n_s(y)}{\gamma_s}$$

Equations for a_{\pm} are solved numerically assuming $a_{\pm} = (u_{\pm}(y) + iv_{\pm}(y))e^{\Gamma x}$. This yields a boundary value problem (cf. Ref. [28]). Boundary conditions are chosen as

$a_{\pm} |_{y=0,\infty} \rightarrow 0$. Such a choice leads in the nonlinear stage of the instability to a splitting of the solution into at least two filaments. Figure 2.3 shows gain coefficients Γ corresponding to the unstable transverse perturbations of the stationary solutions a_s (2.18) for $\eta=1.3, 1.4$ and 1.49 as functions of the wave number l . All nonlinear filaments are unstable for $\eta < 1.5$, i.e. without full electron evacuation, against transverse perturbations. However for low densities the characteristic gain length $1/\Gamma$ can be very long. For example, results shown in Figs. 2.1 at $n/n_{cr} = 0.001$ and $\eta = 1.26$ correspond to a gain length of approximately $5300 \mu\text{m}$. This distance is too long for the instability to affect the RSF solution in the simulation of Fig. 2.1. On the other hand the same $\eta = 1.26$ at $n/n_{cr} = 0.1$ corresponds to a gain length of $50 \mu\text{m}$. This is consistent with the splitting of the filament into two in simulations discussed later in the paper. For larger values of η , the maximum gain is smaller and disappears at $\eta = 1.5$.

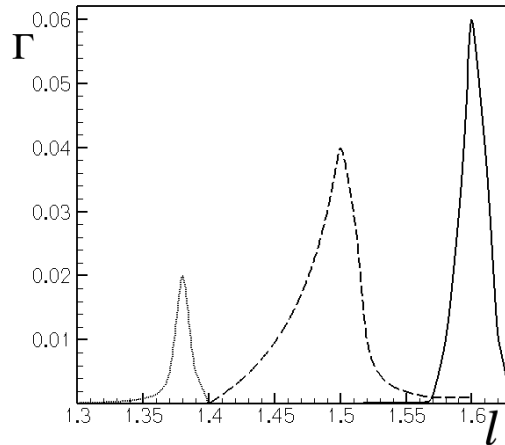


Figure 2.3 Gain coefficient (Γ) as a function of wavenumber for $\eta = 1.3$ (solid curve), 1.4 (dashed curve) and 1.49 (dotted curve).

2.3 Channelling of the Laser Pulse

The stationary analytical solution in the previous Section gives a negative density for electrons for $\eta > 1.5$. In order to construct a solution in this regime, we assume that the electrons are fully evacuated and the laser forms the channel where the ponderomotive force is balanced by the electrostatic force of the positive ions. As discussed in the introduction, much work has been devoted to the laser pulse channeling. We give below a summary of the analytical results discussed in Ref. [24]. PIC simulations which reproduce stationary channels follow in the next subsection. Finally we describe the destruction of channels due to surface waves on the channel walls and electron acceleration.

2.3.1 Analytical Theory

For powers greater than channeling power $P > P_{ch}$, complete evacuation will happen according to the stationary model. The ponderomotive force is strong enough to push all the electrons away from central region, making an ion channel where the laser pulse is trapped. Given the plasma background density, the increasing trapped laser power corresponds to a larger transverse size of the channel. The corresponding solution consists of two parts: an evacuated channel free of electrons and the outside plasma regions. For the plasma outside the channel we have the same solution as before, cf. (2.18), while for the evacuated region the vacuum Hamiltonian can be found using

$$a'' + a = 0, \tag{2.24}$$

Following the method of Sec. (4.2), gives $g(a) = 1$ and $V(a) = \frac{1}{2}a^2$. Therefore the vacuum Hamiltonian will be

$$H_V = \frac{1}{2}(a'^2 + a^2), \quad (2.25)$$

and the solution inside the channel can be found by integrating (2.25):

$$a_{ch} = C \cos(y - \chi), \quad (2.26)$$

where $C^2 = a_d^2 + a'_d{}^2$ and a_d is the field amplitude at the boundary, a'_d is the derivative of the field at the boundary (y_d), and χ gives the peak position of a . Therefore the total power can be determined:

$$P = \int_{-\infty}^{y_d} a_{plasma}^2 dy + \int_{-y_d}^{y_d} a_{ch}^2 dy + \int_{y_d}^{\infty} a_{plasma}^2 dy, \quad (2.27)$$

The channel width can be evaluated by integrating Poisson's equation over the whole interval:

$$\eta \int_{-\infty}^{\infty} (n - 1) dy = -2\eta \int_0^{y_d} dy + 2 \int_{y_d}^{\infty} \gamma'' dy = 0, \quad (2.28)$$

Thus:

$$y_d = -\frac{\gamma'}{\eta}, \quad (2.29)$$

where prime is the derivative with respect to y .

$$y_d = -\frac{1}{\eta} \frac{a_d a'_d}{\sqrt{1 + a_d^2}}, \quad (2.30)$$

Using $y_d = -\arctan \frac{a'_d}{a_d}$ and (2.30),

$$\begin{aligned} \tan \left[\frac{a_d (2\eta (\sqrt{1 + a_d^2} - 1) - a_d^2)^{1/2}}{\eta} \right] = \\ \frac{\sqrt{1 + a_d^2}}{a_d} ((2\eta (\sqrt{1 + a_d^2} - 1) - a_d^2)^{1/2}), \end{aligned} \quad (2.31)$$

By knowing η and using (2.31), a_d can be calculated and then (2.17) will give a'_d

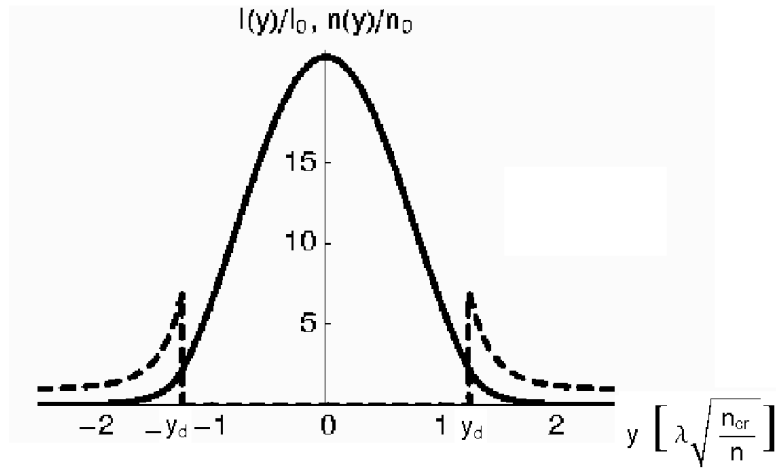


Figure 2.4 Schematic graph of analytical single channel solution, showing intensity distribution (solid curve) and electron density normalized by n_0 (dashed-curve).

and (2.30) will give y_d . A solution to this problem is unique: for every $\eta (> 1.5)$ there is only one value for the power per length and only one value for channel width. Figure (2.4) shows the schematic graph of a single channel analytical solution for $\eta = 4.5$. The solid curve shows the intensity distribution and the dashed curve shows the electron charge density.

2.3.2 PIC Simulations

We have performed several 2D PIC simulations for different background plasma densities, incident laser spot sizes and laser powers. We have found that in a wide range of low plasma densities, the incident Gaussian pulse with a power above the channelling power P_{ch} (2.21) reaches a quasi-stationary state which compares very well with stationary solutions from Sec. 2.3.1. Such a solution is illustrated in Fig. 2.4. With a proper normalization of the channel width y_d by $\lambda(n_{cr}/n_0)^{1/2}$ we can generate a

single curve in Fig. 2.5 describing the power trapped in the analytical solution of Sec. 2.3.1 as function of $2y_d$ for all plasma densities. Different PIC runs that have reached stationary states are shown by dots. Figure 2.5 shows that the trapped power and the size of the channel are in a very good agreement with our analytical predictions. For

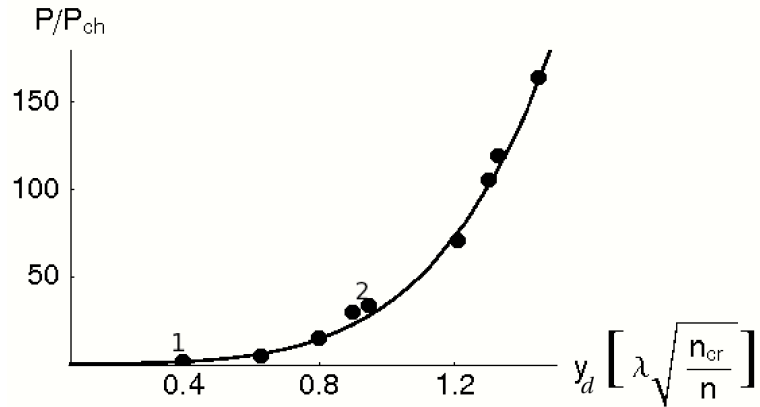


Figure 2.5 Solid line shows the exact analytical solution and circles show the simulation results for one channel. Numbers 1 and 2 corresponds to two simulations illustrated in Sec. 2.3.2.

the incident Gaussian pulse which has initial power and the spot size different from parameters of the stationary solutions in Fig. 2.5 the evolution towards these asymptotic states have involved focusing or defocusing of the laser pulse so it reaches the right width of the stable channel, $2y_d$. We will illustrate this below by two examples where the initial Gaussian laser pulses reach the RSF solutions of Fig. 2.5 without the loss of power. Depending on plasma density, the very front of the pulse can undergo a complicated nonlinear evolution involving the acceleration of electrons, scattering instabilities, self-modulations, etc. [10, 13, 29]. All these processes could lead to laser energy absorption. However, with the rapid increase of the laser power to its clamped

value higher than the channeling power, P_{ch} , these nonlinear processes are localized at the front of the pulse and suppressed in the evacuated channel. It is in this region where the laser intensity assumes constant value that we have identified stationary solutions.

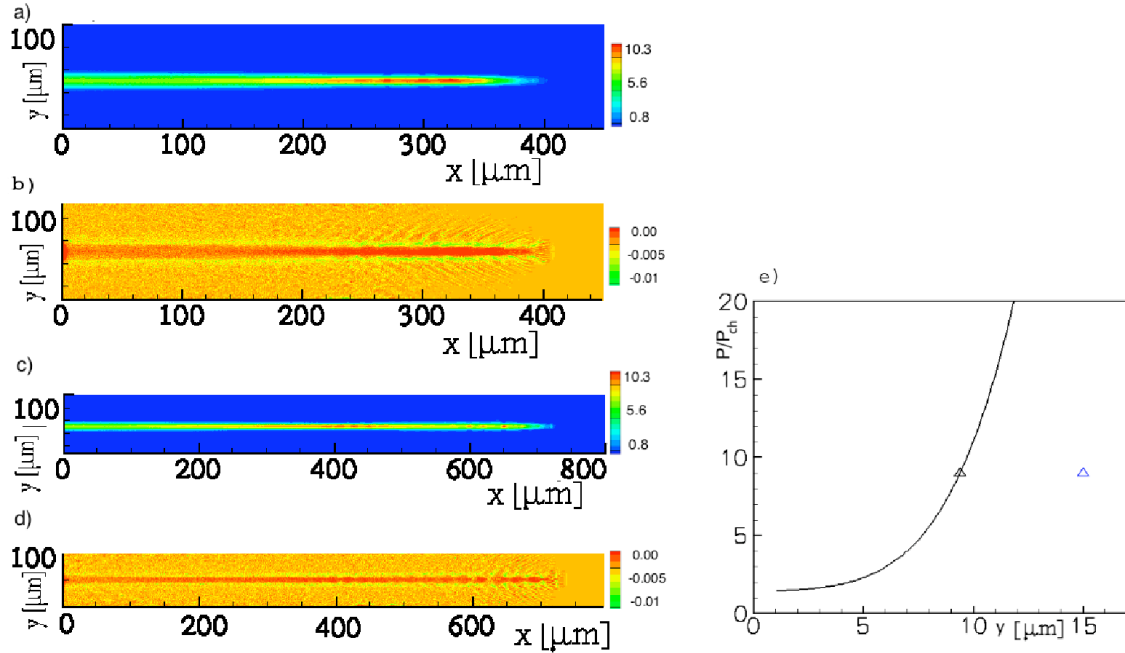


Figure 2.6 (Color online) Contours of laser intensity (a,c) and electron charge density (b,d) normalized by n_c for $t=1411$ fs and $t=2540$ fs. Solid curve in (e) shows the analytical solution of P/P_{ch} vs full channel width y in μm for corresponding plasma density. The triangle shows the input parameters: laser power and FWHM of the laser intensity and the triangle is the calculated power and channel width taken from transverse cut at $x = 408\mu m$, $t=2540$ fs.

Two examples of PIC simulations illustrate the evolution of the initial Gaussian laser pulses towards channeling solutions. Figures 2.6 show simulation results for a homogeneous plasma density of $0.005n_{cr}$, the peak laser intensity is $7.0 \times 10^{19} W/cm^2$ and

the initial full-width-half-maximum of the laser intensity is $15 \mu m$. Figures 2.6 show the contour plots of laser intensity (a),(c) and electron charge density (b),(d) after propagating 1411 fs and 2540 fs, respectively. Here the initial laser spot size is bigger than the predicted channel width, therefore the pulse first self focuses, decreasing the spot size and forming a stable channel. The solid curve in Fig. 2.6e shows the analytical solution of P/P_{ch} vs. full channel width, $2y_d$, for plasma density $0.005n_{cr}$. The star represents the input power and the initial full-width-half-maximum of the laser intensity. The triangle represents the calculated power and channel width taken from transverse lineout in simulation box. The laser power is $7.0 \times P_{ch}$ and the evacuated channel width is $8.4 \mu m$. For incident powers above channel power for evacuation, if the the laser spot size is bigger than the expected channel width (like the case above), then the pulse first adjusts itself, self-focuses and then the channel becomes stable, cf. Fig. 2.6. Figure 2.7 shows another comparison between PIC simulation results and the stationary solution for the intensity and density cross-sections. The agreement is quite accurate. Figures 2.8 show another simulation result where the homogeneous plasma density is $0.001n_{cr}$, the peak laser intensity is $5.0 \times 10^{20} W/cm^2$ and the initial full-width-half-maximum of the laser intensity is $10 \mu m$. Figures 2.8a,c show the contour plots of intensity profile of the laser and Figs. 2.8b,d the density profile of electrons. At the relatively high power and intensity of the incident pulse the channel is formed after the nonlinear interaction at the front of the pulse resulting in heating of electrons. The ponderomotive force pushes the electrons away from regions with higher laser intensity making a completely evacuated channel. The width of the channel is $30.1 \mu m$. The laser power is $23.0 \times P_{ch}$. In this example, the initial laser spot size is smaller than the expected channel width (Figs. 2.8, 4.10), therefore the laser pulse first adjusts itself, in this case broadens, increasing the spot size and then

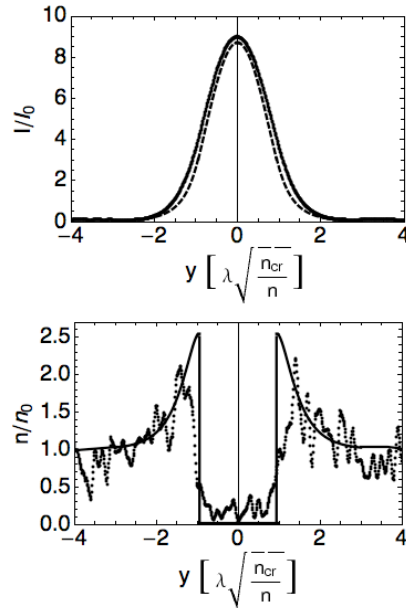


Figure 2.7 Lineouts of laser intensity and electron density normalized by N_0 along transverse direction (cut at $x = 408\mu m$, $t=2540$ fs). Solid curves show the exact analytical solutions and dashed curves are calculated laser intensity and electron density taken from transverse cut in simulation box.

the channel becomes stable, (see Figs. 2.8, 2.9). The solid curve in Fig. 2.8e shows the P/P_{ch} vs full channel width $2y_d$ for plasma density $0.001n_{cr}$. The star represents the input power and the initial full-width-half-maximum of the laser intensity. The triangle represents the calculated power and channel width taken from a transverse lineout in the simulation box. Figure 2.9 shows the input laser intensity (solid curve), laser intensity calculated from data taken from a transverse cut in simulation box after the head of the laser pulse propagated $x = 250 \mu m$ (dash-dotted curve) and electron charge density taken from the same data (dotted curve). We can see from the graph that the laser pulse is broadened in this case and channel is completely evacuated.

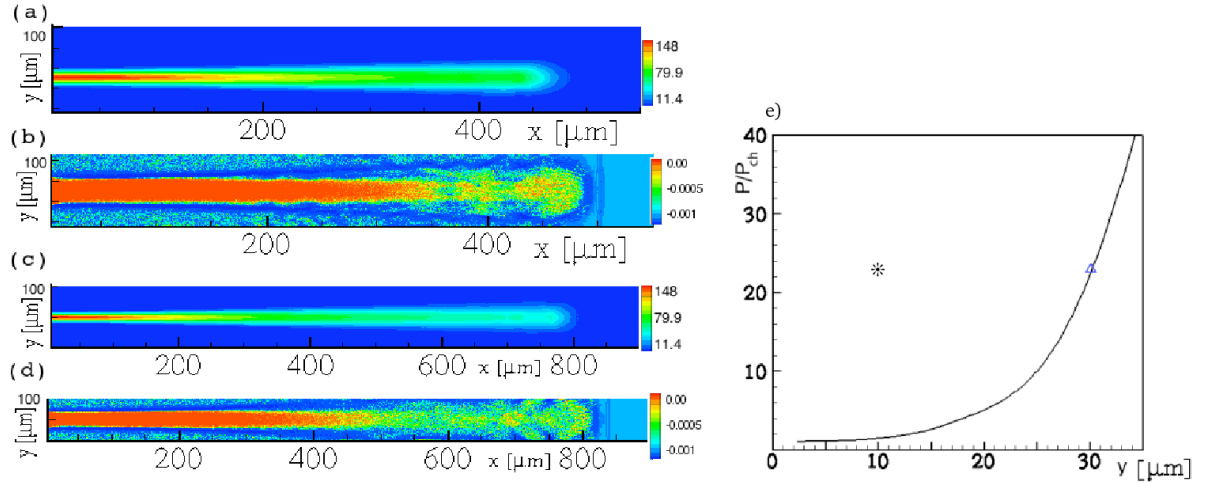


Figure 2.8 Contours of laser intensity (a,c) and electron charge density (b,d) normalized by n_c for $t=1693$ fs and $t=2823$ fs. Solid curve in (e) shows the P/P_{ch} vs full channel width y in μm for corresponding plasma density. The star shows the input parameters: laser power and FWHM of the laser intensity and the triangle is the calculated power and channel width taken from transverse cut at $x = 200\mu\text{m}$, $t = 1693$ fs.

An important feature in this simulation is that at the front of the pulse, we see clearly the rippling of the channel and the increase of the number of fast electrons inside the channel. We have interpreted these perturbations of the electron density and of the electromagnetic fields as the surface waves propagating on the walls of the plasma channels [30]. The next subsection will address the mechanism of electron acceleration in the evacuated channels due to the interaction with surface waves.

2.3.3 Surface Waves Excitation

Figure 2.10a shows the longitudinal momentum of fast electrons in units of mc in $x - y$ plane at $t=847$ fs. These particles are accelerated during interaction with

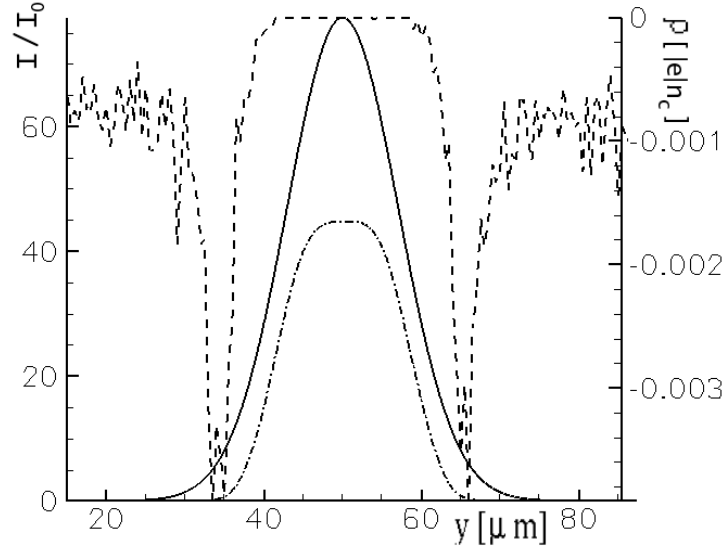


Figure 2.9 Solid line shows the input intensity of the laser and the dash-dotted line taken from a transverse cut ($x = 200\mu m, t = 1693fs$) in simulation box at showing the intensity of the laser in plasma. The dashed curve is the electron charge density taken from the same cut, clearly shows the evacuated channel.

the electrostatic component of the surface waves that are excited on the walls of the plasma channel. The wavelength of the electron bunches on the channel edges is longer than the homogeneous plasma wavelength $\lambda_p = 2\pi c/\omega_p = 33\mu m$ and it corresponds to the surface wave perturbation.

The wavelength of the bunching has been calculated for the weakly relativistic regime [10, 30]: a short laser pulse can drive a large amplitude wake at the edges of an evacuated channel over long distances. The effect of a nonzero thickness boundary was discussed in the same paper. It was shown that for a given plasma density, the wavelength of the wake for sharp boundaries is $\lambda_p\sqrt{1 + k_p\bar{y}_d}$ where k_p is plasma

wavenumber and $2\bar{y}_d$ is the dimensional width of the evacuated channel. The more realistic case of finite thickness boundary was studied by Shvets *et al.* [31]. Although we have used a clamped laser pulse in all our simulations, the laser pulse has a rise time of 200 fs before intensity reaches its constant value. In this case, the surface waves on the edges of the channel are excited by the longitudinal ponderomotive force due to increasing intensity of the laser in the front of the pulse. The excited wakes are driven to the wave breaking amplitude and accelerate electrons at the edges of the channel. Eventually energetic electrons fill up the channel and the evacuation will be lost (Fig. 2.10b).

Our simulations are in the relativistic regime. To find the wavelength of the surface waves and electron bunches, we will generalize to the relativistic intensities ($a > 1$) the theory of Ref. [30]. We are assuming an evacuated channel in the slab geometry. In order to be able to calculate the wavelength of the excited wakes on the boundaries of the channel, we assume that the thickness of the boundary is zero. We rewrite (2.1) introducing electric field as $\mathbf{E} = -c^{-1}\partial\mathbf{A}/\partial\mathbf{t} - \nabla\varphi$:

$$\nabla(\nabla\cdot\mathbf{E}) - \nabla^2\mathbf{E} + \frac{1}{c^2}\frac{\partial^2\mathbf{E}}{\partial t^2} = -\frac{4\pi}{c^2}\frac{\partial\mathbf{J}}{\partial t} \quad (2.32)$$

where $\mathbf{E}(y)e^{i(k_x x - \omega t)}$ is the electric field, k_x is the wave number of the surface mode, $\mathbf{J} = -en_0\mathbf{v}$ outside the channel and zero inside. Using the same equations as in Subsec. 2.2.1, we have:

$$\frac{\partial\mathbf{v}}{\partial t} = -\frac{e}{\gamma m}\mathbf{E} + \frac{\mathbf{f}}{\gamma m} \quad (2.33)$$

where $\mathbf{f} = -mc^2\nabla\gamma$ is the ponderomotive force. Substituting (2.33) in (2.32) gives:

$$\nabla(\nabla\cdot\mathbf{E}) - \nabla^2\mathbf{E} + \frac{1}{c^2}\frac{\partial^2\mathbf{E}}{\partial t^2} = -\frac{4\pi e^2}{\gamma m_e c^2}n_0\mathbf{E} + \frac{4\pi en_0}{\gamma m c^2}\mathbf{f} \quad (2.34)$$

We can find the wake modes from (2.34) by setting $f = 0$. Rewriting (2.34) with

$f = 0$ gives,

$$\nabla(\nabla \cdot \mathbf{E}) - \nabla^2 \mathbf{E} + \frac{1}{c^2} \frac{\partial^2 \mathbf{E}}{\partial t^2} + \frac{\omega_p^2}{\gamma c^2} \mathbf{E} = 0 \quad (2.35)$$

Assuming $\omega/k_x \approx c$, the wakefield solutions for inside the channel ($n_0 = 0$) are:

$$\tilde{E}_x(x, y, t) = A e^{i(k_x x - \omega t)} \quad (2.36)$$

$$\tilde{E}_y(x, y, t) = -\frac{ik_x}{k_0} \sqrt{\frac{\eta}{n_0/n_{cr}}} A y e^{i(k_x x - \omega t)} \quad (2.37)$$

Where A is a constant, y is in units of $k_p/\sqrt{\eta}$ and $\tilde{\mathbf{E}}$ is in units of $e/m\omega_0 c$. To find wakefield solutions in the plasma outside the channel, we first write the y-component of (2.35),

$$\left(\frac{k_p^2}{\gamma}\right) \tilde{E}_y = -ik_x k_0 \sqrt{\frac{n_0/n_{cr}}{\eta}} \frac{\partial \tilde{E}_x}{\partial y} \quad (2.38)$$

Substituting $\partial \tilde{E}_y/\partial y$ from (2.38) into x-component of (2.35) gives:

$$\frac{\partial}{\partial y} \left(\left(\frac{\gamma \omega^2}{\omega_p^2} - 1 \right) \frac{\partial \tilde{E}_x}{\partial y} \right) = -\frac{\eta}{n_0/n_{cr}} \frac{k_p^2}{\gamma k_0^2} \left(\frac{\gamma \omega^2}{\omega_p^2} - 1 \right) \tilde{E}_x \quad (2.39)$$

where γ is given by:

$$\gamma = \frac{\eta \cosh^2(\sqrt{\eta-1}(y-y_d)) + (\eta-1)}{\eta \cosh^2(\sqrt{\eta-1}(y-y_d)) - (\eta-1)} \quad (2.40)$$

which is calculated from (2.18). \tilde{E}_x in the plasma outside the channel is the solution to (2.39). To solve (2.39), we note that for all $\eta > 1.5$, $\partial\gamma/\partial y \ll \gamma$. Therefore to solve (2.39), we ignore $\partial\gamma/\partial y$. This is correct if $|(\partial\gamma/\partial y)/\gamma| \ll |(1 - \omega_p^2/\gamma\omega^2)\partial^2\tilde{E}_x/\partial y^2)/(\partial\tilde{E}_x/\partial y)|$. We will show later that this is a correct assumption. Considering the above approximation, the solution to (2.39) can be found numerically. By fitting the numerical solution with an analytic function, we find $\tilde{E}_x \approx D e^{-\delta(|y|-y_d)} e^{i(k_x x - \omega t)}$ where $(D, \delta > 0)$ are constants. For $1.51 \leq \eta \leq 4$, we find $1.1 \leq \delta \leq 2.0$ for $n_0/n_{cr} = 0.001$ and $1.08 \leq \delta \leq 1.98$ for $n_0/n_{cr} = 0.1$. We can see

that the range of δ remains almost the same for the plasma densities considered in this paper. By matching the boundary conditions for longitudinal component of the electric field, we find $A = D$. The normal component of the displacement vector at $y = \pm y_d$ is continuous, therefore,

$$-\frac{1}{k_0^2} \frac{\eta}{n_0/n_{cr}} y_d = \left(1 - \frac{\omega_p^2}{\bar{\gamma}\omega^2}\right) \frac{\bar{\gamma}c^2}{\omega_p^2} \frac{\delta\bar{\gamma}}{k_p^2} \quad (2.41)$$

and the following dispersion relation can be found:

$$\omega = \frac{\omega_p}{\bar{\gamma}} \frac{1}{\sqrt{1 + \frac{y_d\eta}{\bar{\gamma}\delta}}} \quad (2.42)$$

and the wavelength of the surface wake will be:

$$\lambda_s = \lambda_p \sqrt{\bar{\gamma}} \sqrt{1 + \frac{y_d\eta}{\bar{\gamma}\delta}} \quad (2.43)$$

where $\bar{\gamma}$ is calculated at the channel boundary and y_d is in units of $k_p/\sqrt{\eta}$. Now we check the validity of $|(\partial\gamma/\partial y)/\gamma| \ll |(1 - \omega_p^2/\gamma\omega^2)(\partial^2\tilde{E}_x/\partial y^2)/(\partial\tilde{E}_x/\partial y)|$. For all $\eta > 1.5$, the largest value of γ and $|\partial\gamma/\partial y|$ happen at the boundary y_d . For instance for $\eta = 1.51$, $|\partial\gamma/\partial y/\gamma| = 0.1$ at the boundary which gives the largest value and $|(1 - \omega_p^2/\gamma\omega^2)\partial^2\tilde{E}_x/\partial y^2/\partial\tilde{E}_x/\partial y| \approx 1$. The inequality holds for all $\eta > 1.5$ in the plasma region.

We have calculated the wavelength of bunching (2.43) for the above simulation (cf. Fig. 2.10) ($\eta = 2.2$, $\bar{\gamma} = 2.0$, $\delta \approx 1.5$) and the result is $\lambda_s = 75.0\mu m$. This is in a good agreement with the rippling wavelength in the simulation. The electrons are bunched on the edges of the channel at distances of λ_s as can be seen in Fig. 2.10a. In weakly relativistic regime, (2.43) gives the same value for the wavelength as in Refs. [10, 30]. The maximum value of $k_{||}/k_0$ calculated from the spectrum of the longitudinal electric field at the edges of the channel is 0.014 which corresponds

to the surface wake wavelength, λ_s (2.43). The maximum energy of these electrons is 45 MeV. The electrons from the channel walls will be heated and gradually fill up the evacuated channel starting from the front of the laser pulse (Fig. 2.10b). Figure 2.10b shows the longitudinal momentum of the electrons in the transverse direction at $t=1695$ fs. These electrons are concentrated at the channel edges at earlier times and they start to fill the channel at later times. At the later time, the length of the completely evacuated channel becomes $400\mu m$, while the rest of the channel is 50% evacuated. The laser pulse broadens and the maximum intensity of the laser drops to 1/3 of maximum intensity in the evacuated channel. Electron density modulations and acceleration due to interaction with the surface modes could provide an explanation for the experimental observation of relativistic electrons during the interaction of PW pulses with gas jet targets [6]. This mechanism could also be responsible for the injection of fast electrons into the laser pulse thus enabling direct acceleration of electrons.

The excitation of the surface waves depends on the rise time of the laser pulse. If the ascending part of the laser pulse is shorter than the wavelength of the surface mode on the channel edges, the longitudinal ponderomotive force at the front of the pulse will act as the source for the surface wave (cf. Ref. [30]). Increasing the plasma density will lead to smaller wavelengths λ_s and a less effective coupling between the laser pulse and the surface modes. At higher background plasma densities and for not fully evacuated channels the pulse could undergo hosing instability. The resulting intensity modulations can also excite surface waves, in particular an asymmetric mode as shown in [10].

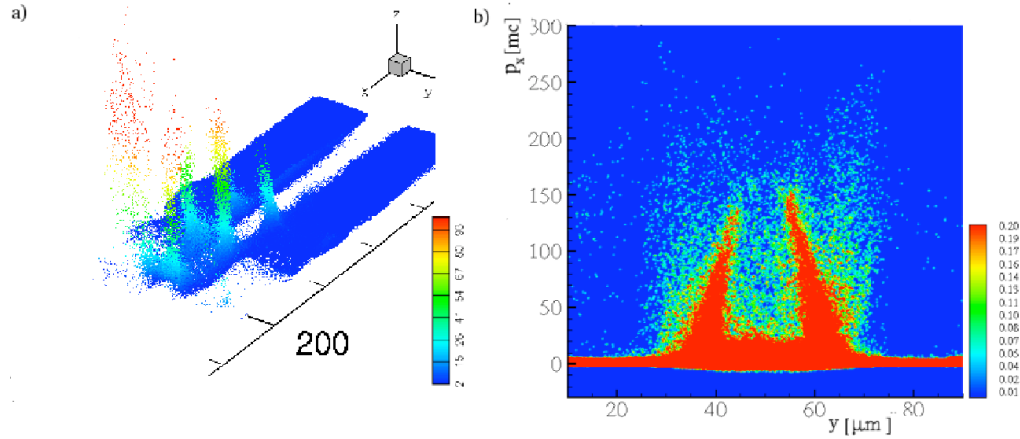


Figure 2.10 (Color online) Longitudinal momentum of electrons in units of mc in $x - y$ plane for $t=847$ fs (a) and longitudinal momentum of electrons in units of mc averaged over x in transverse direction at $t=1695$ fs (b).

2.3.4 High Density Regime

Surface wave excitation and electron heating dominates the long time evolution of laser filaments at lower densities, $n \leq 0.01n_{cr}$. At higher densities, $n \approx 0.1n_{cr}$, we could not reach the channeling solutions as predicted by the stationary theory of Subsec. 2.3.1. To gain further insight into properties of these theoretical solutions for single filaments we have plotted the graph from Fig. 2.5 in the dimensional form for different plasma densities in Fig. 2.11. Figure 2.11 shows the total power vs channel width for densities $0.001n_{cr}$ (solid curve), $0.01n_{cr}$ (dashed curve) and $0.1n_{cr}$ (dash-dotted curve). For the same total power we get different channel widths, smaller channels for higher plasma densities. Figure 2.11 also demonstrates that increasing P/P_{ch} for each density will lead to a wider channel. At higher densities, such as $0.1n_{cr}$ the transverse width of the channel approaches the laser wavelength where the paraxial approximation used in the derivation of the analytical results fails. It is also

clear that the transverse instability of RSF filaments of Subsec. 2.2.4 becomes very effective at higher electron densities and can compete with the channel formation by splitting RSF filaments into two structures. This is illustrated in Fig. 2.12 at time $t = 864$ fs and plasma density $0.1n_{cr}$. The laser peak intensity is $4.3 \times 10^{19} \text{ W/cm}^2$ and the initial full-width-half-maximum of the laser intensity is $8 \mu\text{m}$ ($P/P_{ch} = 16$). The laser pulse self-focuses after the head of the pulse has propagated a distance of approximately $60 \mu\text{m}$. However there is no evacuation of electron density and no channel formation. Instead laser pulse relaxes to a broad structure supported by the density depletion which subsequently becomes unstable to transverse modulations producing two filaments after laser propagation over a distance of $200 \mu\text{m}$. The splitting is shown in Fig. 2.12a. Figure 2.12b shows the laser intensity for two transverse cuts at $t=560$ fs ($x=119 \mu\text{m}$, dashed curve) and $t=846$ fs ($x=181 \mu\text{m}$, solid curve). The propagation length which is involved in the development of these two filaments is consistent with the linear gain length of the instability described before in Subsec. 2.2.4. At the later times ($t = 1411$ fs and 2540 fs) and after some power losses due to electron acceleration and laser light escaping the filament, Fig. 2.13 displays a hosing like behaviour of the laser beam (cf. Ref. [10]). The light starts to bend away from center after the head of the pulse has propagated a distance of $290 \mu\text{m}$. The predicted growth rate in the long wavelength regime is [32] $\gamma_h = (a/\sqrt{8})(c/\omega_0 w)k_h c = 0.003 \text{ fs}^{-1}$, where the spot size $w = 3 \mu\text{m}$ and $a = \sqrt{20}$ are taken from transverse lineout and $k_h = 2\pi/50 \mu\text{m}^{-1}$ is observed. The characteristic growth time of $\gamma_h^{-1} \sim 300$ fs is consistent with the simulation results. No stable electron evacuated channel forms in this and other similar runs with the same and higher densities. Because of the transverse instability and time dependent evolution of the self-focused relativistic pulses no stationary single channels have been recovered

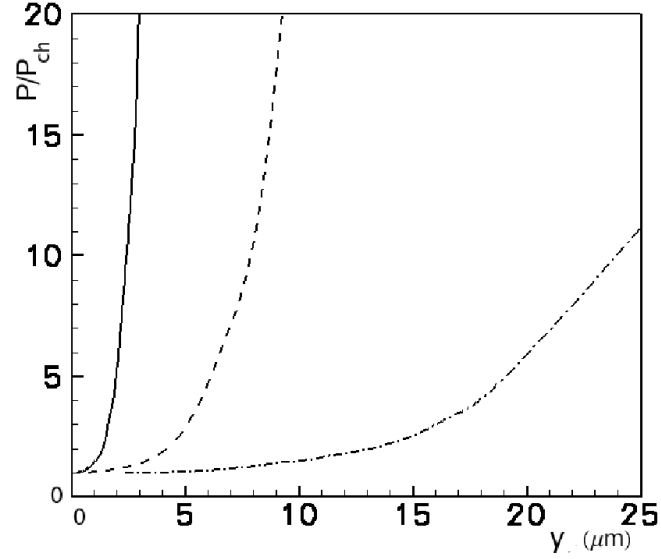


Figure 2.11 P/P_{ch} vs channel width y_d in μm for plasma densities $0.001n_{cr}$ (dash-dotted curve), $0.01n_{cr}$ (dashed curve) and $0.1n_{cr}$ (solid curve).

at these higher plasma densities $n \geq 0.1n_{cr}$.

2.4 Conclusions

We have studied relativistic self-focusing and laser pulse channelling in large-scale length underdense plasma by means of analytical theory and 2D PIC simulations. This research has been motivated by continuing interests in intense short pulse laser propagation in underdense plasmas for fusion [4], particle acceleration [6] and x-ray transport [5] applications. Numerous theoretical studies over the years [12,19–22] and in particular the Ref. [24] have provided the set of analytical results which are used together with PIC simulations in constructing different scenarios of RSF and laser

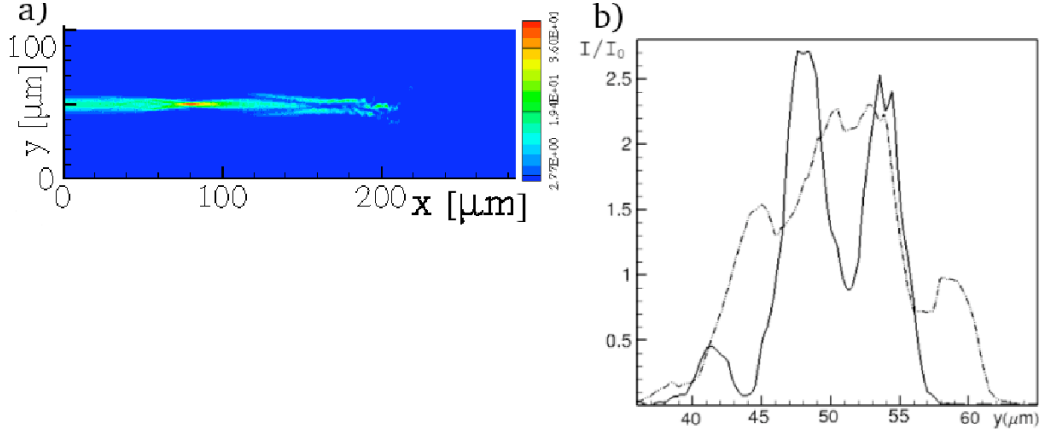


Figure 2.12 (Color online) Contour plot of laser intensity at $t=846$ fs (a) and Lineouts of laser intensity along transverse direction at $t=560$ fs ($x=119$ μm , dashed curve) and $t=846$ fs ($x=181$ μm) (b).

pulse channelling.

The most significant result of this paper is the demonstration that the single fully evacuated stationary channel solution due to RSF is a stable asymptotic state in PIC simulations. In the density range $0.001 < n_0/n_{cr} < 0.1$ and for the laser power above channelling power, P_{ch} (2.21), we were able to reproduce in PIC simulations the analytical curve from Fig. 2.5. This function describes the location of stationary analytical solutions in terms of captured power vs channel width. At higher densities, $n_0 \geq 0.1n_{cr}$, the stationary channels have the width on the order of the laser wavelength and require high laser powers to be formed.

The long term evolution of the fully evacuated filaments includes electron acceleration due to surface waves, of the wavelength $\lambda_s = \lambda_p \sqrt{\bar{\gamma}} \sqrt{1 + \frac{y_d \eta}{\bar{\gamma} \delta}}$ (2.43) (where $\bar{\gamma} = \sqrt{1 + a_d^2}$ is calculated at the channel boundary) that are excited on the walls of the channels. These hot electrons can eventually fill up the channel and lead to its destruction. Surface waves are excited by the coupling between longitudinal pon-

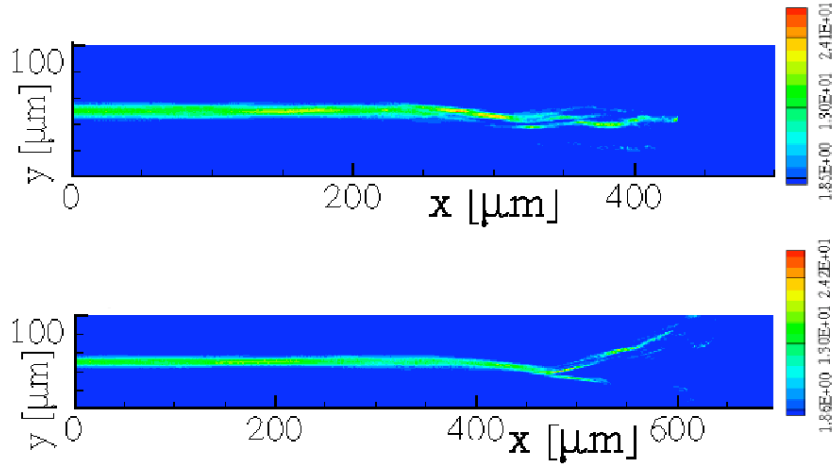


Figure 2.13 (Color online) Contour plots of laser intensity at $t=1411$ fs and 2540 fs. Plots show filamentation and bending of the laser light.

deromotive force of the ascending (or descending) portions of the laser pulse with the plasma on the walls of the channels.

Contrary to the case of fully evacuated channels, the soliton like RSF filaments without full electron evacuation (2.18) are unstable to transverse modulations, Fig. 2.3. This instability can be particularly effective at higher densities ($n_0 \geq 0.1n_{cr}$), where due to the very large gain factor it can compete with the evacuation process of the channelling laser pulses and break them up into separate filaments. This has been one of the reasons why we could not reach in our PIC simulations multi-filamentary stationary solutions from Ref. [24]. RSF filaments with nonzero electron density have been also unstable to hosing instability. Many qualitative features of our 2D results are also taking place in more realistic 3D simulations. They will be the topic of the next Chapter.

Bibliography

- [1] M. Tabak, J. Hammer, M. E. Glinsky, W. L. Kruer, Scott C. Wilks, J. Woodworth, E. M. Campbell, M. D. Perry and R. J. Mason, *Phys. Plasmas* **1**, 1626 (1994).
- [2] Z. Najmudin, K. Krushelnick, M. Tatarakis, E. L. Clark, C. N. Danson, V. Malka, D. Neely, M. I. K. Santala, A. E. Dangor, *Phys. Plasmas* **10**, 438 (2003).
- [3] M. Borghesi, A. J. MacKinnon, L. Barringer, R. Gaillard, L. A. Gizzi, C. Meyer, O. Willi, A. Pukhov, and J. Meyer-ter-Vehn, *Phys. Rev. Lett.* **78**, 879 (1997).
- [4] G. Li, R. Yan, C. Ren, T.-L. Wang, J. Tonge, and W. B. Mori, *Phys. Rev. Lett.* **100**, 125002 (2008).
- [5] J. Davis, G. M. Petrov, and A. L. Velikovich, *Phys. Plasmas* **12**, 123102 (2005).
- [6] S. P. Mangles, B. R. Walton, M. Tzoufras, Z. Najmudin, R. J. Clarke, A. E. Dangor, R. G. Evans, S. Fritzler, A. Gopal, C. Hernandez-Gomez, W. B. Mori, W. Rozmus, M. Tatarakis, A. G. Thomas, F. S. Tsung, M. S. Wei, and K. Krushelnick, *Phys. Rev. Lett* **94**, 245001 (2005)
- [7] A. Pukhov, Z.-M. Sheng, J. Meyer-ter-Vehn, *Phys. Plasmas* **6**, 2847 (1999).

-
- [8] G. Shvets, and J. S. Wurtele, *Phys. Rev. Lett* **73**, 3540 (1994).
- [9] G. Shvets and X. Li, *Phys. Plasmas* **8**, 8 (2001).
- [10] N.M. Naumova, J. Koga, K. Nakajima, T. Tajima, T. Zh. Esirkepov, S. V. Bulanov, and F. Pegoraro, *Phys. Plasmas* **8**, 4149 (2001).
- [11] C.D. Decker, W. B. Mori, K.-C. Tzeng, and T. Katsouleas, *Phys. Plasmas* **3**, 2047 (1996).
- [12] A. B. Borisov, J.W. Longworth, K. Boyer, and C. K. Rhodes, *Proc. Natl. Acad. Sci. USA* **95**, 7854 (1998); A.B. Borisov, O. B. Shiryayev, A. McPherson, K. Boyer and C. K. Rhodes, *Plasma Phys. Control. Fusion* **37**, 569 (1995)
- [13] K.-C. Tzeng and W. Mori *Phys. Rev. Lett* **81**, 104 (1998).
- [14] E. Esarey, C. B. Schroeder, B. A. Shadwick, J. S. Wurtele, and W. P. Leemans, *Phys. Rev. Lett* **84**, 3081 (2000).
- [15] G. A. Askar'yan, *Sov. Phys. JETP* **15**, 168 (1962).
- [16] R. Y. Chiao, E. Garmire, and C. H. Townes, *Phys. Rev. Lett.* **13**, 479 (1964).
- [17] A. G. Litvak, *Sov. Phys. JETP* **30**, 344 (1969).
- [18] C. Max, J. Arons and A. B. Langdon, *Phys. Rev. Lett* **33**, 209 (1974).
- [19] Gou Zheng Sun, E. Ott, Y. C. Lee and P. Gudzar, *Phys. Fluids* **30**, 526 (1987).
- [20] M. D. Feit, A. M. Komashko, S. L. Musher, A. M. Rubenchik, and S. K. Turitsyn, *Phys. Rev. E* **57**, 7122 (1998).
- [21] T. Kurki-Suonio, P. J. Morrison, and T. Tajima, *Phys. Rev. A* **40**, 32302 (1989)

-
- [22] X. L. Chen and R. N. Sudan, *Phys. Fluids. B* **5**, 1336 (1993)
- [23] P. Sprangle, Cha-Mei. Tang, E. Esarey, *IEEE Trans. on Plasma Sci.* **15**, 145 (1987).
- [24] F. Cattani, A. Kim, D. Anderson, and M. Lisak, *Phys. Rev. E* **64**, 016412 (2001)
- [25] A. Kim, M. Tushentsov, F. Cattani, D. Anderson, and M. Lisak, *Phys. Rev. E* **65**, 036416 (2002)
- [26] D. Romanov, V. Yu. Bychenkov, W. Rozmus, C. E. Capjack and R. Fedosejevs, *Phys. Rev. Lett* **93**, 215004 (2004)
- [27] V.I. Berezhiani, S.M. Mahajan, Z. Yoshida, and M. Pekker, *Phys. Rev.* **E65**, 046415 (2002).
- [28] W. J. Firth, D. V. Skryabin, *Phys. Rev. Lett.* **79**, 2450 (1997)
- [29] E. Esarey, J. Krall and P. Sprangle, *Phys. Rev. Lett.* **72**, 2887 (1994).
- [30] T. C. Chiou, T. Katsouleas, C. Decker, W. B. Mori, J. S. Wurtele, G. Shvets and J. J. Su, *Phys. Plasmas* **2**, 310 (1995)
- [31] G. Shvets, J. S. Wurtele, T. C. Chiou, T. Katsouleas, *IEEE Trans. Plasma. Sci* **24**, 351 (1996)
- [32] B. J. Duda and W. B. Mori, *Phys. Rev. E* **61**, 1925 (2000); B. J. Duda, R. G. Hemker, K. C. Tzeng, and W. B. Mori, *Phys. Rev. Lett.* **83**, 1978 (1999)

Chapter 3

Self-Focusing, Channeling and Particle Acceleration by Relativistic Laser Pulses in 3D Geometry

3.1 Introduction

Propagation of intense laser pulses in large scale underdense plasma has been an important subject for advanced applications such as inertial confinement fusion [1], particle acceleration [2] and radiation sources. The interesting and basic nonlinear physics of relativistic self-focusing (RSF) and self-channelling of intense laser pulses has been a topic of ongoing theoretical, experimental and simulation studies [3–19]. Relativistic self-focusing happens if the laser power, P , exceeds the critical power

A version of this Chapter will be submitted to Physics of Plasmas. N. Naseri and W. Rozmus

$P_{cr} = 17\omega_0^2/\omega_p^2$ GW, where ω_0 is the laser frequency and ω_p is the plasma frequency [11]. For intense laser pulses the transverse ponderomotive force can be large enough to expel electrons from the central region leading to full electron evacuation [12–15]. This problem was first studied by Sun *et. al* [12] in cylindrical geometry. Later Feit *et. al* [13] showed that charge conservation was not satisfied in their model. Cattani *et. al* [14] and Kim *et. al* [15] studied this problem in 2D slab geometry and 3D cylindrical geometry, respectively. Their models satisfy the charge conservation by explicitly including Poisson’s equation. In our previous work, we studied channeling of intense laser pulses in underdense plasmas using 2D PIC code in large-scale plasmas. We found a limit on plasma density for complete evacuation to happen. We observed that for higher plasma densities hosing and transverse instability are the dominant effects. We also showed how the rise time of the laser pulse can affect the stability of the evacuated channels [19].

Higher dimensionality is very important in self focusing and self channeling of the laser pulses in underdense plasma and it leads to fundamental differences compared to 2D cases. 3D simulations by Pukhov *et. al* [6] showed that self focusing is much stronger in 3D than in 2D slab geometry. The purpose of this paper is to study channeling, ring structure and stability of the channels using 3D PIC codes Mandor [20] and SCPIC [21]. 3D simulations are more realistic. Moreover, azimuthal properties of the laser pulse can only be studied in 3D geometry. As we will show azimuthal perturbations can break the symmetry of the pulse and split the pulse into several filaments. The growth length of azimuthal instability is shorter for higher plasma densities. In what follows, first we review the theory of channeling in cylindrical geometry (Sec. 3.2,3.3). Then we illustrate the simulation results for single channelling and compare them with analytical solutions (Sec. 3.4). Surface wave excitation will be addressed in Sec.

3.5. Section 3.6 contains theoretical solutions for the ring structure. The results of simulations and the comparison with analytical solution are presented in Sec. 3.7. Stability of single channels and ring structure is studied in Sec. 3.8.

3.2 A Theoretical Model

The focus of our work is on the 3D PIC simulations of intense laser pulses interacting with a plasma under conditions where wakefields and scattering instabilities are not important. We will study RSF and channeling of short laser pulses using PIC simulations and examine first whether and under which conditions these numerical results approach the stationary solutions of a simplified theoretical model [12, 15, 17, 22]. This well established theoretical model includes the description of a cold, relativistic electron fluid interacting with a laser pulse that is described in the paraxial approximation. Assuming immobile ions, the basic equations of this model are:

$$\nabla^2 \mathbf{A} - \frac{1}{c^2} \frac{\partial^2 \mathbf{A}}{\partial t^2} = \frac{1}{c} \frac{\partial}{\partial t} \nabla \varphi + \frac{4\pi}{c} N e \mathbf{v}, \quad (3.1)$$

$$\nabla^2 \varphi = 4\pi e (N - N_0), \quad (3.2)$$

$$\frac{\partial \mathbf{p}}{\partial t} + (\mathbf{v} \cdot \nabla) \mathbf{p} = \frac{e}{c} \frac{\partial \mathbf{A}}{\partial t} + e \nabla \varphi - \frac{e}{c} \mathbf{v} \times (\nabla \times \mathbf{A}), \quad (3.3)$$

where N is the electron density, N_0 is the background density, $-e$ is electron charge, m is mass of electron, \mathbf{A} is an electromagnetic vector potential and φ is an electrostatic scalar potential. Using the equality

$$(\mathbf{v} \cdot \nabla) \mathbf{p} = mc^2 \nabla \gamma - \mathbf{v} \times (\nabla \times \mathbf{p}), \quad (3.4)$$

we can rewrite (3.3) as the equation for the canonical momentum $\mathbf{P}_c = \mathbf{p} - \frac{e}{c} \mathbf{A}$,

$$\frac{\partial \mathbf{P}_c}{\partial t} - \mathbf{v} \times (\nabla \times \mathbf{P}_c) = -mc^2 \nabla \gamma + e \nabla \varphi, \quad (3.5)$$

Operating with $\nabla \times$ on Eq. (3.5) we derive the equation for the generalized vorticity,

$$\mathbf{\Omega} = \nabla \times \mathbf{P}_c,$$

$$\frac{\partial \mathbf{\Omega}}{\partial t} - \nabla \times (\mathbf{v} \times \mathbf{\Omega}) = \mathbf{0}. \quad (3.6)$$

It can be shown [17,23] using Eq. (3.6) that if $\mathbf{\Omega} = \mathbf{0}$ everywhere at some initial time then $\mathbf{\Omega}$ remains zero at later times. The generalized vorticity vanishes initially in our cold electron plasma in the absence of a laser pulse. Because of $\nabla \times (\mathbf{p} - \frac{e}{c}\mathbf{A}) = 0$ we can introduce a scalar function ψ and write

$$\gamma m \mathbf{v} = \frac{e}{c} \mathbf{A} + \nabla \psi, \quad (3.7)$$

$$\frac{\partial \psi}{\partial t} = e\varphi - mc^2(\gamma - 1), \quad (3.8)$$

where γ is the relativistic factor. The laser pulse is short enough to neglect the ion motion, and we assume that the plasma will approach a quasi-stationary and homogeneous state where $\psi = 0$. We introduce the slowly varying, normalized amplitude, $a(r, x)$, of the vector potential $e\mathbf{A}/mc^2 = (1/2)a(r, x) \exp(i(k_L x - \omega t))(\mathbf{e}_y + i\mathbf{e}_z) + c.c$ where x is the direction of propagation and k_L is the vacuum wave number. Then the system of Eqs. (3.1-3.8) will take the following form:

$$2ik_L \frac{\partial a}{\partial x} + \nabla_{\perp}^2 a - \frac{k_L^2 n_0}{\gamma} na = 0, \quad (3.9)$$

$$\nabla_{\perp}^2(\phi) = k_L^2 n_0(n - 1), \quad (3.10)$$

$$\phi = \gamma - 1, \quad (3.11)$$

where $\gamma = \sqrt{1 + a^2}$ is the relativistic factor, $\phi = e\varphi/mc^2$, $n_0 = N_0/n_c$, $n = N/N_0$ and n_{cr} is the critical density.

3.3 Channelling

RSF at high laser powers leads to full evacuation of electrons by the ponderomotive force that is enhanced by the relativistic effect and results in the formation of plasma channels. This regime of the nonlinear laser pulse propagation has been of particular interest to the fast ignition scheme, particle acceleration and radiation generation, particularly as one can find the range of laser powers where such channels seem to exhibit a linear stability. In order to find an analytical, or almost an analytical solution describing the cylindrical plasma channel we assume the amplitude of the vector potential in the following form $a(r, x) = a(r) \exp(-i\kappa x)$ where κ is the propagation constant. Equations (3.9-3.11) can be now written as the set ordinary differential equations [15] in r :

$$\nabla_{\perp}^2 a(r) + \left(\kappa - \frac{n}{\gamma}\right) a(r) = 0, \quad (3.12)$$

$$\nabla_{\perp}^2 \phi = (n - 1), \quad (3.13)$$

$$\phi = \gamma - 1, \quad (3.14)$$

where $\nabla_{\perp}^2 = \frac{1}{r} \frac{d}{dr} \left(r \frac{d}{dr} \right)$ and spatial variables r, x are now normalized to $(k_L \sqrt{n_0})^{-1}$ and $(k_L n_0 / 2)^{-1}$ respectively (r and x denote from now on dimensionless variables). Equations (3.13), (3.14) give the plasma density $n = 1 + \nabla_{\perp}^2 \gamma$. Clearly in this model a strong ponderomotive force can produce full electron expulsion corresponding to $n = 0$. For even stronger ponderomotive force, which cannot be balanced by the electrostatic force due to charge separation, Eqns. (3.13), (3.14) can lead to nonphysical negative electron density. To deal with this problem Sun *et al.* [12] suggested a simple solution that amounts to setting $n = 0$ inside the cavitation region of the channel whenever $1 + \nabla_{\perp}^2 \gamma < 0$. As pointed out by Feit *et al.* [13] the straightforward application of this fix has resulted in the violation of the overall

charge neutrality. Only when the global structure of the solution is determined and the charge conservation is used in evaluation of the channel size [15] one could proceed with the solution to (3.12), (3.13), (3.14). Results of Ref. [15] for a single channel evacuation are reviewed below and later compared with PIC simulations.

Our first goal is to find the threshold power for channeling. Exceeding this power gives an electron cavitated region where $n(r \leq R) = 0$. The radius of the electron evacuated channel, R , can be calculated by considering the balance between the ponderomotive force and charge separation force. Assuming that R is the boundary position, we can write total charge conservation as:

$$\int_0^{+\infty} (1-n)rdr = \int_0^R rdr + \int_R^{+\infty} (1-n)rdr = 0, \quad (3.15)$$

where the plasma density $n = 1 + \nabla_{\perp}^2 \gamma$. Substituting n into Eq. (3.15) gives:

$$\left[\frac{a(r)a'(r)}{\sqrt{1+a(r)^2}} \right]_{r=R} = -\frac{1}{2}R. \quad (3.16)$$

To find a solution to Eq. (3.12), we need to know the values of $a(r)|_{r=R}$ and $a'(r)|_{r=R}$. For inside the channel, Eq. (3.12) will be:

$$\frac{1}{r} \frac{d}{dr} \left(r \frac{da(r)}{dr} \right) + \kappa a(r) = 0 \quad (3.17)$$

The solution to this equation is a Bessel function of order zero:

$$a_{ch}(r) = C J_0(\sqrt{\kappa}r), \quad (3.18)$$

C is the value of $a(r)|_{r=0}$. At $r = R$ continuity condition for $a(r)$ and $a'(r)$ gives:

$$a_{ch}(R) = C J_0(\sqrt{\kappa}R), \quad (3.19)$$

$$a'_{ch}(R) = -C \sqrt{\kappa} J_1(\sqrt{\kappa}R), \quad (3.20)$$

Substituting Eqs. (3.18-3.20) in Eq. (3.16) gives,

$$C^2 = \frac{R^2}{8\kappa J_1^2(\sqrt{\kappa}R)} \left(1 + \sqrt{1 + \frac{16\kappa J_1^2(\sqrt{\kappa}R)}{R^2 J_0^2(\sqrt{\kappa}R)}}\right). \quad (3.21)$$

Knowing C for a certain κ and fixed R , $a(R)$ and $a'(R)$ will be known.

To find solution in the plasma region $r > R$, we should combine Eq. (3.13) and Eq. (3.14) as,

$$n(r) = 1 + \frac{1}{r} \frac{d}{dr} \left(r \frac{d\gamma(r)}{dr} \right), \quad (3.22)$$

Substituting Eq. 3.22 into Eq. (3.12) gives:

$$a''(r) + \frac{1}{r} a'(r) - \frac{a(r)a'^2(r)}{(1+a^2(r))} + (\kappa(1+a^2(r)) - \sqrt{1+a^2(r)})a(r) = 0. \quad (3.23)$$

Equation (3.23) can be solved numerically using shooting method with R as the shooting parameter. Boundary conditions are: $a(r)|_{r=\infty} = 0$ and $a'(r)|_{r=\infty} = 0$. From the shooting method, we find that the complete evacuation does not happen if $\kappa > 0.88$. Therefore the threshold power for channeling ($\kappa_{th} = 0.88$) will be:

$$P_{th} = \int_0^\infty a_{\kappa_{th}}^2(r) r dr = 1.09 P_{cr} \quad (3.24)$$

In next Section, we will show the results of different PIC simulations and compare them with theoretical solutions.

3.4 Single Fully Evacuated Channels-PIC Simulation Results

We performed several 3D PIC simulations considering different parameters such as different background plasma densities and different laser spot sizes. We have used PIC codes Mandor [20] and SCPIC [21] in Cartesian geometry. In most of our runs

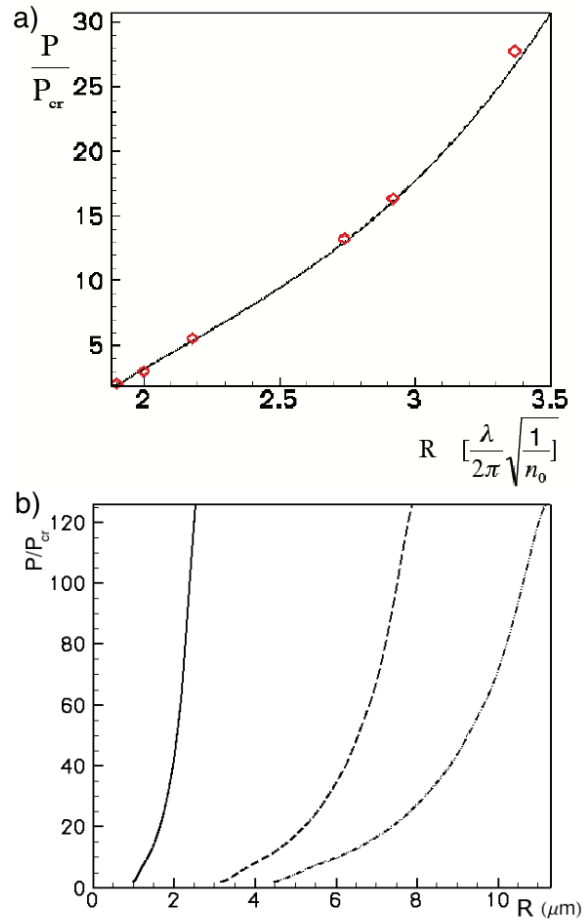


Figure 3.1 P/P_{cr} as a function of evacuated channel radius in units of $[k_L\sqrt{n_0}]^{-1}$ (calculated from theoretical model). Points show the simulation results (Fig.1-a). P/P_{cr} as a function of radius of evacuated channel in μm for plasma densities 0.1, 0.01, 0.005 n_{cr} (solid, dashed, dashed-dotted), calculated from theoretical model (Fig.1-b).

we have used laser pulses with a Gaussian profile, a rise time of 100 fs and a clamped amplitude afterwards. The pulse is focused $2 \mu m$ from the left boundary of the simulation box. The plasma is homogeneous with densities $(0.001 - 0.1)n_{cr}$, laser wavelength is $1 \mu m$. The spatial resolution in all simulations that were performed is $\Delta x = \Delta y = \Delta z = \lambda/15$ (λ is laser wavelength). Laser intensity is normalized to $I_0 = \frac{(m\omega c/e)^2 c}{4\pi}$. The laser pulse is circularly polarized. Light propagates along x direction. The dimension of simulation box is $X \times Y \times Z = (200 - 300)\mu m \times 40\mu m \times 40\mu m$. We have calculated the ion plasma period for different plasma densities in simulations and we limited the propagation distance accordingly except for higher plasma densities such as $0.1n_{cr}$ where ions are considered mobile.

We found that for low plasma densities, the incident Gaussian laser pulse with a power above threshold power for channeling reaches a quasi-stationary state which compares well with the solution from Sec. 3.3. A location of such solutions is illustrated in Fig. 3.1-a (solid curve). Different PIC simulations are shown by dots on the curve. We find that the radius of evacuated channel is to a very good approximation given by a scaling relation, $R(\mu m) = 0.245\lambda(\mu m)(P/P_{cr})^{(1/4.383)}\sqrt{n_0}$, where λ is the laser wavelength. Having the laser power and the initial plasma density, the radius of empty channel can be estimated. It can be seen from this scaling relation that the radius of the channel is smaller for higher plasma densities. Moreover, for the same plasma density, increasing the laser power leads to bigger channel radius. Dimensional graphs of P/P_{cr} as a function of channel radius R (μm) helps toward a better understanding of the problem. Figure 3.1-b shows the total power as a function of channel radius in μm for three plasma densities of 0.1, 0.01, 0.005 n_{cr} . We see that for the same total power we can get different channel radii, smaller channels for higher plasma densities.

Here we discuss the two sample simulations in more details. Figure (3.2) shows PIC simulation results where the homogeneous plasma density is $0.01n_{cr}$, the initial peak laser intensity is $2.5 \times 10^{19}W/cm^2$ and the initial full-width-half-maximum of the laser intensity is $6 \mu m$. Figure 3.2 shows the contour plots of laser intensity (a-c) and electron charge density (d-f) after propagating for $200 \mu m$. After the transient perturbations of the electron density and the laser intensity in front of the laser pulse which corresponds to the rising time of the pulse intensity, the simulation shows a stationary profile. We see in Fig. 3.2a-b that the laser pulse evacuates electrons, making a cylindrical uniform channel. Figure 3.2 c shows the front of the laser pulse. The density contour plot Fig. 3.2 d,e show a straight evacuated channel. Figure 3.2 f shows the interaction of front of the laser pulse with the plasma. The characteristic spiral shape in the electron density is due to the circular polarization of the laser pulse. We showed the calculated analytical and simulation result for this simulation in Fig. 3.3. The data from the simulation is taken from x-y plane at $x=90 \mu m$. We calculated the power of the laser, which is $P/P_{cr} = 5.0$ close to the expected value from theoretical solution $P/P_{cr} = 5.5$.

For the incident Gaussian pulse which has an initial power and a spot size different from the parameters of the stationary solutions in Fig. 3.1, the evolution towards these asymptotic states has involved focusing or defocusing of the laser pulse until it reaches the right width of the stable channel. Figures 3.4 show another simulation results where the homogeneous plasma density is $0.001n_{cr}$, the peak laser intensity is $5.0 \times 10^{20}W/cm^2$ and the initial full-width-half-maximum of the laser intensity is $6 \mu m$. Figures 3.4a,c show the contour plots of intensity profile of the laser and Figs. 3.4b,d the density profile of electrons. The ponderomotive force pushes the electrons away from regions with higher laser intensity making a completely evacuated channel.

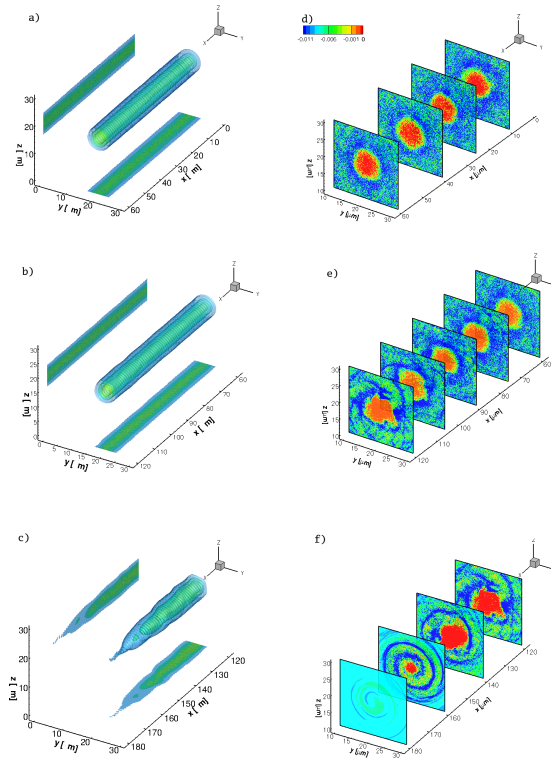


Figure 3.2 (Color online) Contours of laser intensity (a-c) and electron charge density (d-f) normalized to n_c .

The diameter of the evacuated channel is $\sim 30\mu\text{m}$. The laser power is $\sim 22 \times P_{cr}$. In this example, the initial laser spot size is smaller than the expected channel radius (Figs. 3.5), therefore the laser pulse first adjusts itself, broadens, increasing the spot size and then the channel becomes stable, (see Figs. 3.5). The solid curve in Fig. 3.5 shows the P/P_{ch} vs full channel width R for plasma density $0.001n_{cr}$. The star represents the input power and the initial full-width-half-maximum of the laser intensity. The circle represents the calculated power and channel width taken from transverse lineout in the simulation box.

We have first noticed a limitation on the extent and stability of relativistic fil-

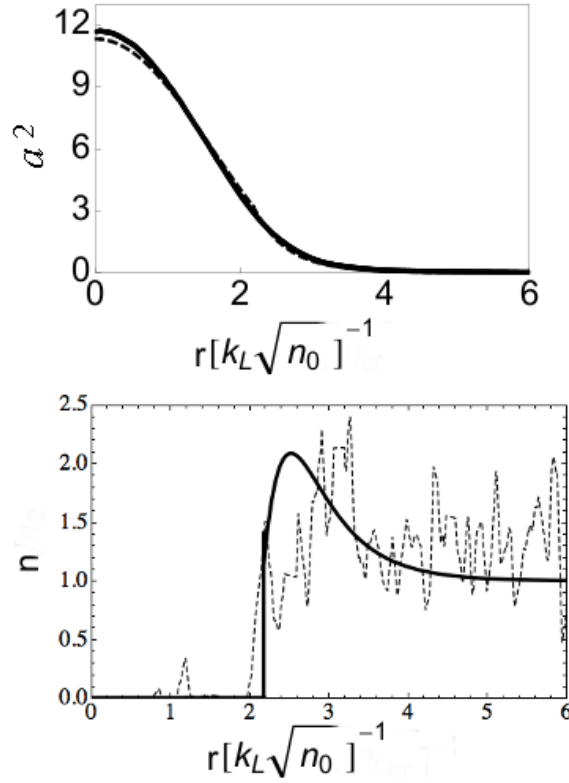


Figure 3.3 Comparison of theoretical solutions for laser intensity and electron density (solid curves) and simulation (dashed curves). Data taken from simulation in x-y plane at $x=90 \mu m$ ($t=633$ fs).

aments that otherwise satisfied conditions for a stationary single channel solutions when we increased plasma density in a few simulations. Taking as a background density $3.5 \times 10^{19} cm^{-3}$ and $P = 173P_{cr}$, results in an evacuated channel of a shorter length. The channel forms but after the front of the laser pulse propagated for $120 \mu m$, the evacuation is lost. Figure 3.6 shows the contour plots of laser intensity (a-c) and electron charge density (d-f) after propagating $200 \mu m$. We see in Fig. 3.6a-b that the laser pulse evacuates electrons, making a cylindrical uniform channel. The density contour plot Fig. 3.2 d,e show a straight evacuated channel. However the

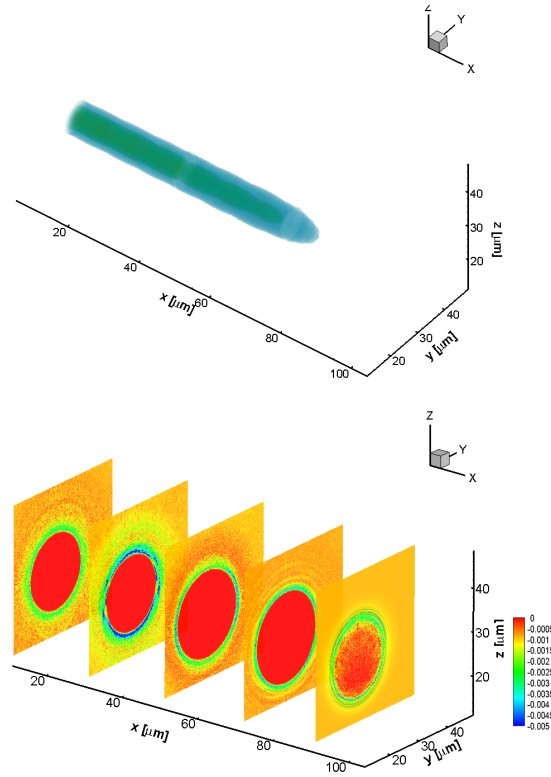


Figure 3.4 (Color online) Contours of laser intensity (a-c) and electron charge density (b-d) normalized to n_c .

complete evacuation is lost after $100\mu m$. We show the longitudinal momentum of electrons vs longitudinal direction in Fig. 3.7 for the last record in the simulation box. We can see that around $x=120\mu m$ and further on the heating is significant. As a result, the ponderomotive force is not strong enough to evacuate electrons. Here is where the destruction of the channel begins. The graph clearly shows the bunching of electrons at distances $\sim 12\mu m$. This bunching is the result of surface wave excitation on the channel edges which will be discussed in the next Section.

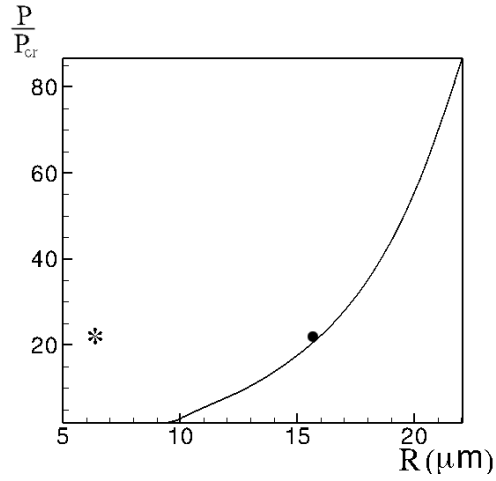


Figure 3.5 P/P_{cr} vs channel radius R in μm for plasma density $0.001n_{cr}$ (calculated from theoretical model). Star shows the initial FWHM of the laser intensity. Circle shows the calculated power and channel radius from simulation at $x = 90\mu m$ and $t=600$ fs.

3.5 Surface Wave Excitation

The RSF of the laser pulse above the threshold for channeling that corresponds to complete electron evacuation is not limited by scattering instabilities or plasma wakes. The two last processes require a finite electron density in the channel. However the steep density channel walls can support surface waves which modulate the density and can effectively accelerate electrons due to the longitudinal electric field component. The surface waves have been discussed in Ref. [30] in the weakly relativistic regime. It has been shown that for a given plasma density, the wavelength of the wake for sharp boundaries is $\lambda_s = \lambda_p \sqrt{1 + k_p R K_0(k_p R) / 2K_1(k_p R)}$ where λ_s is the surface wave wavelength and $k_p = \omega_p/c$ is the plasma wavenumber, R is the radius of the evacuated channel and K_0, K_1 are modified Bessel functions of the second kind. The more realistic case of a finite thickness boundary was studied by Shvets *et al.* [31]. As

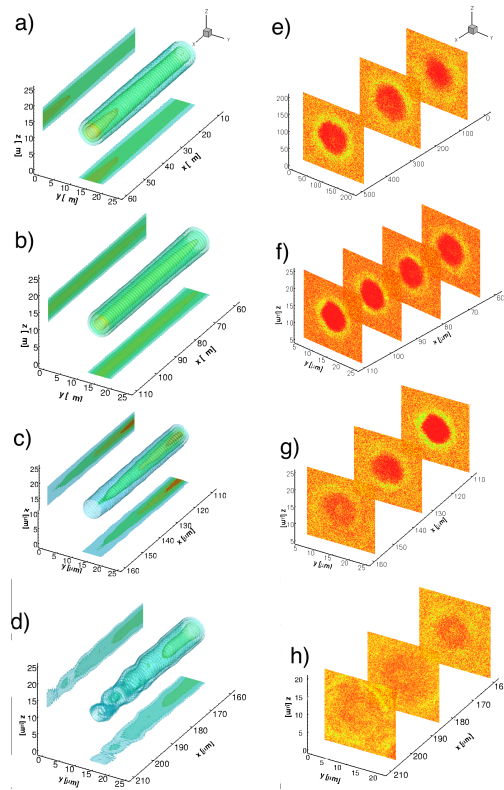


Figure 3.6 (Color online) Contour plots of laser intensity (a-c) and electron charge density (d-f) normalized to n_c .

discussed in Refs. [19,30] the surface waves are excited by the longitudinal component of the laser ponderomotive force. The shorter the rise time of the laser pulse and the steeper the intensity profile, the broader will be the spectrum of the surface waves that can be enhanced and driven to a nonlinear level. The longitudinal field of the excited waves can accelerate electrons and heat them, and this leads to the loss of the full evacuated channel. Here the simulation is done for the following parameters: peak laser intensity is $5 \times 10^{20} \text{ W/cm}^2$, FWHM of the laser intensity $8 \mu\text{m}$, plasma density is $0.001n_{cr}$ and pulse has a FWHM of 400 fs. The power of the laser is well above the threshold power for channeling. Therefore a fully evacuated channel is

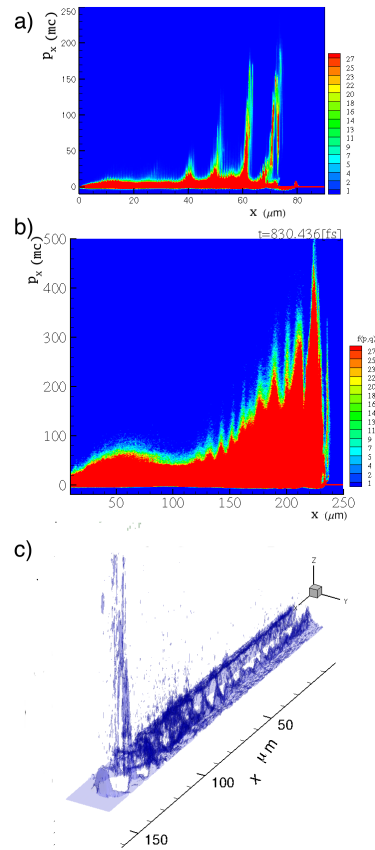


Figure 3.7 (Color online) a,b) Contour plot of longitudinal momentum of electrons normalized to mc after propagating for $80 \mu m$ and $240 \mu m$ vs longitudinal direction x in μm . c) Contour plot of longitudinal momentum of electrons normalized to mc in the x-y plane.

expected.

The laser pulse is linearly polarized along the z direction. Figure 3.8 shows the contour plots of the longitudinal field of the excited surface waves, the transverse field, the electron charge density and the laser intensity at $t=1070$ fs in the xy plane. The contour plots of the charge density clearly show the rippling of the channel at distances of $\lambda_s \sim 40 \mu m$ which is not far from $\lambda_p \sqrt{1 + k_p R K_0(k_p R) / 2K_1(k_p R)} = 40 \mu m$ where the plasma wavelength is $\lambda_p \sim 33 \mu m$ and the channel radius is $R \sim 15 \mu m$. The channel is fully evacuated. The contour plots of the longitudinal and transverse fields show that the fields oscillate at a surface wave wavelength and their magnitudes are maximum at the channel edges. Prediction of the longitudinal and transverse electric fields inside the empty channel are given as [30]:

$$E_x = A e^{i(k_x x - \omega t)} \quad (3.25)$$

$$E_r = -\frac{i k_x A r}{2} e^{i(k_x x - \omega t)} \quad (3.26)$$

where A is a constant. Figure 3.9 shows a transverse cut at $x=297 \mu m$ at $t=1070$ fs and shows the longitudinal and transverse fields of the surface waves at this position. The longitudinal field of the surface waves inside the channel is almost constant and it decays outside the channel. The transverse field of the surface wave is proportional to r , zero at the center of the channel and becomes maximum on the edges and then decays in the plasma outside the channel. This agrees with the fields taken from transverse cut in x - y plane in simulation (Fig. 3.9). The longitudinal field of the surface wave accelerates electrons, eventually the electrons become heated and full evacuation is lost. The excitation of the surface waves on the edges of evacuated channels is more enhanced when a finite laser pulse is used. However even for clamped laser pulses, this process can interfere with channeling. If the front part of the laser

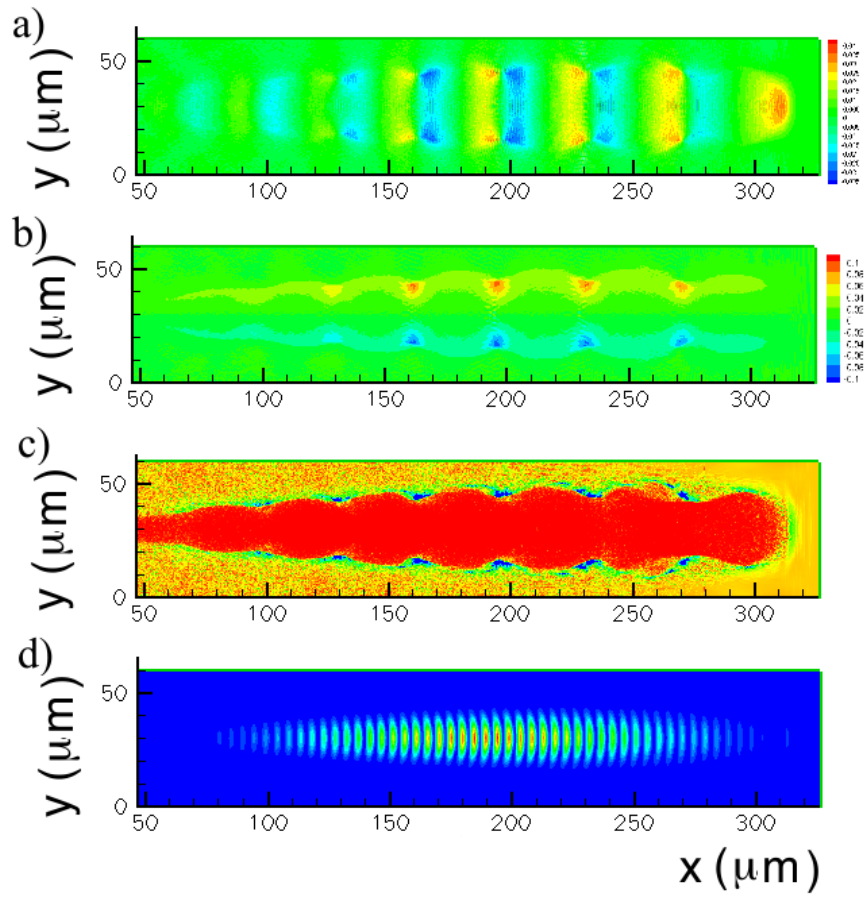


Figure 3.8 Contour plots of a) longitudinal electric field of the surface waves b) transverse field E_y c) electron charge densities and d) laser intensities in xy plane at $t=1070$ fs.

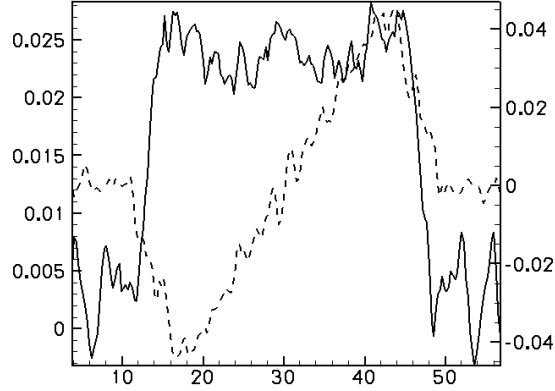


Figure 3.9 Longitudinal (solid) and transverse (dashed) electric fields at $x = 297\mu m$ at $t=1070$ fs in xy plane.

pulse is comparable with the wavelength of the surface waves, the surface waves can be excited on the edges of the evacuated channel starting from the front of the laser pulse and can heat the electrons and this will end the channeling process. It is important to note that the excitation of the surface waves is independent of its polarization. We used linearly polarized laser pulse to ease the visualization process in simulation.

3.6 Ring Structure

3.6.1 Ring Structure- Theoretical Review

Central depleted channels are not the only solutions to Eqs. (3.12-3.14). A central electron filament enclosed by an evacuated ring is another possible set of solutions to Eqs. (3.12-3.14) [15]. These structures can exist at higher laser powers. To solve the equations, the shooting parameter will be the on-axis value of the field and its first

derivative on axis will be zero because of symmetry. There is a freedom in choosing the boundary position (R_1 , Fig. 3.10). The only constraint is that the electron density can not be negative. The minimum power for this structure for specific κ is when the electron density at R_1 is zero. Having R_1 , we know the field amplitude and its first derivative at this point.

The solution for the depleted region (from R_1 to R_2) is:

$$a(r) = A_v J_0(\sqrt{\kappa}r) + B_v Y_0(\sqrt{\kappa}r), \quad (3.27)$$

where J_0 and Y_0 are zero order Bessel and Neumann functions respectively. Therefore the solution at the boundary is:

$$a(R_1) = A_v J_0(\sqrt{\kappa}R_1) + B_v Y_0(\sqrt{\kappa}R_1), \quad (3.28)$$

$$a'(R_1) = -A_v \sqrt{\kappa} J_1(\sqrt{\kappa}R_1) - B_v \sqrt{\kappa} Y_1(\sqrt{\kappa}R_1). \quad (3.29)$$

Integrating Poisson's equation:

$$\int_0^{+\infty} (1-n)rdr = \int_0^{R_1} (1-n)rdr + \int_{R_1}^{R_2} rdr + \int_{R_2}^{+\infty} (1-n)rdr = 0, \quad (3.30)$$

gives a relation between R_1 and R_2 :

$$g(R_1) - g(R_2) = \frac{1}{2}(R_2^2 - R_1^2), \quad (3.31)$$

where

$$g(r) = \frac{ra(r)a'(r)}{\sqrt{(1+a^2(r))}}. \quad (3.32)$$

Therefore R_2 can be calculated from above equations. Knowing R_2 , we can calculate $a(R_2)$ and $a'(R_2)$ and the solution for the semi-infinite plasma region can be found. The threshold power for exciting ring structure solution for fixed κ is when the density at the first boundary from central axis becomes zero. Figure 3.14 shows the minimum total power required for ring structure as a function of κ . The minimum power to excite these structures is $33P_{th}$.

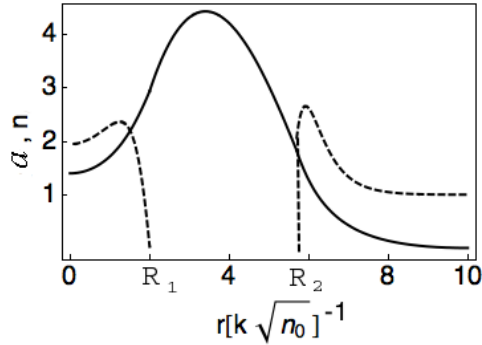


Figure 3.10 Schematic graph showing the ring structure solution. The solid curve is the amplitude of the laser and the dashed curve is the electron density calculated for $\kappa = 0.3$.

3.7 Ring Structure-Simulations

Ring structures were observed in 3D simulations. We always observed them coexisting with the main laser mode. We will present the results of a sample simulation with 3D PIC code SCPIC [21]. The input parameters are as follows: the initial homogeneous plasma density is $0.036n_{cr}$. Initial peak laser intensity is 10^{20} W/cm^2 and FWHM of the Gaussian laser pulse is $10 \mu\text{m}$ ($P \sim 230P_{th}$). The FWHM of the laser pulse is 250 fs and is focused $10 \mu\text{m}$ from the left boundary. Figure 3.11 shows the contour plots of time evolution of the laser intensity in the xy plane. In the beginning we see the formation of a single channel. Then the laser pulse starts splitting into two from the front after propagating for $100 \mu\text{m}$. The formation of uniform ring is illustrated in Fig. 3.12 which shows the laser intensity and electron charge density in y-z plane at $x = 95\mu\text{m}$. Figure 3.13 shows the comparison between theoretical and simulation results for ring structure ($\kappa = 0.3$). At later time, the ring structure goes back in the pulse. This is because the coexisting main mode has smaller κ , therefore has a larger

group velocity compared to the ring structure. Thus the ring structure is slower than the main mode and moves back in the pulse.

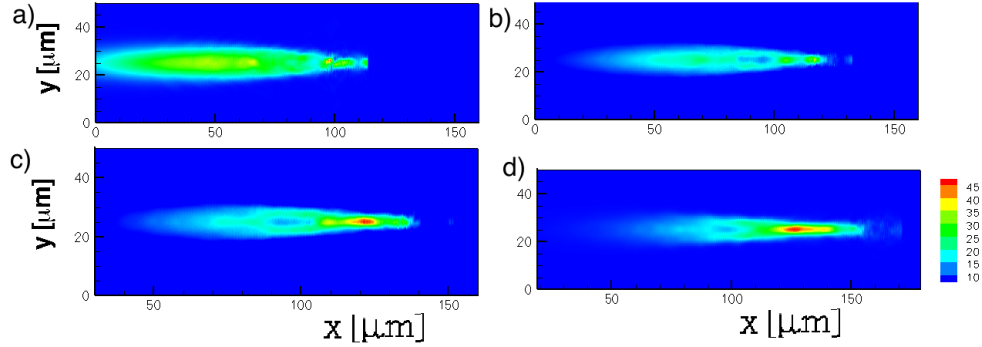


Figure 3.11 (Color online) Contour plots of laser intensity at different times.

3.8 Stability Analysis

3.8.1 Stability Analysis-Single Channel

We will examine the stability of theoretical solutions to Eqs. (3.12-3.14) by linear stability analysis. Within the stationary approximation of Sec3.2 we rewrite Eq. (3.12) as:

$$i\frac{\partial a}{\partial x} + \nabla_{\perp}^2 a - \frac{na}{\gamma} = 0, \quad (3.33)$$

where r is normalized to $[k_L\sqrt{n_0}]^{-1}$ and x is normalized to $[k_L n_0/2]^{-1}$. To investigate the stability of solutions to Eqs. (3.12-3.14), we assume an exponentially growing small perturbation as $a = a_0(r) + a_1(r) \exp(\delta x)$ where a_0 is the theoretical solution to Eqs. (3.12-3.14) and $a_1 = u + iv$, substituted into Eq. (3.33) upon linearization leads to:

$$\delta u = -L_0 v, \quad -\delta v = L_1 u. \quad (3.34)$$

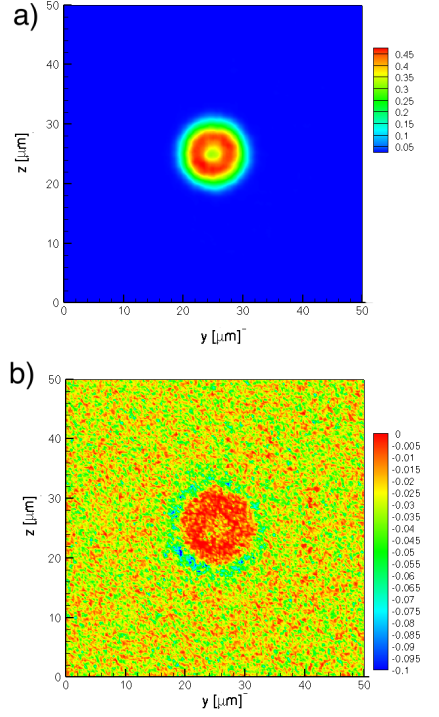


Figure 3.12 (Color online) Contour plots of laser intensity (a) and electron charge density (b) in y-z plane at $x=95 \mu m$ and $t=400$ fs.

The growth rate of small perturbation is determined by the above eigenvalue problem where the operators L_0 and L_1 are defined as:

$$L_0 = \kappa - \frac{1}{\gamma_0} + \frac{1}{r\gamma_0^2} \frac{d}{dr} + \frac{1}{\gamma_0^2} \frac{d^2}{dr^2} - \frac{a_0'^2}{\gamma_0^4}, \quad (3.35)$$

$$L_1 = L_0 + \frac{a_0^2}{\gamma_0^3} - \frac{2a_0 a_0'}{r\gamma_0^4} - \frac{a_0 a_0''}{\gamma_0^4} - \frac{2a_0 a_0'}{\gamma_0^4} + \frac{4a_0^2 a_0'^2}{\gamma_0^6}, \quad (3.36)$$

where $\gamma_0 = \sqrt{1 + a_0^2}$ and $L_0 a_0 = 0$. Therefore

$$L_0 L_1 u = -\delta^2 u. \quad (3.37)$$

It can be shown that a sufficient condition for the stability of solutions to Eqs. (3.12-3.14) against symmetric perturbation is $\frac{\partial P}{\partial \kappa} < 0$ [34]. With reference to Fig. 3.14

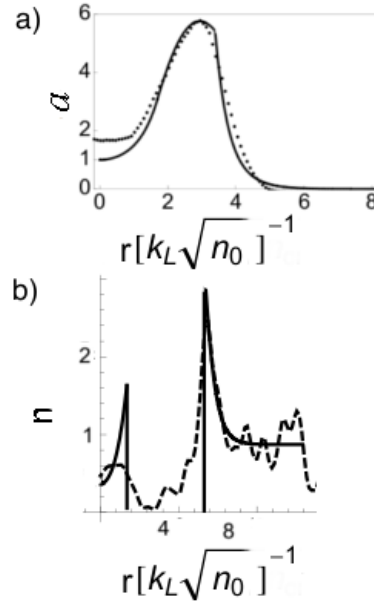


Figure 3.13 Amplitude of the laser (a) and electron density (b), solid curves are the theoretical solutions and dashed curves are taken from simulation in y - z plane at $x=95 \mu m$.

we see that both partially evacuated channel solution ($\kappa > 0.88$) and fully evacuated channel solution ($\kappa \leq 0.88$) are stable against symmetric perturbations [15].

3.8.2 Stability Analysis (symmetric perturbation)-Ring Structure

Figure 3.14 shows the total power as a function of propagation constant κ for ring structure solution when $n_{R1} = 0$ (dashed curve). As mentioned earlier the solutions with $n_{R1} = 0$ gives the least power required for ring structure formation [15]. For $\kappa \leq 0.5$, the stability condition $\frac{\partial P}{\partial \kappa} < 0$ holds. This means that the ring structure solution for $\kappa \leq 0.5$ is stable against symmetric perturbations. However for $\kappa > 0.5$,

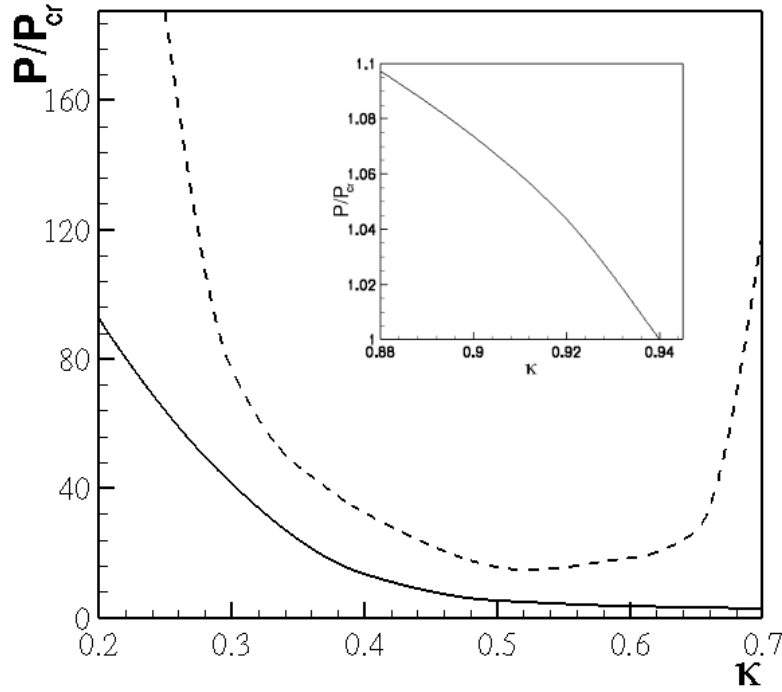


Figure 3.14 The solid curve shows the power as a function of κ for single channel solution. The dashed curve shows the minimum power required to obtain ring structure as a function of κ . The total power as a function of κ for partial evacuation is shown in the inset.

the stability condition is not satisfied $\frac{\partial P}{\partial \kappa} > 0$ [15]. Therefore ring structure solution with propagation constant $\kappa > 0.5$ is unstable against symmetric perturbation. We should mention that the above discussion is for a special case of $n_{R1} = 0$. For other possible cases where $n_{R1} \neq 0$, one has to plot the corresponding graph and examine the stability condition $\frac{\partial P}{\partial \kappa} < 0$.

3.8.3 Stability Analysis (asymmetric perturbation)-Ring Structure

In this Section we examine the stability of ring structure for asymmetric (azimuthal index=1,2,...) eigenfunctions. We will show that the break up of the ring structure can be due to a transverse instability. To investigate the stability of ring structure, we use approximate stability theory [35,36] where all quantities are the mean values averaged over annular ring (evacuated region). We assume azimuthally dependent perturbation as:

$$a = a_0 + \mu \cos(m\theta) \exp(\delta x), \quad (3.38)$$

where μ is a small constant and δ is the growth rate. The form chosen here ensures that the field is periodic in θ and it allows the modulation to develop around the ring. This means that we have azimuthal perturbation which as will be shown can break the azimuthal symmetry of the ring. Substituting Eq. (3.38) into Eq. (3.33) upon linearization leads to:

$$\delta^2 = \left(\kappa - \frac{m^2}{\bar{r}^2}\right) \left(\kappa - \frac{m^2}{\bar{r}^2 \gamma_0^2} - \frac{\bar{a}_0 \bar{a}_0''}{\gamma_0^4} + \frac{3\bar{a}_0 \bar{a}_0'^2}{\gamma_0^6} - \frac{\bar{a}_0 \bar{a}_0'}{\bar{r} \gamma_0^4}\right), \quad (3.39)$$

where $\bar{Q} = \int_{R_1}^{R_2} Q a_0^2 r dr / \int_{R_1}^{R_2} a_0^2 r dr$ with Q which denotes any of the quantities a_0, a_0', r, γ_0 . Figure 3.15 shows the growth rate of transverse instability as a function of $\kappa - 1$. Solid curve shows the growth rate of the transverse instability for $m = 1$ and dashed-curve for $m = 2$. It can be seen that $m = 1$ dominates over $m = 2$. The characteristic gain length ($1/\delta$) can be very long for lower plasma densities.

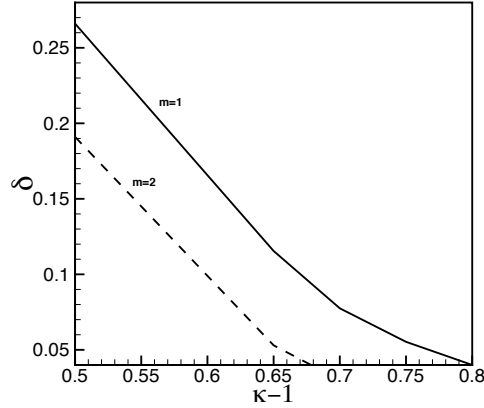


Figure 3.15 Growth rate of transverse instability δ as a function of $\kappa - 1$ for ring structure $m = 1, 2$.

3.9 Evolution of Laser Pulses at Higher Plasma Densities

Azimuthal perturbations due to the interaction of an intense laser pulse with a plasma can break up the symmetry of the laser pulse as addressed in previous Section. We observed the symmetry breaking of the laser pulse in simulations in higher plasma densities ($n_0 \geq 0.1$). We could not reach the stable channeling in simulations as predicted from analytical solutions for $n/n_{cr} \geq 0.1$. Azimuthal instability becomes more important in this regime because the gain length is smaller.

Figure 3.16 shows a simulation with following parameters: initial plasma density is $0.1n_{cr}$, the peak laser intensity is $4.7 \times 10^{19} \text{ W/cm}^2$ and the initial FWHM of the laser intensity is $5 \mu\text{m}$. This simulation was performed twice with both movable and stationary ions. Figure 3.16 shows the iso-surfaces of evolution of the laser pulse as it propagates through the plasma for $300 \mu\text{m}$. We see the formation of a ring structure

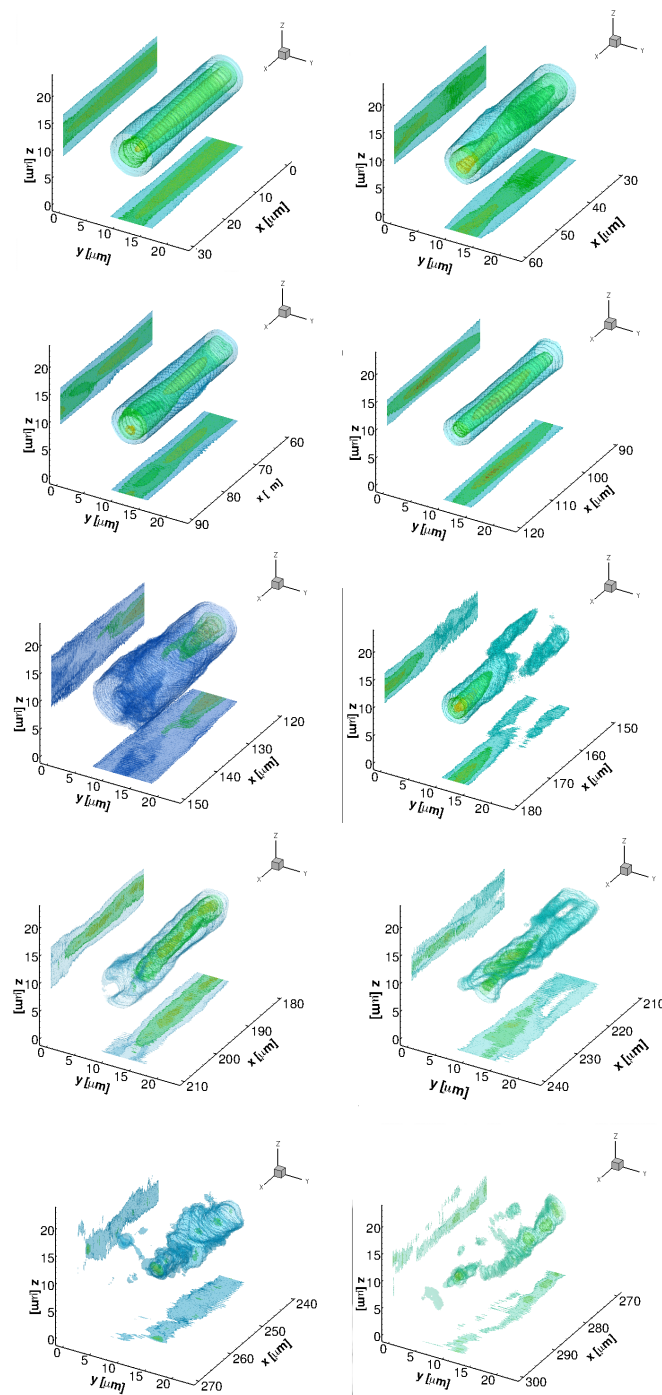


Figure 3.16 (Color online) Contour plots of laser intensity after propagating for $300 \mu\text{m}$.

after propagating for $x=17 \mu m$. Figure 3.18 shows a cut at $x=17 \mu m$ in y - z plane. The top panel, bright ring, shows the laser intensity and the lower panel shows the electron charge density. The plasma density follows the same pattern, central electron filament enclosed by a cavitated ring. This structure correspond to $\kappa = 0.4$. As the laser pulse propagates farther, the ring loses its symmetrical shape.

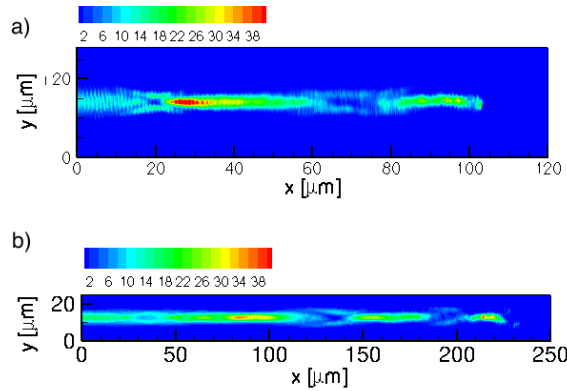


Figure 3.17 (Color online) Contour plots of laser intensity in x - y plane at $t=464$ and 943 fs.

Azimuthal perturbation breaks the symmetry of ring structure as it propagates through plasma (See 3.8.3). Figure 3.17 shows the contour plots of the laser intensity in x - y plane at $t=464$ and 943 fs. Figure 3.19 shows different cuts at different positions in the y - z plane at $x=21$, 44 and $70 \mu m$ at $t=580$ fs. Figure 3.19-a shows a ring structure at $x=21 \mu m$, central maximum at $x=44 \mu m$ and nonuniform ring at $x=70 \mu m$. The growth rate of the transverse instability for ring structure for this simulation ($\kappa = 0.4$) is 0.1 which corresponds to a gain length of $33 \mu m$ for these parameters.

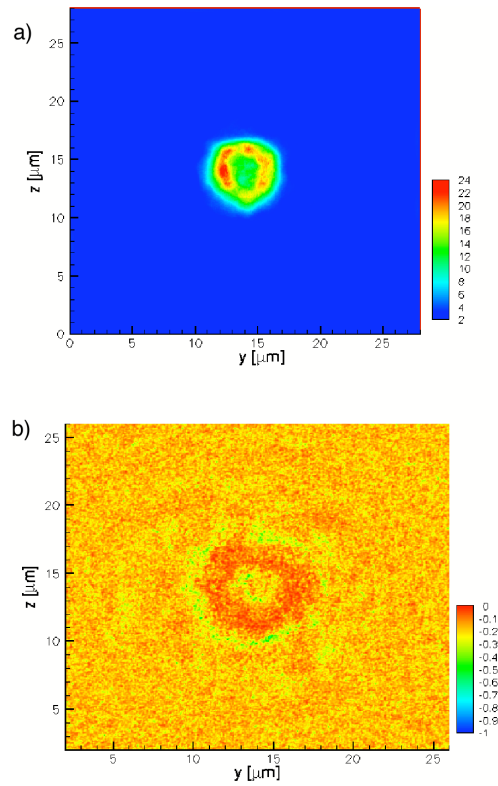


Figure 3.18 (Color online) Contour plots of laser intensity (a) and electron charge density (b) in yz plane at $x=17 \mu\text{m}$ and $t=133 \text{ fs}$.

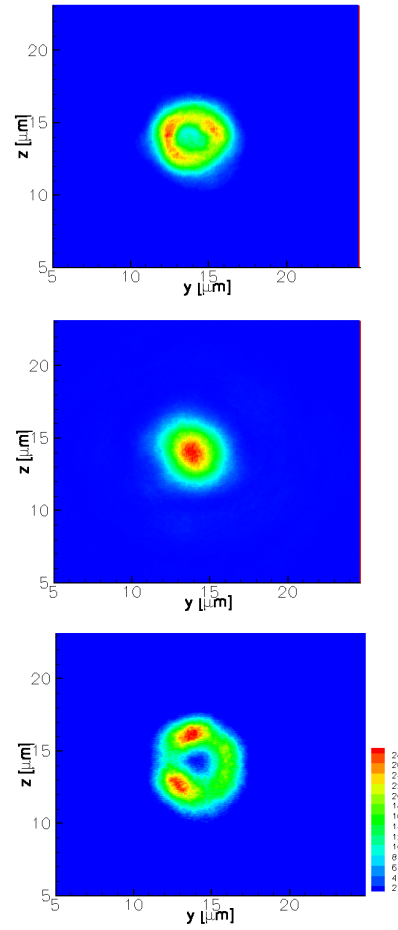


Figure 3.19 (Color online) contour plots of laser intensity showing in y - z plane, cuts at $x=21, 44$ and $70 \mu\text{m}$ at $t=580$ fs.

3.10 Conclusions

We have studied laser pulse channeling in underdense plasma by means of analytical theory and 3D PIC simulations. Numerous theoretical studies over the years [9, 12, 13, 16, 17] and in particular the Ref. [15] have provided the set of analytical results which are used together with 3D PIC simulations in constructing different scenarios of laser pulse channeling.

The most significant result of this paper is the demonstration of the single fully evacuated stationary channel solution can be reached an asymptotic state in PIC simulations. In the density range $0.001 < n_0 < 0.1$ and for a laser power above channeling power, $P_{th} \sim 1.1P_{cr}$, we were able to reproduce in PIC simulations the analytical curve from Fig. 3.1. It describes the location of stationary analytical solutions in terms of captured power vs channel radius. We showed that single channels are stable structures against symmetric perturbations. We have not observed stable channeling for plasma densities $\geq 0.1n_{cr}$.

The excitation of the surface waves on the edges of the fully evacuated channel was addressed. The amplitude of the excited surface waves grows as the laser propagates through the plasma and so does the energy of the electrons on the edges of the evacuated channel. Eventually the electrons will be heated and start filling the channel. It is important to note that the excitation of the surface waves can happen if the ascending part of the laser is comparable with the surface wave wavelength.

We also studied the formation of the ring structure in theory and simulations. An evacuated ring enclosed by an electron filament was observed in our 3D simulations. However they always coexist with the main laser mode. The threshold power for ring structure formation is when $P > 33P_{cr}$. Higher laser power is needed for ring

formation. These rings are stable against symmetric perturbations if $\kappa < 0.5$ (Fig. 3.15). Our studies on stability of the rings against asymmetric perturbations show that ring structure is not stable against azimuthal perturbations. The growth rate of the instability is shorter for higher densities and it is therefore more effective at higher densities. In fact, we presented an example (Fig. 3.17) for the density $0.1n_{cr}$ where the evacuated ring forms early in the simulation, however due to transverse instability the ring collapses and nonuniform rings form (Fig. 3.19).

Bibliography

- [1] M. Tabak, J. Hammer, M. E. Glinsky, W. L. Kruer, Scott C. Wilks, J. Woodworth, E. M. Campbell, M. D. Perry and R. J. Mason, *Phys. Plasmas* **1**, 1626 (1994).
- [2] S. P. Mangles, B. R. Walton, M. Tzoufras, Z. Najmudin, R. J. Clarke, A. E. Dangor, R. G. Evans, S. Fritzler, A. Gopal, C. Hernandez-Gomez, W. B. Mori, W. Rozmus, M. Tatarakis, A. G. Thomas, F. S. Tsung, M. S. Wei, and K. Krushelnick, *Phys. Rev. Lett* **94**, 245001 (2005)
- [3] Z. Najmudin, K. Krushelnick, M. Tatarakis, E. L. Clark, C. N. Danson, V. Malka, D. Neely, M. I. K. Santala, A. E. Dangor, *Phys. Plasmas* **10**, 438 (2003).
- [4] M. Borghesi, A. J. MacKinnon, L. Barringer, R. Gaillard, L. A. Gizzi, C. Meyer, O. Willi, A. Pukhov, and J. Meyer-ter-Vehn, *Phys. Rev. Lett.* **78**, 879 (1997).
- [5] J. Davis, G. M. Petrov, and A. L. Velikovich, *Phys. Plasmas* **12**, 123102 (2005).
- [6] A. Pukhov, Z.-M. Sheng, J. Meyer-ter-Vehn, *Phys. Plasmas* **6**, 2847 (1999).
- [7] E. Esarey, C. B. Schroeder, B. A. Shadwick, J. S. Wurtele, and W. P. Leemans, *Phys. Rev. Lett* **84**, 3081 (2000).

-
- [8] G. A. Askar'yan, Sov. Phys. JETP **15**, 168 (1962).
- [9] A. B. Borisov, J.W. Longworth, K. Boyer, and C. K. Rhodes, Proc. Natl. Acad. Sci. USA **95**, 7854 (1998); A.B. Borisov, O. B. Shiryaev, A. McPherson, K. Boyer and C. K. Rhodes, *Plasma Phys. Control. Fusion* **37**, 569 (1995)
- [10] K.-C. Tzeng and W. Mori Phys. Rev. Lett **81**, 104 (1998).
- [11] C. Max, J. Arons and A. B. Langdon, Phys. Rev. Lett **33**, 209 (1974).
- [12] Gou Zheng Sun, E. Ott, Y. C. Lee and P. Gudzar, Phys. Fluids **30**, 526 (1987).
- [13] M. D. Feit, A. M. Komashko, S. L. Musher, A. M. Rubenchik, and S. K. Turitsyn, Phys. Rev. E **57**, 7122 (1998).
- [14] F. Cattani, A. Kim, D. Anderson, and M. Lisak, Phys. Rev. E **64**, 016412 (2001)
- [15] A. Kim, M. Tushentsov, F. Cattani, D. Anderson, and M. Lisak, Phys. Rev. E **65**, 036416 (2002)
- [16] T. Kurki-Suonio, P. J. Morrison, and T. Tajima, Phys. Rev. A **40**, 32302 (1989)
- [17] X. L. Chen and R. N. Sudan, Phys. Fluids. B **5**, 1336 (1993)
- [18] G. Li, R. Yan, C. Ren, T.-L. Wang, J. Tonge, and W. B. Mori, Phys. Rev. Lett. **100**, 125002 (2008).
- [19] N. Naseri, S. G. Bochkarev, W. Rozmus, Phys. Plasmas. **17**, 033107 (2010)
- [20] D. Romanov, V. Yu. Bychenkov, W. Rozmus, C. E. Capjack and R. Fedosejevs, Phys. Rev. Lett **93**, 215004 (2004)

-
- [21] K. I. Popov, V. Yu. Bychenkov, W. Rozmus, R. D. Sydora, and S. S. Bulanov, Phys. Plasmas **16**, 053106 (2009).
- [22] L. M. Gorbunov, Sov. Phys. Usp. **16**, 217 (1973).
- [23] I. D. Kaganovich, G. Shvets, E. Stratsev, and R. C. Davidson, Phys. Plasmas **8**, 4180 (2001).
- [24] G. Shvets, and J. S. Wurtele, Phys. Rev. Lett **73**, 3540 (1994).
- [25] R. Y. Chiao, E. Garmire, and C. H. Townes, Phys. Rev. Lett. **13**, 479 (1964).
- [26] P. Sprangle, Cha-Mei. Tang, E. Esarey, IEEE Trans. on Plasma Sci. **15**, 145 (1987).
- [27] V.I. Berezhiani, S.M. Mahajan, Z. Yoshida, and M. Pekker, Phys. Rev. **E65**, 046415 (2002).
- [28] W. J. Firth, D. V. Skryabin, Phys. Rev. Lett. **79**, 2450 (1997)
- [29] E. Esarey, J. Krall and P. Sprangle, Phys. Rev. Lett. **72**, 2887 (1994).
- [30] T. C. Chiou, T. Katsouleas, C. Decker, W. B. Mori, J. S. Wurtele, G. Shvets and J. J. Su, Phys. Plasmas **2**, 310 (1995)
- [31] G. Shvets, J. S. Wurtele, T. C. Chiou, T. Katsouleas, IEEE Trans. Plasma. Sci **24**, 351 (1996)
- [32] N.M. Naumova, J. Koga, K. Nakajima, T. Tajima, T. Zh. Esirkepov, S. V. Bulanov, and F. Pegoraro, Phys. Plasmas **8**, 4149 (2001).

-
- [33] B. J. Duda and W. B. Mori, Phys. Rev. E **61**, 1925 (2000); B. J. Duda, R. G. Hemker, K. C. Tzeng, and W. B. Mori, Phys. Rev. Lett. **83**, 1978 (1999)
- [34] N. G. Vakhitov and A. A. Kolokolov, Sov. RadioPhys. **16**, 783 (1973)
- [35] J. Atai, Y. Chen, J. M. Soto-Crespo, Phys. Rev. A **49**, R3170 (1994)
- [36] J. M. Soto-Crespo, D. R. Heatley, E. M. Wright and N. N. Akhmediev, Phys. Rev. A **44**, 636 (1991)

Chapter 4

Axial Magnetic Field Generation in Interaction of Intense Circularly Polarized Laser with Underdense Plasma

An inverse Faraday effect (IFE) as proposed by L. P. Pitaevskii [1] in 1960 corresponds to an axial magnetic field generation by circularly polarized electromagnetic waves in dielectrics. With the invention of a laser in the same year, 1960, and in particular with the introduction of high intensity short pulse lasers in the last two decades, IFE has now been studied experimentally in laser produced plasmas [2–5] and by means of numerical simulations and theoretical analysis [6–15].

In addition to IFE, several other mechanisms of the magnetic field generation

A version of this Chapter has been published. N. Naseri, V. Yu. Bychenkov and W. Rozmus, 2010. *Physics of Plasmas*. 17: 083109-(1-10).

during interactions of circularly polarized laser pulses with underdense plasmas have been proposed during the last two decades [16–19].

For example, M. G. Haines [16] has found that during the absorption of a short circularly polarized laser pulse, a torque is delivered to electrons. This results in the generation of an opposing torque due to an induced azimuthal solenoidal electric field. The induced electric field leads to the generation of an axial magnetic field. The axial magnetic field is inversely proportional to the electron density, $\approx 1/n$, and it is proportional to the laser light absorption coefficient, which is also a function of density [16].

In a different study, I. Yu. Kostyukov *et al.* [17] have demonstrated how the absorbed angular momentum of the laser pulse is transferred to the electron rotational motion resulting in the generation of an axial magnetic field. The laser light and the electromagnetic wave angular momentum are absorbed by electrons executing betatron oscillations in the ion channel formed by the high intensity pulse.

A kinetic model for the generation of a quasi-static magnetic field in the interaction of circularly polarized laser pulses with a plasma was developed by Yu. M. Aliev *et al.* [18] based on the Vlasov equation. This theory applies to hot plasmas where electron thermal velocity is much higher than typical phase velocity of the generated magnetic field. The model was later extended to the case of a relativistic two electron temperature plasma [19].

The aforementioned physical processes lead to diverse equations for the magnetic field generation. They display different scaling and dependence on plasma parameters and are also distinct from the theoretical description of the IFE. Even the papers that have been published specifically on the IFE [6–15] contain important differences between expressions describing an axial magnetic field generation. The phenomeno-

logical approach introduces the magnetization per unit volume \mathbf{M} given by

$$\mathbf{M} = \frac{e^3 n E_0^2}{2cm^2\omega^3} \hat{\mathbf{e}}_x \quad (4.1)$$

by adding single particle magnetic dipole moments $e\langle\mathbf{r}_0 \times \mathbf{v}_E\rangle/2c$ for all electrons, where n is the electron density, e and m are the electron charge and mass, E_0 is the amplitude of the electric field of the laser beam with frequency ω propagating in x-direction, and c is the speed of light. The Eq. (4.1) leads to the widely used expression for the axial magnetic field [1]

$$B = \frac{a^2}{2} \frac{n}{n_c} B_0, \quad (4.2)$$

that is usually identified with the standard IFE result for the magnetic field. Here $a = eE_0/mc\omega$, $B_0 = mc\omega/e$, and n_c is the critical plasma density. A source for this magnetic field is the magnetization current $\nabla \times \mathbf{M}$, with \mathbf{M} defined by Eq. (4.1), as it was shown in the earliest works on IFE [2, 6]. In Ref. [7] it was demonstrated that Eq. (4.2) follows also from the collisional electron hydrodynamics of a plasma in the nonrelativistic laser field. Given that $n_c \propto m$ and the relativistic laser field increases a mass of an electron, i.e. $m \rightarrow \gamma m$, the relativistic generalization of Eq. (4.2) reads [9]

$$B = \frac{a^2}{2} \frac{n}{\gamma^2 n_c} B_0, \quad (4.3)$$

after taking into account all relativistic mass factors,

$$\gamma = \sqrt{1 + a^2} \quad (4.4)$$

References [8, 10–15] have developed theories of the magnetic field generation based on the collisionless electron fluid description and have improved on the simple phenomenological approach of Refs. [1, 2, 6]. Whereas the theories of Refs. [8, 10, 12–14]

have shown similar results, the equations for the IFE magnetic field in Refs. [11, 15] are different from each other and from results of Refs. [8, 10, 12–14].

Thus, different studies that have been performed since 1990 [8, 10–17] have demonstrated that even without including kinetic effects (as in Refs. [18–20]) theoretical models for the magnetic field generation by a circularly polarized laser beam do not agree with Eq. (4.2). These studies also differ between themselves [8, 10–17] as far as the expressions for the magnetic field are concerned. Clearly, there is a need for 3D numerical simulations, that may clarify existing discrepancies between different theories and could help to identify a leading mechanism of the magnetic field generation. Such simulations have been recently performed in Ref. [15]. However, because no comparisons were given in Ref. [15] with analytical results no progress has been achieved in terms of finding the leading mechanism or the proper expression describing the B-field generation by IFE. We will present below the results of 3D PIC simulations and provide comparisons with theoretical results. We will focus on the range of parameters that lead to laser pulse channeling which is accompanied by the formation of strongly inhomogeneous electron density and laser intensity profiles. Our results that have been achieved for relatively long laser pulses without wakefield generation will also contribute to the description of relativistic self-focusing and laser plasma channeling [21–25].

We have demonstrated that the quasi-static magnetic field generation is due to IFE in inhomogeneous plasma and that the results of analytical theories [8, 12–14] are well reproduced by 3D PIC simulations for conditions of a laser plasma channel formation. The outline of the paper is as follows. In Sec. 4.1, we describe the study of typical radial distributions of magnetic fields in plasma channels due to the IFE using a theory derived in Refs. [12–14]. We show how the radial profiles of the electron

density and laser intensity affect the magnitude and spatial distribution of the axial magnetic field. In Sec. 4.2 and 4.3, using distributions of the laser intensity and density from our 3D simulations we compare quasi-static magnetic field calculations from the theory with the fields taken directly from the 3D PIC simulation. The distributions of quasi-static magnetic fields are found for several typical cases of PIC simulations relevant to characteristic features of self-channeling (Sec. 4.2.1 and 4.2.2) and cavitation (Sec. 4.2.3). In Sec. 4.2.4, we show that the magnetic field changes in time following adiabatically the evolution of the radial profiles of the laser intensity and of the density channel. The last Section, Sec. 4.3, contains a discussion and summary.

4.1 A Model of the IFE

It has already been shown [8] that a source of the quasi-static magnetic field due to IFE is a nonlinear current $\mathbf{j}_{NL} = e \langle \tilde{n}_e \tilde{\mathbf{v}}_e \rangle$, where the angular brackets denote an average over the laser period and \tilde{n}_e , $\tilde{\mathbf{v}}_e$ are the oscillatory density and the oscillatory velocity of electrons, respectively. The vector-potential in the plasma can be written as a sum of low and high frequency parts:

$$\mathbf{A}(\mathbf{r}, t) = \langle \mathbf{A}(\mathbf{r}, t) \rangle + \text{Re}\{A_L(\mathbf{r}, t)(\mathbf{e}_y + i\lambda\mathbf{e}_z) \exp[-i\omega(t - x/c)]\} \quad (4.5)$$

where x is the propagation direction of the laser beam of the amplitude A_L , and $\lambda = \pm 1$ refers to the left-hand and right-hand circularly polarized laser light. We will consider a well underdense plasma, $n \ll n_c$. An expression for the azimuthal current density excited by a laser pulse in a plasma in the cylindrical geometry is

given by [8, 10, 14]:

$$\langle \mathbf{j}_{NL} \rangle = \frac{e^3 A_L^2 \lambda}{2m^2 c^2 \omega \gamma} \frac{d n}{dr} \frac{1}{\gamma} \mathbf{e}_\theta, \quad (4.6)$$

where the relativistic factor, γ , is given by Eq. (4.4) and \mathbf{e}_θ is the unit vector in the azimuthal direction. It can be seen from Eq. (4.6) that the nonlinear current density is zero for a linearly polarized laser pulse ($\lambda = 0$). The equation describing the quasi-static axial magnetic field due to inverse Faraday effect can be written as [10, 14, 18]:

$$\frac{1}{r} \frac{d}{dr} \left(\frac{r\gamma}{n} \frac{d}{dr} B_x \right) - B_x = -\frac{\lambda}{2r} \frac{d}{dr} \left(\frac{ra^2}{n} \frac{d n}{dr} \frac{1}{\gamma} \right), \quad (4.7)$$

where the magnetic field is normalized to B_0 , the radial coordinate is normalized to $c/\omega = k_0^{-1}$ and the plasma density is normalized to n_c .

Equation (4.7) shows that the magnetic field depends on the spatial distribution of plasma density, n and laser intensity, a^2 , across a channel. According to Eq. (4.7) the magnetic field cannot be generated in a homogeneous plasma. In order to solve Eq. (4.7) one needs to know the spatial profile of the electron density and laser intensity. We consider first two limiting cases: a wide channel such as $k_p r_0 \gg \sqrt{\gamma}$ and a narrow channel with $k_p r_0 \ll \sqrt{\gamma}$. Here r_0 is the radius of the trapped laser beam and $1/k_p = c/\omega_{pe}$ is the plasma skin length, where ω_{pe} is the electron plasma frequency and k_0 is the laser wavenumber. For wide channels, the first term on the left-hand side of Eq. (4.7) is small and therefore the radial profile of the quasi-static magnetic field can be written as:

$$B_x = \frac{\lambda}{2r} \frac{d}{dr} \left(\frac{ra^2}{n} \frac{d n}{dr} \frac{1}{\gamma} \right). \quad (4.8)$$

This is the same expression as Eq. (4.6) in Frolov *et. al* [14]. For narrow plasma channels, the second term on the left hand side of Eq. (4.7) is negligibly small and

one gets:

$$B_x = \int_r^\infty dr \frac{\lambda a^2}{2} \frac{d n}{\gamma dr \gamma}. \quad (4.9)$$

One obtains simple scaling expressions for the magnetic field in a channel for the strongly relativistic case, $\gamma \gg 1$ from Eqs. (4.8) and (4.9): $B/n \sim (\sqrt{\gamma}/k_p r_0)^2$ for $k_p r_0/\sqrt{\gamma} > 1$ and $B/n \sim 1$ for $k_p r_0/\sqrt{\gamma} < 1$. This shows that a plasma channel of a few micron width and background density 0.01 - 0.1 n_{cr} may produce magnetic fields of tens of MG.

Note that the theoretical model based on Eqs. (4.6,4.7) is valid for laser pulses that are longer than the characteristic electron response time, i.e. for $\tau \gg 1/\omega_{pe}$, where τ is the laser pulse duration or its rise time for the case of pulses with clamped intensity that we will often use in simulations. In the opposite limit of very short laser pulses all other components of the magnetic field in addition to B_x are also important. We have also neglected electron collision effects. This is correct for the small electron-ion collision frequency, $\nu_{ei} \gg 1/\tau_B$ where τ_B is the characteristic time scale of the magnetic field variation. The time τ_B is determined either by the laser pulse duration or by the electron plasma response, $\tau_B = \max(\tau, 1/\omega_{pe})$. Finally, we have also neglected electron kinetic effects [18]. For this approximation the radial scale length of the magnetic field, L_B , should satisfy $L_B \gg v\tau_B$ where v is characteristic velocity of bulk electrons; correspondingly $L_B = \max(r_0, \sqrt{\gamma}/k_p)$.

Figure 4.1 illustrates the radial distributions of a quasi-static magnetic field for moderately relativistic case, Fig. 4.1a, and strongly relativistic case, Fig. 4.1b, laser intensities with a Gaussian radial profile $\propto \exp(-r^2/r_0^2)$ and the plasma channel density distribution $n_0/(9e^{-r^2/r_0^2} + 1)$. Solid curves in Figs. 4.1 are obtained from the numerical solution of Eq. (4.7) and dashed curves show the limiting cases of wide

($k_p r_0 = 14.7$) and narrow ($k_p r_0 = 0.9$) plasma channels given by expressions Eq. (4.8) and Eq. (4.9), correspondingly. The magnitude of the magnetic field increases with the parameter $k_p r_0$ which plays an important role in the magnetic field generation. The magnetic field has a maximum on the channel axis and decreases in a radial direction away from the center changing its sign at some radius. The sign change of the magnetic field in Fig. 4.1 corresponds to the change in the direction of the magnetic field vector \mathbf{B} at the channel edge. The two azimuthal current layers in Eq. (4.6) are responsible for this field configuration. The currents flow in the opposite directions [14] due to the change in a sign of the radial derivative in Eq. (4.6). This effect is reproduced by the approximate solution (4.8) (cf. Fig. 4.1a) however it is lost in Eq. (4.9) for the limiting case of a narrow channel (cf. Fig. 4.1b). In general, the approximate solutions (4.8) and (4.9) describe well the magnetic field profile for large and small $k_p r_0 / \sqrt{\gamma}$, respectively. Figure 4.2 demonstrates a comparison of the solution to Eq. (4.7) (solid curve) with the magnetic field profiles from Refs. [2, 6, 9] (dotted curve) and from Ref. [11] (dashed curve) for the same plasma and laser parameters. An important difference between these profiles corresponds to the single direction (dotted) and to a change in the direction (solid and dashed curves) of the generated magnetic field. The magnetic field distribution derived by M. G. Haines [16] scales as $\propto \alpha(n)a^2/n$, where $\alpha(n)$ is an absorption coefficient. Also, the B-field profile from [16] does not display a two directional structure as given by Eq. (4.7), i.e. topologically it is similar to expressions from Refs. [2, 6, 9].

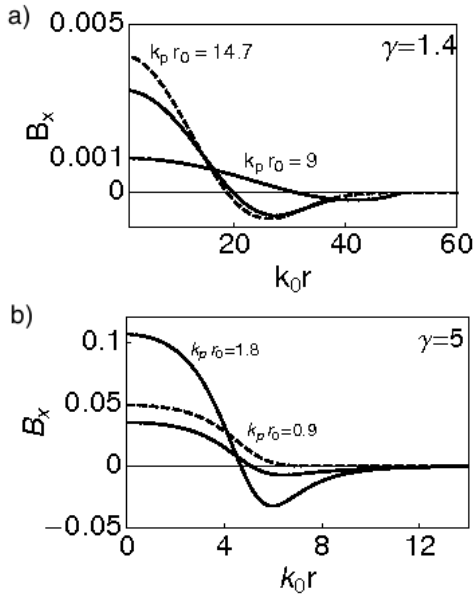


Figure 4.1 The radial distributions of axial magnetic field induced by interaction of circularly polarized laser pulse with plasma. Figure (a) shows the solutions obtained from Eq. (4.7) for wide channels ($k_p r_0 = 14.7$ and $k_p r_0 = 9$) and (b) shows the same solution for narrow channels ($k_p r_0 = 1.8$ and $k_p r_0 = 0.9$). The dashed curves in (a) and (b) correspond to expressions given by Eqs. (4.8) and (4.9) for $k_p r_0 = 14.7$ and $k_p r_0 = 0.9$, respectively.

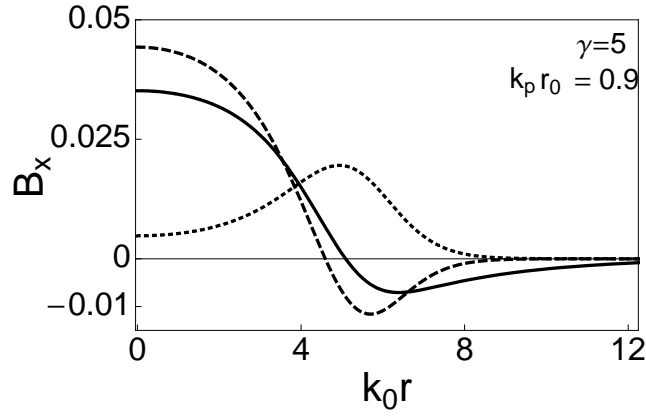


Figure 4.2 Comparison of the solution to Eq. (4.7) (solid curve) with B-field profiles from Refs. [2, 6, 9] (dotted curve) and results from Ref. [11] (dashed curve).

4.2 3D Simulation Results

In order to study magnetic field generation in a realistic geometry of the relativistic self-focusing and laser pulse channeling we have performed 3D simulations using our PIC code Mandor [26]. The laser light propagates in the x-direction and is circularly polarized, the laser wavelength is $1 \mu\text{m}$. We have used 8 particle per cell for all simulations. The spatial resolution in all simulations is $\Delta x = \Delta y = \Delta z = \lambda/15$ (λ is laser wavelength). The laser pulse has a rise time of 100 fs and a clamped constant amplitude afterwards and it is focused at $2 \mu\text{m}$ from the left boundary of the simulation box.

As in the discussion of theoretical results above, the laser intensity is given by a^2 . In order to find the distribution of a quasi-static axial magnetic field, we have located probes along the transverse direction, y , in the simulation box. The probes have collected data on the time evolution of the magnetic field that is subsequently

averaged over the laser wave period. This gives the distribution of an axial quasi-static magnetic field at the given cross section. The probes were distributed uniformly $1/3 \mu m$ apart from one another. For comparison with the theory of IFE we have solved Eq. (4.7) numerically using the radial distributions of the laser pulse intensity and the plasma density profile in a channel given by the results of our PIC simulations. To check the characteristic feature of the IFE that clearly identifies this mechanism as the source of the magnetic field, mainly the change in the magnetic field direction after reversal from clockwise to counter-clockwise directions of the light polarization, we have performed two simulations with different circular polarization of the laser beam. Figure 4.3 shows the averaged quasi-static magnetic field. The circles show the quasi-static magnetic field for the counter-clockwise polarization of the laser light and triangles show the B-field for the clockwise polarization of the laser light. Figure 4.3 agrees with the Eq. (4.7) which changes the sign when the polarization changes from $\lambda = +1$ to $\lambda = -1$ in accordance with the IFE. We have checked this feature for different laser-plasma parameters confirming that the IFE is the main source of a quasi static axial B-field in our simulations. Below we study the magnetic field profiles for three typical cases of relativistic self-focusing and laser light self-channeling: (1) self-focusing with a single channel formation, (2) self-focusing leading to a ring structure formation, and (3) the regime of a complete electron expulsion from the channel.

4.2.1 A Single Channel Self-Focusing

We will discuss the results of two simulations corresponding to the examples where only one central density channel is formed and the channel is not fully evacuated. The initial parameters for the first run are as follows: the maximum of the input

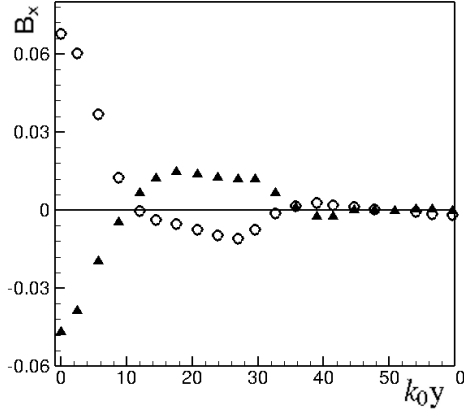


Figure 4.3 Quasi-static magnetic field calculated from probes located at $x = 85 \mu m$ in simulation box. Initial peak laser intensity is $4.7 \times 10^{19} W/cm^2$. The initial FWHM of the laser intensity is $5 \mu m$ and the background plasma density is $0.1n_{cr}$. Circles and triangles correspond to $\lambda = \pm 1$.

laser intensity (indicated by the subscript 00) is $1 \times 10^{20} W/cm^2$ that corresponds to $a_{00} \simeq 6$. The relativistic self-focusing has increased the laser intensity in the channel to $a \simeq 12$. The initial transverse FWHM of the laser intensity of the input Gaussian beam is $5 \mu m$ in the best focus position. The quasi-stationary nonlinear channel in a plasma has a radius of $2.5 \mu m$. Ions are considered as immobile in the simulation. The background plasma density is $0.36n_{cr}$.

Figure 4.4 shows the contour plots of the laser intensity and the electron charge density at $x=32 \mu m$ in the y - z plane. The contour plots show the formation of a single cylindrical channel. The minimum electron density in the channel is $0.2n_{cr}$ at the beam center. The laser beam is self-focused and the peak laser intensity increases four times in a channel. The dashed curves in Fig. 4.5 show the transverse (along the y direction) spatial distributions of the laser intensity and of the electron density in

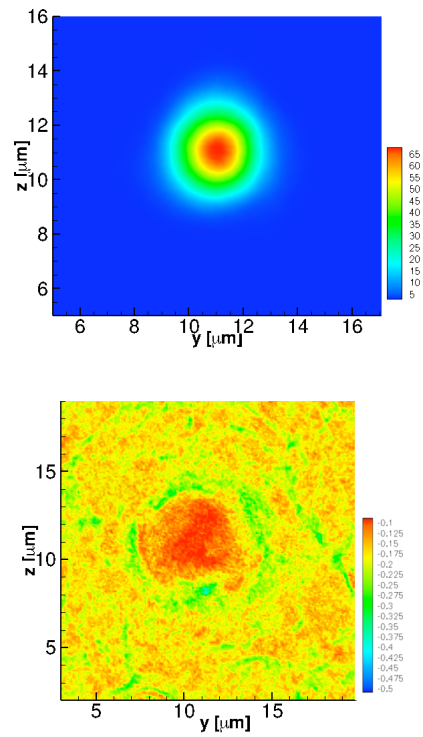


Figure 4.4 (Color online) Contour plots of a) laser intensity and b) electron charge density at $x=32 \mu\text{m}$ for a single channel.

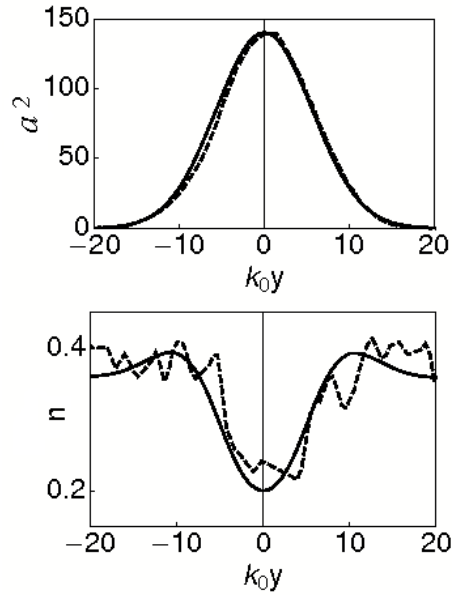


Figure 4.5 Distributions of laser beam intensity and electron density across the propagation direction at $x=32 \mu m$ (the dashed curves) for a single channel self-focusing. Solid curves show the analytical functions used for fitting and later in the numerical solutions of Eq. (4.7).

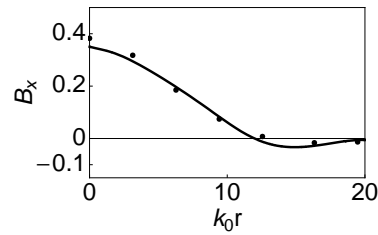


Figure 4.6 Comparison of the quasi-static magnetic field profiles for a single channel obtained from PIC simulation (dots) and by the analytical IFE theory (solid curve) using the intensity and density profiles shown in Figs. 4.4 and 4.5.

the simulation box at $x = 32\mu m$. We have estimated $k_p r_0 / \sqrt{\gamma} \sim 2.3$ within a channel. The solid curves in Fig. 4.5 show analytical functions representing the best fits of $a(r)$ and $n(r)$. These analytical functions have been used in the numerical solutions of Eq. (4.7). Figure 4.6 shows radial distribution of the axial magnetic field (solid curve) which is the solution of Eq. (4.7) while dots show the quasi-static magnetic field from PIC simulation. The maximum magnetic field in the center ($y=0$) is 35 MG.

We have significantly increased the laser input intensity up to $1 \times 10^{22} W/cm^2$ or $a_{00} \simeq 60$ in the second numerical example. The initial FWHM of the laser intensity is the same as before $5 \mu m$. The background plasma density is also the same at $0.36n_{cr}$. Because of the relatively high background plasma density the relativistic self-focusing does not lead to a fully evacuated channel. Electrons would be fully expelled from the channel at this high input laser power for smaller background plasma densities, $n < 0.1n_{cr}$ (cf. e.g. Ref. [25,27]). However, such a nonlinear filament in Figs. 4.7,4.8, where electrons are not fully evacuated, is not stable and will eventually develop transverse modulations or hosing type instabilities on the long time scale. Figure 4.7 shows the contour plots of the laser intensity and electron charge density in y-z plane at $x=51 \mu m$. As before, one central density channel is formed.

The laser intensity in a channel has been increased due to self-focusing by a factor 1.6 from its initial maximum intensity or $a \simeq 1.3a_{00}$ and the characteristic channel radius has been reduced to $r_0 \sim 4\mu m$ and FWHM of the laser intensity has become $3.9 \mu m$. The dashed curves in Fig. 4.8 show the transverse (along the y direction) spatial distributions of laser intensity and electron density in a simulation box at $x = 51\mu m$. The solid curves in Fig. 4.8 show the analytical functions representing the best fits of $a(r)$ and $n(r)$. These analytical functions have been used in the numerical solutions

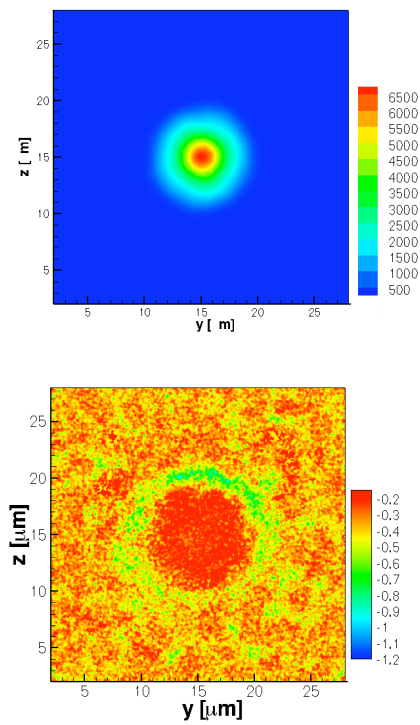


Figure 4.7 Contour plots of a) laser intensity and b) electron charge density at $x=51 \mu m$ for a single channel self-focusing.

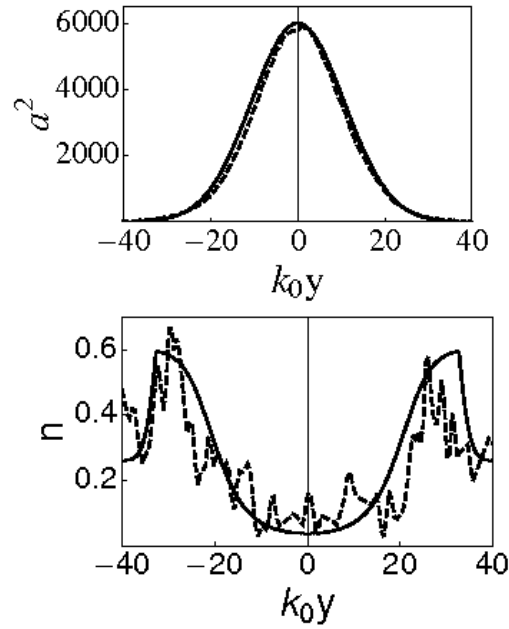


Figure 4.8 Distributions of laser beam intensity and electron density for single channel across propagation direction at $x=51 \mu\text{m}$ (the dashed curves). Solid curves show the analytical functions used for fitting.

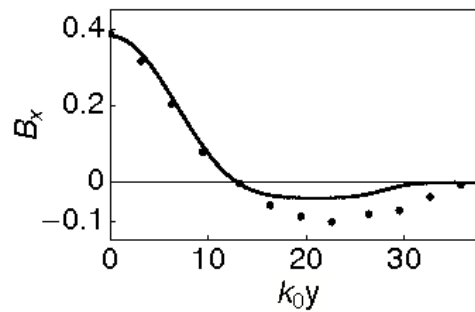


Figure 4.9 Comparison of the quasi-static magnetic field profiles for a single channel self-focusing from PIC simulation (dots) and by the analytical IFE approach (solid curve) for the intensity and density profiles shown in Figs. 4.7 and 4.8.

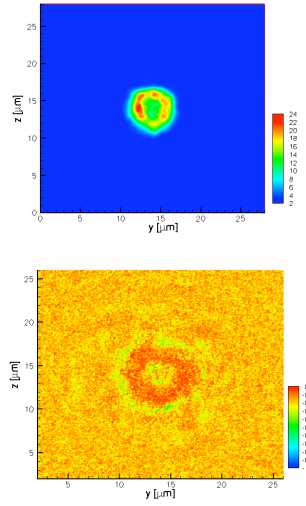


Figure 4.10 Contour plots of a) laser intensity and b) electron charge density at $x=18 \mu\text{m}$ for ring structure case.

of Eq. (4.7). In spite of two orders of magnitude higher laser intensity as compared to the previous example, the parameter $k_p r_0 / \sqrt{\gamma} \sim 1.5$. This is why, in agreement with the IFE theory, one may expect a similar magnetic field as in the first example that is demonstrated by Fig. 4.9. The points in Fig. 4.9 show the quasi-static magnetic field from PIC simulation and the magnetic field from Eq. (4.7) is shown by the solid line. The maximum magnetic field on the axis is 40 MG. The magnitude of the magnetic field and its radial distribution calculated from the theoretical model are very close to result of a PIC simulation.

4.2.2 Ring Structure of the Laser Pulse

To present qualitatively different example we chose the following set of parameters. The maximum initial intensity of the laser is $5 \times 10^{19} \text{ W/cm}^2$ ($a_{00} \simeq 4.3$). The initial FWHM of the laser intensity is $5 \mu\text{m}$ and the background plasma density is $0.09 n_{cr}$.

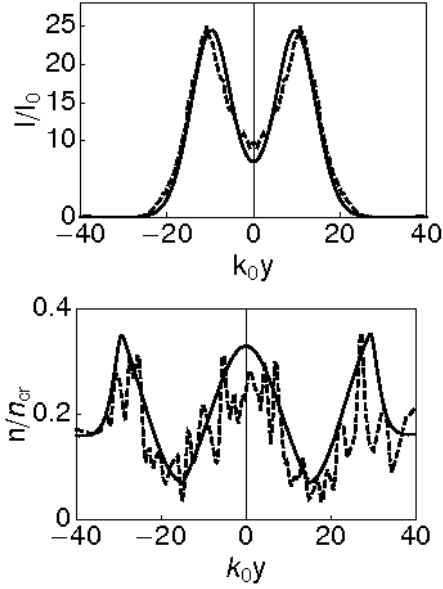


Figure 4.11 Distributions of laser beam intensity and electron density for ring structure across propagation direction at $x=18 \mu\text{m}$ (the dashed curves). Solid curves show the analytical functions used for fitting.

Ions are considered immobile. For these parameters relativistic self-focusing evolves towards the nonlinear state of the plasma and the laser pulse where they both display ring-like structures.

Figure 4.10 shows contour plots of the laser intensity and electron density at $x=18 \mu\text{m}$ in y - z plane. The laser intensity has a ring shape structure with a minimum on the laser beam axis. The electron charge density shows similar structure of a central electron filament surrounded by a partially evacuated ring region where the electron density reaches a minimum value of $0.05n_{cr}$.

Figure 4.11 shows the transverse profiles of the laser intensity and the electron density at $x = 18\mu\text{m}$ (dashed curves). Solid curves in Fig. 4.11 show analytical functions used to fit these radial distributions. As before, we have used these analytical

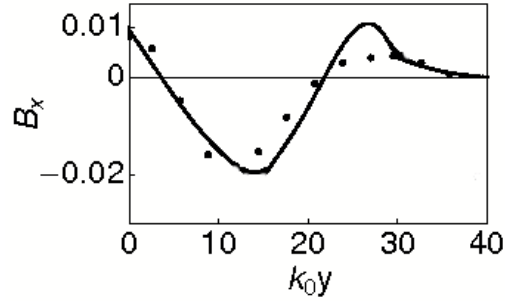


Figure 4.12 Comparison of the quasi-static magnetic field profiles for a case of the self-focusing leading to ring like field distribution obtained in PIC simulation (dots) and by the analytical theory of the IFE (solid curve) for the intensity and density profiles shown in Figs. 4.10 and 4.11.

fits of density and laser intensity to solve numerically Eq. (4.7).

Figure 4.12 shows the axial magnetic field (solid curve) which is the solution of Eq. (4.7). Dots show the quasi-static magnetic field found from PIC simulation. Here azimuthal nonlinear current have three layers where the middle azimuthal ring current flows in the opposite direction to the azimuthal current in the central filament and in the outer layer. Therefore the magnetic field has three local maxima: on the beam axis, inside the intensity ring and on the channel edges. Correspondingly, it changes twice its sign and goes to zero at $r \gg r_0$. The maximum of the magnetic field, $\simeq 2$ MG, is reached within the intensity ring. The oppositely directed inner and outer magnetic fields have approximately the same maxima $\simeq 1$ MG. This demonstrates that the self-focusing leading to the formation of a ring structure considerably suppresses IFE magnetic field generation as compared to B-fields obtained in the case of a single channel.

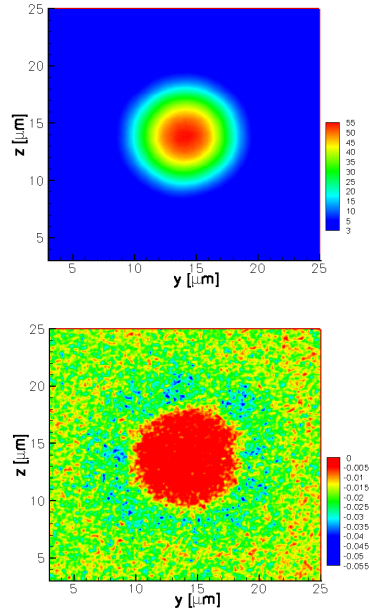


Figure 4.13 (Color online) Contour plots of a) laser intensity and b) electron charge density at $x=30 \mu\text{m}$ for the cavitation regime.

4.2.3 Channelling Regime

The complete electron evacuation in a laser channel takes place when the laser power P exceeds the critical power $P_{cr} = 16/n[\text{GW}]$. We have already observed in our simulations [27] that for plasma densities $n < 0.1n_{cr}$ full evacuation happens if $P > 1.1P_{cr}$. In this Section, we illustrate the IFE magnetic field generation for fully evacuated channel. The initial plasma density is $0.02n_{cr}$ and the laser power is 68 TW ($76P_{cr}$). The maximum initial intensity of the laser is $1.7 \times 10^{20} \text{ W/cm}^2$ ($a_{00} \simeq 7.8$). The initial FWHM of the laser intensity is $6 \mu\text{m}$. A fully evacuated stable channel is observed. The radius of the fully evacuated channel is $5.4 \mu\text{m}$. Figure 4.13 shows the laser intensity and the electron density in y - z plane at the distance $x = 30 \mu\text{m}$ along the direction of propagation. The laser intensity and electron density that are

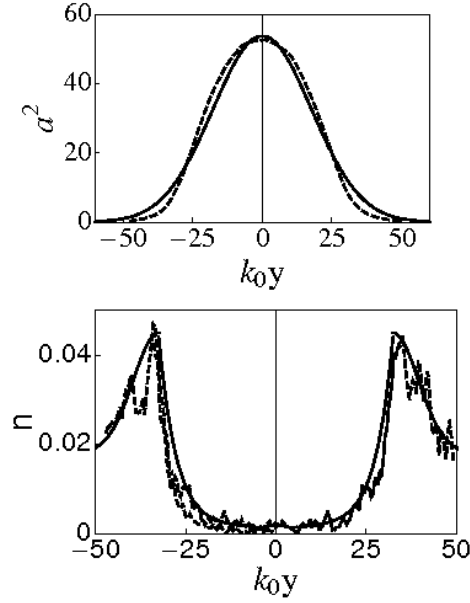


Figure 4.14 Distributions of laser beam intensity and electron density for cavitation regime across propagation direction at $x=30 \mu m$ (the dashed curves). Solid curves show the analytical functions used for fitting.

obtained from this cross section are shown in Fig. 4.14 by solid lines. The dashed curves were fitted by analytical functions in order to find the quasi-static magnetic field profile from Eq. (4.7). Figure 4.15 shows the solution to Eq. (4.7) (solid curve). The radial distribution of magnetic field was also found from PIC simulation by using the probes in y -direction at $x = 30 \mu m$. As before the probes record the time evolution of magnetic field as the laser light propagates in the plasma. After averaging over the fast laser period the spatial distribution of the quasi-static magnetic field is shown by dots in Fig. 4.15. The magnetic field profile is similar to the case of not fully evacuated channel (Sec. 4.2.1). However, the magnitude of the magnetic field is considerably lower because the effective electron density is much smaller and the relativistic factor γ reduces the magnetic field source (4.6). Magnetic field reaches a local maximum

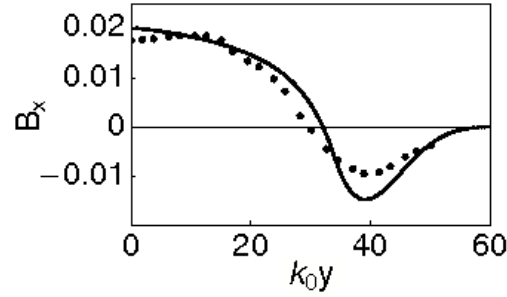


Figure 4.15 Comparison of the quasi-static magnetic field profiles for the cavitation regime calculated from the PIC simulation (dots) and by the analytical IFE theory (solid curve) for the intensity and density profiles shown in Figs. 4.13 and 4.14.

($\simeq 2$ MG) on the channel axis but it is larger at the channel edge where the nonlinear azimuthal current density is concentrated.

4.2.4 Time Evolution of the Magnetic Field

In this subsection we will give more examples of PIC simulation results and discuss comparisons with theoretical predictions for the generation of the magnetic field. In particular we will demonstrate that the growth of the magnetic field and its time evolution follows adiabatically changes in the radial profiles of the laser intensity and electron density. We have found that the axial B-field very quickly adjusts to changing plasma and laser conditions so we could use the stationary theory (4.7) at different moments in time to obtain good agreement with simulations at the same location but for quite different B-field configurations. This has been shown using PIC simulation results for the following parameters: the peak laser intensity is $1 \times 10^{20} \text{ W/cm}^2$ ($a_{00} \simeq 6$), a FWHM of the laser intensity is $5 \mu\text{m}$ and the initial plasma density is $0.1n_{cr}$. We expect that at this relatively large electron density and laser intensity

the pulse will undergo dynamical relativistic self-focusing and evolve from the central maximum filament to a ring structure and back at any particular position [27, 28]. Probes in such a run were located at $x=25 \mu m$ and collected the magnetic field profiles after the laser pulse propagated for 160 fs and 332 fs. At $t=160$ fs, Fig. 4.16, only one central channel is formed (similarly to the results of Sec.4.2.1). The single channel at 160 fs is not fully evacuated. The minimum density in the channel is $0.04n_{cr}$ and it has a radius of $\sim 3\mu m$. Further evolution of the laser filament gives rise to a ring formation (similarly to the results of Sec.4.2.2) at $t=332$ fs. The electron charge density shows a central electron filament enclosed by a partially evacuated ring where the minimum density is $0.02n_{cr}$. Figures 4.16, 4.17 show the transverse cuts in the x-y plane at $x=25 \mu m$ (dashed curves) at $t=160$ fs and $t=332$ fs, respectively. The solid curves in Figs. 4.16a,b and 4.17a,b show the analytical functions used for the best fits of $a(r)$ and $n(r)$ which subsequently were used in numerical solutions of Eq. (4.7). Figures 4.16c and 4.17c show the comparison of radial distribution of the axial magnetic field (solid curve) and the quasi-static magnetic field (dots) from PIC simulations for single channel and ring structure for $x=25 \mu m$ at 160 fs and 332 fs. Figures 4.16 and 4.17c show that the distribution of magnetic field adjusts itself to the radial profile of the laser intensity and density channel. Therefore we could conclude that even for complicated evolution of laser-plasma (single channel to ring structure) the changes in the magnetic field follows the evolution of the laser intensity and density channel.

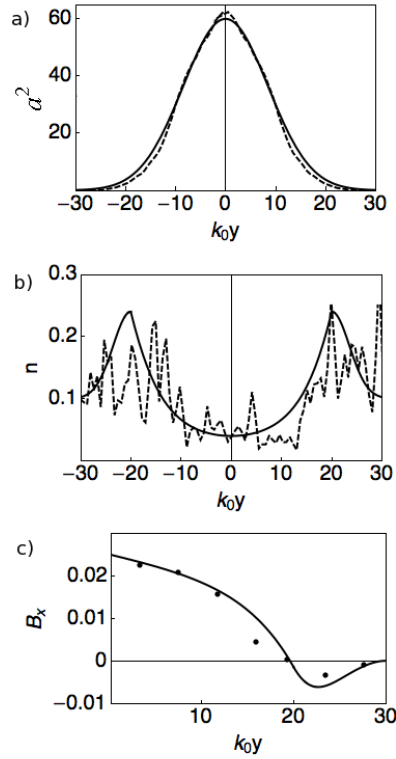


Figure 4.16 a) Distributions of laser beam intensity and b) Distribution of electron density across propagation direction at $x=25 \mu\text{m}$ at $t=160 \text{ fs}$. Dashed curves represent the lineouts from simulation and solid curves show the analytical functions used for fitting. c) Comparison of the quasi-static magnetic field profiles obtained in PIC simulation (dots) and the analytical theory of the IFE (solid curve) for the intensity and density profiles shown in (a) and (b).

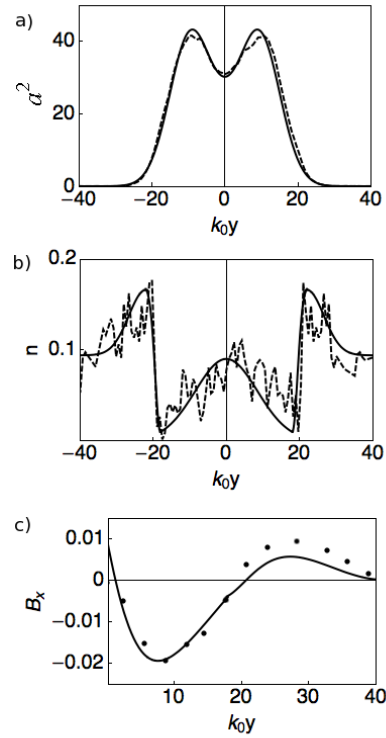


Figure 4.17 a) Distributions of laser beam intensity and b) Distribution electron density across propagation direction at $x=25 \mu\text{m}$ at $t=332 \text{ fs}$. Dashed curves represent the lineouts from simulation and solid curves show the analytical functions used for fitting. c) Comparison of the quasi-static magnetic field profiles obtained in PIC simulation (dots) and the analytical theory of the IFE (solid curve) for the intensity and density profiles shown in (a) and (b).

4.3 Discussion and Summary

We have studied by means of 3D PIC simulations and analytical theories magnetic field generation due to the IFE during the interaction of intense circularly polarized laser beams with underdense plasmas. We have investigated the regime of parameters corresponding to a relativistic self-focusing and laser pulse channeling. Depending on the laser input power and the electron background density, the plasma response during the relativistic self-focusing takes different forms. We have considered a single channel self-focusing without full evacuation of electrons, a ring like mode propagation of the laser light and density perturbation and, finally, a fully evacuated laser plasma channel. We have demonstrated for all these cases that magnetic field generation results from IFE and the quasi-stationary magnetic field spatial distribution is well approximated by the solution to the theoretical model based on Eq. (4.7). Thus, our numerical results have confirmed theories of Refs. [10, 12–14, 18] and are in a good agreement with approximate analytical results given by Eqs. (4.6)-(4.9). The onset and time changes of this B-field follow adiabatically variations of plasma density and laser intensity.

We have found that the magnetic field vector in plasma channels can change its direction and produce radial profiles with two or three different directions across the channel cross-section. This is quite different from the early theories of the IFE by circularly polarised laser light [2,6]. These early results [2,6] and the mechanism of the spin deposition from photons during the absorption of a circularly polarized light [16] result in an axial magnetic field along one direction. For the conditions considered in our simulations, we have not observed effects of the electron temperature [15, 18, 19] and a resonant absorption of the laser light by electrons executing betatron oscillations

in the channel [17].

Our results show that the magnetic field in a channel scales roughly as the averaged over the laser spot electron density. The B-field may reach several tens MG in magnitude for conditions of present high intensity experiments. Note that the changing direction of the generated magnetic field within a channel will complicate accurate measurements of the magnetic field using Faraday rotation technique and may result in the significant reduction of the measured magnetic field as compared to the true value of the field. Clearly ultra-relativistic intensities will lead to the inhibition of the nonlinear current (4.6) and will result in the laser light channeling. The two effects will decrease the magnitude of the magnetic field.

Bibliography

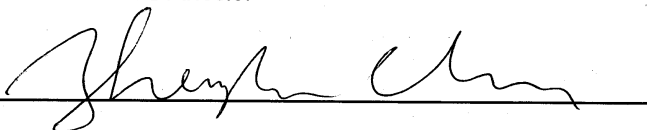
- [1] L. P. Pitaevskii, Zh. Eksp. Teor. Fiz. **39**, 1450 (1960) [Sov. Phys. JETP **12**, 1008 (1961)].
- [2] J. Deschamps, M. Fitaire, and M. Lagoutte, Phys. Rev. Lett **25**, 1330 (1970).
- [3] Y. Horovitz, S. Eliezer, A. Ludmirsky, Z. Henis, E. Moshe, R. Shpitalnik, and B. Arad, Phys. Rev. Lett **78**, 1707 (1997).
- [4] Y. Horovitz, S. Eliezer, Z. Henis, Y. Paiss, E. Moshe, A. Ludmirsky, M. Werdiger, B. Arad and A. Zigler, Phys. Lett. A **246**, 329 (1998).
- [5] Z. Najmudin, M. Tatarakis, A. Pukhov, E. L. Clark, R. J. Clarke, A. E. Dangor, J. Faure, V. Malka, D. Neely, M. I. K. Santala, and K. Krushelnick, Phys. Rev. Lett **87** 215004 (2001)
- [6] A. D. Steiger and C. H. Woods, Phys. Rev. A **5**, 1467 (1972).
- [7] A. Sh. Abdullaev and A. A. Frolov, Sov. Phys. JETP Letters **33**, 101 (1981).
- [8] Yu. M. Aliev, V. Yu. Bychenkov, and A. A. Frolov, Quasi-static magnetic fields generation in a plasma with strong electromagnetic radiation, In book: Nonlin-

- ear Theory of Strong Electromagnetic Wave-Plasma Interactions, Nova Science Publ., Ed. O.N.Krokhin 1993, p. 87.
- [9] T. Lehner, *Physica Scr.* **49**, 704 (1994).
- [10] V. Yu. Bychenkov and V. T. Tikhonchuk, *Laser and Particle Beams* **14**, 55 (1996).
- [11] Z. M. Sheng and J. Meyer-ter-Vehn, *Phys. Rev. E* **54**, 1833 (1996).
- [12] V. I. Berezhiani, S. M. Mahajan, and N. L. Shatashvili, *Physica Scripta.* **T75**, 280 (1998).
- [13] A. Kim, M. Tushentsov, D. Anderson and M. Lisak, *Phys. Rev. Lett* **89**, 095003 (2002).
- [14] A. A. Frolov, *Plasma Phys. Rep.* **30**, 698 (2003).
- [15] C. Y. Zheng, X. T. He and S. P. Zhu, *Phys. Plasmas* **12**, 044505 (2005).
- [16] M. G. Haines, *Phys. Rev. Lett* **87**, 135005 (2001).
- [17] I. Yu. Kostyukov, G. Shvets, J. Fisch and J. M. Rax, *Phys. Plasmas* **9**, 636 (2002).
- [18] Yu. M. Aliev, V. Yu. Bychenkov, M. S. Jovanović and A. A. Frolov, *J. Plasma Phys.* **48**, 167 (1992).
- [19] B. Qiao, S. P. Zhu, C. Y. Zheng and X. T. He, *Phys. Plasmas* **12**, 053104 (2005).
- [20] G. Shvets, N. J. Fisch and J. M. Max, *Phys. Rev. E.* **65**, 0464031 (2002).
- [21] G. Z. Sun, E. Ott, Y. C. Lee, and P. Guzdar, *Phys Fluids* **30**, 526 (1987).

-
- [22] A. B. Borisov et al., Phys. Rev. Lett. **68**, 2309 (1992).
- [23] V. I. Berezhiani, S. M. Mahajan, and N. L. Shatashvili, Phys. Rev. E. **55**, 995 (1997).
- [24] T. Lehner and L. di Menza, Phys. Rev. E **65**, 016414 (2002).
- [25] A. Kim, M. Tushentsov, F. Cattani, D. Anderson and M. Lisak, Phys. Rev. E **65**, 036416 (2002) **89**, 095003 (2002).
- [26] D. Romanov, V. Yu. Bychenkov, W. Rozmus, C. E. Capjack and R. Fedosejevs, Phys. Rev. Lett **93**, 215004 (2004).
- [27] N. Naseri, S. G. Bochkarev, W. Rozmus, Phys. Plasmas **17**, 033107 (2010).
- [28] N. Naseri and W. Rozmus, to be published.

Copyright Permission Slip

I hereby allow Neda Naseri to use the illustration/s listed paper, for the sole purpose of use in her Ph.D. thesis.

Signed: 

Date: 31 August 2009

Name (pls. print): Zhenglin Chen

Preferred copyright wording (if desired):

List of copyrighted material granted permission

Laser and Particle Beams 26, 147-155 (2008), Z. L. CHEN, C. UNICK, N. VAF AEI-NAJAFABADI, Y. Y. TSUI, R. FEDOSEJEVS, N. NASERI, P. -E. MASSON-LABORDE, AND W. ROZMUS, **Quasi-monoenergetic electron beams generated from 7 TW laser pulses in N₂ and He gas targets.**

Chapter 5

Quasi-Monoenergetic Electron Beams Generated From 7TW Laser Pulses in N₂ and He Gas Targets

5.1 Introduction

Laser electron acceleration [1] is a promising new approach for the development of next generation electron accelerators. GeV electron beam generation has been predicted by multiple simulations [2] and demonstrated in very recent experiments [3]. Such laser based accelerators might be expected to replace the traditional accelerators in the near future. Recent experiments have demonstrated the generation of high quality monoenergetic electron beams with different energies and fluxes, through

A version of this Chapter has been published. Z. L. Chen, C. Unick, N. Vafaei-Najafabad, Y. Y. Tsui, R. Fedosejevs, N. Naseri, P. -E. Masson-Laborde, and W. Rozmus, 2008. *Laser and Particle Beams*. 26: 147-155.

the interaction of laser pulses with powers higher than 10 TW with gases of hydrogen or helium [4–6]. Another recent experiment measured the acceleration gradient in the wakefield through a tomographic diagnosis method, which clearly shows the acceleration of 55 MeV electron beams from 5 MeV over a 200 μm interaction distance [7]. It is believed that the monoenergetic electron beams are generated in the wakefield or in cavitation bubbles in the electron density profile created by the laser fields when the plasma density ranges between $3 \times 10^{18} \text{ cm}^{-3}$ and $5 \times 10^{19} \text{ cm}^{-3}$ and the corresponding wavelength of the plasma waves is of the order of the laser pulse length [1,4–6]. A recent study confirms the possibility of modifying a long laser pulse in underdense plasmas to match the necessary conditions and driving the laser plasma interaction to the laser wakefield acceleration even if the initial laser and plasma parameters are outside the required regime [8]. The corresponding experiments show highly collimated, quasi-monoenergetic multi-MeV electron bunches generated by the interaction of tightly focused, 80 fs laser pulses in a high-pressure helium gas jet.

In this paper we report on measurements of electron generation from relatively high plasma electron densities of $5 \times 10^{19} \text{ cm}^{-3}$ and higher leading to bunches of electrons with energies typically ranging from 10 to 50 MeV for nitrogen targets and 25 to 100 MeV for helium targets. Such bunches would be consistent with injection of electrons from plasma oscillations breaking in the tail of the laser pulse and being injected into the wake of the main laser pulse as analyzed in 2D particle in cell modelling. The exact energy of the resultant electrons depends on the time of release of the electrons from the potential well accompanying the laser pulse which will vary from shot to shot. In addition, we show that on exceptional shots quasi-monoenergetic electron beams with energies of over 200 MeV can be generated both from helium and nitrogen gases. These very energetic electron beams have been produced with a

laser pulse intensity of approximately 7TW on the target, much less than laser powers employed in previous experiments [4–6], which have resulted in quasi-monoenergetic electron bunches over 100 MeV.

5.2 Experiment

Experiments were carried out using the 10 TW laser beamline at the Canadian Advanced Laser Light Source facility and the experimental set up is shown in Fig. 5.1. The 800 nm horizontally polarized laser pulses with energies up to 300 mJ were compressed to give 31 fs, 200 mJ pulses on target (~ 7 TW) and focused by a 150 mm focal length off-axis parabolic mirror in an f/6 cone angle into a $13 \mu\text{m}$ diameter spot on a supersonic gas jet. The resultant peak vacuum laser intensity is approximately $5 \times 10^{18} \text{ W/cm}^{-2}$. The gas jet was generated by a pulsed supersonic nozzle connected to a gas reservoir with backing pressure adjustable from 100 to 1200 psi. Different gases of helium, nitrogen and nitrogen mixed with hydrogen were employed in the experiments. The initial gas density profile was characterized with interferometric measurements.

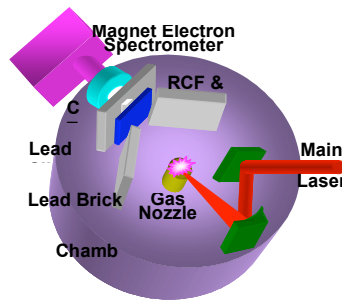


Figure 5.1 (Color online) Experimental set up.

A calibrated magnetic electron spectrometer was used to measure the electron energy spectrum on the laser axis in the forward laser direction, where a Lanex fluorescer screen (Kodak) was mounted after the magnet to record the electron beams. A sandwiched detector consisting of radiochromic film and CR-39 was used to measure the electron angular distributions in the forward laser direction on separate laser shots. It was entirely wrapped by a 20 μm thick aluminium foil to block the scattered laser light. Most ions with energies less than 10 MeV were stopped by the Al foil (confirmed by the signals on CR-39), allowing only energetic electrons and a weak x-ray background to hit the detector and radiochromic film.

5.3 Results and Analysis

In the experiments we scanned the nozzle location along the laser axis to change the position of the laser focus inside the gas jet density profile. An optimum position to generate the monoenergetic electron beams was found with the laser beam incident on the edge of the gas jet, depending on the specific gas density profile formed in the supersonic gas jet. The gas density profile was measured by the interferometer and shown in Fig.5.2. The optimum gas pressure for nitrogen and helium to generate the quasi-monoenergetic electron beams in the forward laser direction was about 360 psi and 900psi in these experiments, respectively. These correspond to electron densities in the interaction region of about $9 \times 10^{19} \text{ cm}^{-3}$ for nitrogen while about $5 \times 10^{19} \text{ cm}^{-3}$ for helium, assuming the charge states of nitrogen and helium are 5+ and 2+ [9], respectively.

Figure 5.3 shows the average energetic electron beam angular distribution in the forward laser direction, measured by RCF with the integration of 1640 laser shots

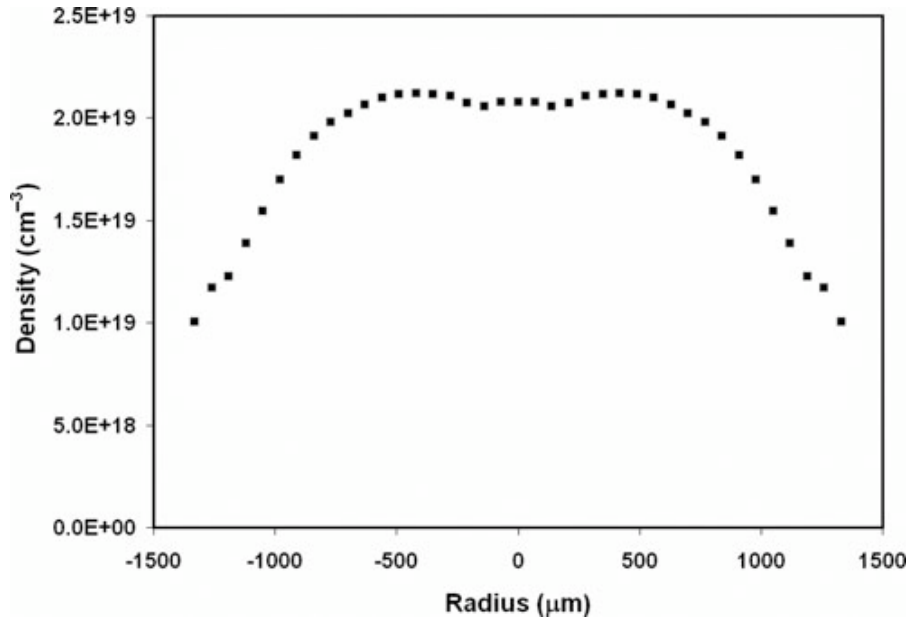


Figure 5.2 Typical gas density profile measured by the interferometer when nitrogen gas backing pressure was 1000 psi. The gas jet was generated by a supersonic nozzle which was connected to the gas reservoir with its pressure adjustable from 100 to 1200 psi. The profile shows a steep gradient at the edge and a good flat top in the center of the jet.

together. It is seen that the average angular dispersion of the electron beam is less than 10° . Estimates based on the RCF sensitivity to the electron beam shows that the number of electrons in the 10° beam is approximately 2.4×10^9 electrons per shot. Assuming an average electron energy in the range of 1 to 5 MeV (dominated by a low energy continuum), the conversion efficiency to electrons with energies greater than 100 keV (the approximate detector cut off energy) would be in the range of 0.2 to 1.0% (the laser energy incident at the target was about 180 mJ for this series of shots). From the PIC simulations, to be described later, an average electron temperature of the order of 1.4 MeV is observed for the bulk of the accelerated electrons. Figs. 5.4

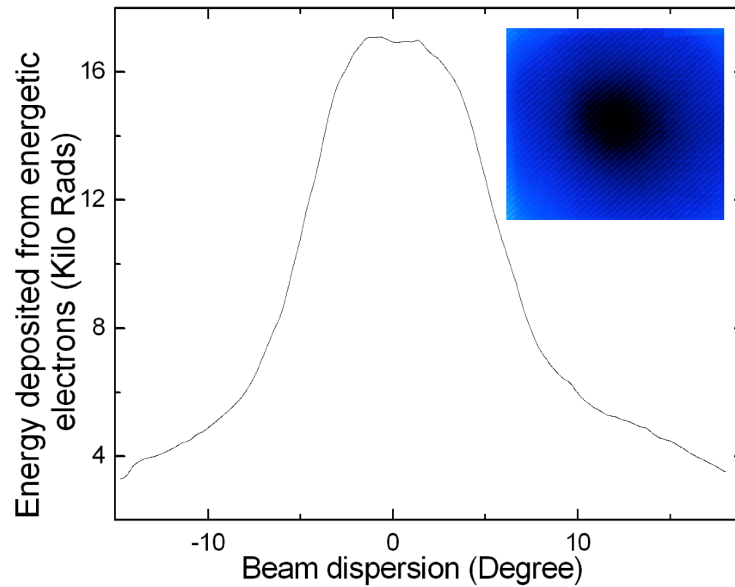


Figure 5.3 (color online) Energetic electron beam angular profile in the forward laser direction, integrated with 1640 shots when optimum conditions were adjusted to obtain mono-energetic electron beams. It was measured by RCF (inner frame) with nitrogen gas at about 360 psi and laser at the peak power. The laser beam forward direction is at 0° .

and 5.5 show the typical electron energy spectra (horizontal axis) with 1 dimensional spatial resolution (vertical axis) from both nitrogen and helium gases in the forward laser direction. For nitrogen alone and nitrogen mixed with 10% hydrogen, in most cases, one obtains multiple quasi-monoenergetic bunches with energies ranging from 12 MeV to 50 MeV, overlapping with a continuous energy spectrum as shown in Fig. 5.4 (a) and Fig. 5.4(b). For helium, in most cases, multiple electron bunches with energy ranging from 10 MeV to 100 MeV could be observed to overlap with a weak continuous energy spectrum, as shown in Fig. 5.5(a) and Fig. 5.5(b). The continuous background electron distribution in the spectrum appeared weaker for

helium than for nitrogen. Occasionally very bright energetic electron bunches were produced around 200 MeV, as shown in Fig. 5.4(c) for nitrogen and Fig. 5.5(c) for helium. Such exceptionally high energy shots, above 100 MeV, would occur on the order of less than 5% of the shots for nitrogen and on the order of about 40% of the shots for helium. The vertical angular spread of the electron bunches observed

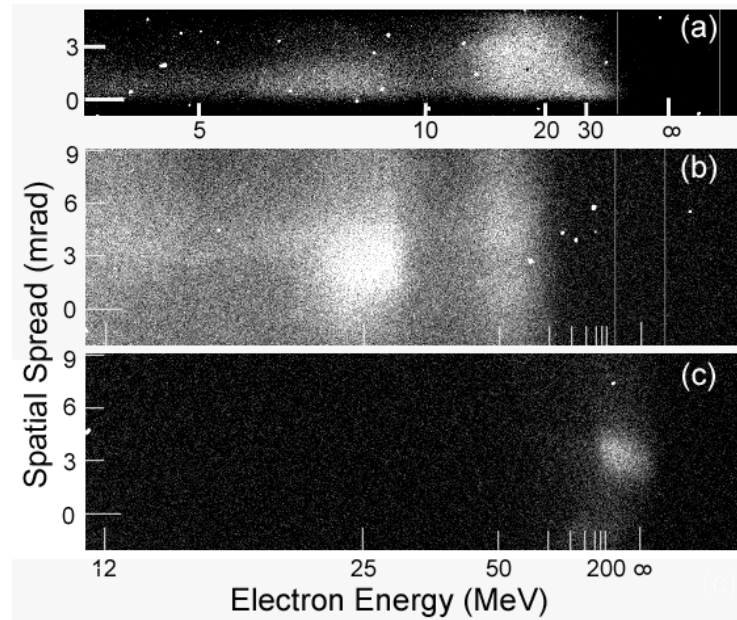


Figure 5.4 Typical single-shot electron energy distributions generated from nitrogen gas targets, measured by a Lanex fluorescent screen coupled to the electron spectrometer. Typical results are shown in (a) for pure N₂ at 500 psi backing pressure and (b) for N₂ with 10% H₂ at 360 psi. An example of an infrequent very high electron energy shot is shown in (c) for N₂ with 10% H₂ at 360 psi. The dashed lines show the location and width of the lead slit used to define the spectrometer entrance aperture.

is on the order of 3 to 6 mrad as seen in Fig. 5.4 and Fig. 5.5. This spread is much less than the average beam diameter of 10° observed from the radiochromic film as shown in Fig.5.3. The much broader beam diameter could correspond to

a much broader background of continuum electrons observed as a background in Figs. 5.4 and 5.5 which would also be dominated by lower energy electrons. The experiments show that the mono-energetic electron bunch generation from helium is somewhat more stable than that from nitrogen gas, especially when the laser is close to the peak power of 7 TW. The corresponding electron energy spectra derived

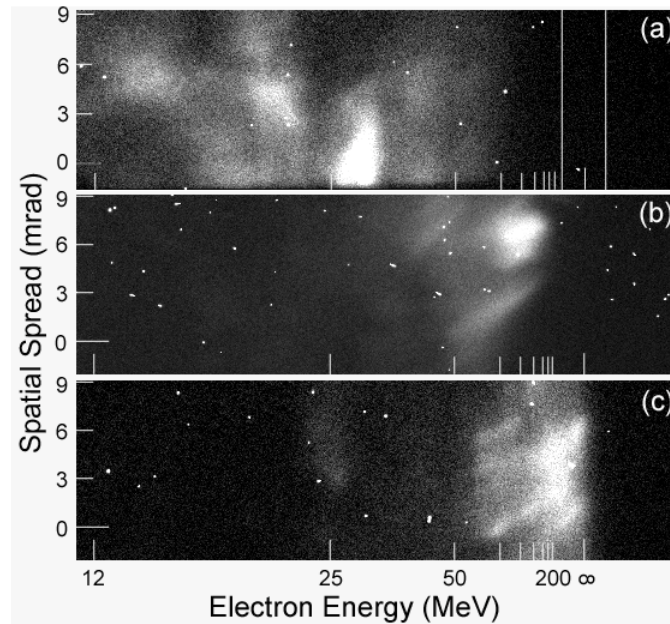


Figure 5.5 Typical single-shot electron energy distributions generated from helium gas targets, measured by a Lanex fluorescent screen coupled to the electron spectrometer. Typical results are shown in (a) and (b) for pure He at 900 psi backing pressure. An example of an infrequent very high electron energy shot is shown in (c) for He at 900 psi. The dashed lines show the location and width of the lead slit used to define the spectrometer entrance aperture.

from the magnetic electron spectrometer observations given in Figs. 5.4 and 5.5 are shown in Fig. 5.6. Fig. 5.6(a) and (b) show the two typical nitrogen spectra and helium spectra respectively. Fig. 5.6(a) shows that in most cases the electrons from

nitrogen gas are around 12 MeV to 50 MeV with several bunches overlapped on a continuous background. For helium gas similar single shot spectra appear with peaks in the range of 25 to 100 MeV as shown in Fig. 5.6(b). When the electron energy spectra are averaged over many shots a continuous quasi-Maxwellian distribution is observed. As shown in Fig. 5.6(c) The electron energy spectrum averaged over 20 shots from nitrogen gas shows a Maxwellian-like distribution, while for the helium gas jet it shows a plateau-like distribution with higher probability of generating energetic electron beams in energies ranging from 40 MeV to 140 MeV from the helium gas. In Fig. 5.6(d), the electron energy spectra from the exceptionally high energy single shots are given for nitrogen and helium gas. The total energy generated in the quasi-monoenergetic bunches from helium appears to be approximately 2 times higher than that from nitrogen gas, which indicates a better energy conversion to the energetic electron beams from the helium gas. Estimate shows that the number of electrons in the mono-energetic electron beam recorded by the Lanex screen in the electron spectrometer is of the order of 10^6 each shot. This is a small fraction of the total number observed on the radiochromic film per shot. However, in this case the energy per electron is much higher, typically on the order of 20 to 200MeV, depending on the shot and thus the total energy can still represent on the order of 2×10^{-5} to 2×10^{-4} of the incident energy. The radiochromic film views a much larger solid angle possibly integrating many such electron beamlets and also integrates all electron energies from 100keV upwards. For a quasi-Maxwellian electron energy spectrum the majority of electron energies observed by the radiochromic film will be in the low end of the energy spectrum.

The prepulse level in the current experiments was of the order of 2×10^{-5} for the nanosecond leakage pulse which arrives 8 ns prior to the main pulse and a picosecond

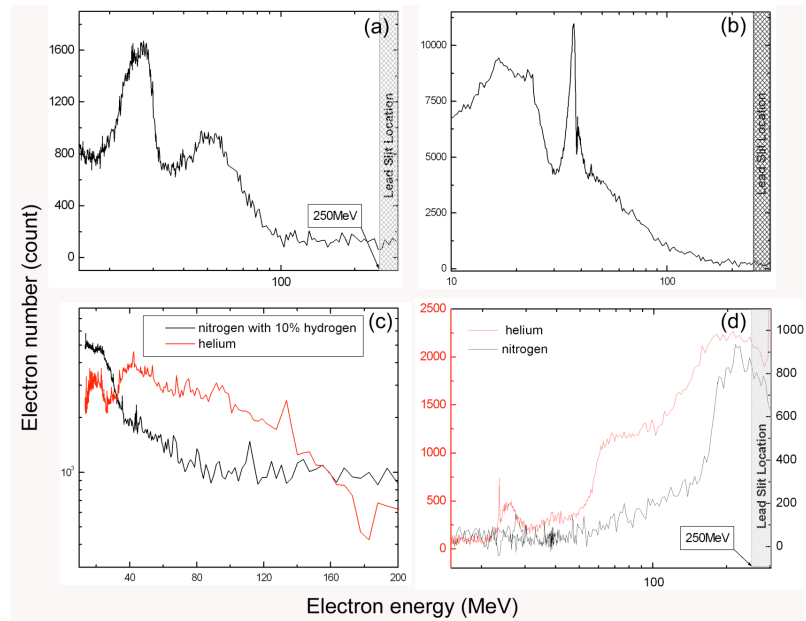


Figure 5.6 Electron energy spectra obtained from the magnetic spectrometer images: (a) from a single shot in nitrogen with 10% hydrogen at 360 psi (Fig. 5.4(b)) integrated over 1.6 mrad of angular spread vertically, (b) from a single shot in helium at 900 psi (Fig. 5.5(a)) integrated over 10.6 mrad of angular spread vertically, (c) by averaging 26 shots from nitrogen gas with 10% hydrogen at 360 psi and 19 shots from helium gas at 900 psi, integrated over 19.2 mrad of angular spread vertically and (d) energy spectra from the shots shown in Figs. 5.4(c) and 5.5(c) showing the infrequent high energy electron bunches for nitrogen with 10% hydrogen and helium respectively integrated over 1.6 mrad of angular spread vertically. The response of the system has been calculated based on the camera response and fluorescence efficiency of the Lanex screen giving approximately one count generated in the image for each incident electron with energy from 10 MeV to 200 MeV.

pedestal at 5×10^{-5} of the main pulse intensity 1ps prior to the peak of the main pulse and rising to 10^{-3} of the main pulse intensity at 0.4 ps prior to the main pulse. The effect of prepulse in enhancing the wakefield acceleration mechanism has already been pointed out by Giuletti *et al.* [20] and Hosokai *et al.* [19]. Our experimental prepulse levels are not too different from those of Hosokai *et al.* where clear guide channels were observed formed by the prepulse. For nitrogen gas this would be even more important due to the complex interaction of the femtosecond beam in ionizing the gas leading to filamentation and defocusing in some cases as previously observed by Fedosejevs *et al.* [9] and which also is complicated by ionization blue shifting of the leading edge of the laser pulse spectrum [21]. Thus, the preplasma formation may be required in order to stabilize the generation of quasi-monoenergetic electrons in nitrogen explaining the lower energies and numbers of electrons observed on average in the electron bunches compared to helium gas. The requirement for the formation of a preplasma for nitrogen may also explain why the optimum density for MeV electron generation was quite high since higher densities would breakdown, absorb more energy from the laser prepulse and form a channel with larger electron density gradients giving better guiding of the main pulse. Only rarely would a very long guide channel of just the right density conditions be formed at the right position for injection of the main beam to generate the 100 to 200 MeV electron bunches which would explain the low frequency of observation of the very high energy electron bunches.

The difference of the number of electrons measured by RCF and the Lanex fluorescent screen could be explained by a combination of the emission of multiple electron bunches in a given laser shot as well as a broad background of lower energy continuum electrons emitted in the forward direction. Noting the difference of the solid angle between RCF and Lanex, the 60 mm by 60 mm RCF was about 80 cm away

from the target while Lanex was about 920 cm away with a 1mm by 25 mm lead slit in the path about 355 mm from the target, as shown in Fig.5.1. The observation height on Lanex screen was only 18 mm, which is equivalent to 7 mm height on the slit. Thus only a small solid angle of the electron distribution function was observed by the Lanex screen in the electron spectrometer. Taking this solid angle difference gives a factor of the order of 100, which partially explains the ratio of the number of electrons measured by the two techniques. It is expected that more of the higher energy electrons which require acceleration over longer propagation distances will be in a small cone angle at the centre of the distribution and the lower energy electrons may be scattered over a larger cone angle. In addition, lower energy electrons (0.1-10 MeV) are not measured by the electron spectrometer but are still measured by the Radiochromic film. A larger number of such lower energy electrons may be produced by the interaction leading to the remaining factor of 10 larger Radiochromic film signal.

5.4 Modelling of the Results

We have performed 2D (2D3V) particle-in-cell (PIC) simulations with the relativistic multidimensional code Mandor [10] in support of the experiments. We have used parameters corresponding to the experimental conditions: the pulse has a Gaussian envelope with a FWHM diameter of $13 \mu m$, a time duration at half maximum $\tau_L = 30$ fs, and a peak irradiation intensity $4 \times 10^{18} W/cm^2$ ($a_0=1.4$, the normalized vector potential, $a_0 = eE_{pk}/mc\omega$, of the incident laser pulse). The ambient plasma electron density n_e is $5 \times 10^{19} cm^{-3}$, which corresponds to $n_e/n_c = 0.036$ with n_c the critical density for the laser wavelength $\lambda_0 = 0.8 \mu m$. The plasma is modelled as

a homogeneous slab of density n_e with a $40 \mu\text{m}$ long ramp on the entrance surface where the density increases linearly. In this 2D simulation, we used 16 particles per cell in $500\mu\text{m} \times 100\mu\text{m}$ box (7500×1500 cells). Ions are considered immobile. For our conditions, the laser pulse length ($c\tau_L \sim 9\mu\text{m}$) is greater than the electron plasma wavelength $\lambda_p \sim 2\pi c/\omega_p \sim 4.2\mu\text{m}$ or more accurately $\lambda_p = (2\pi c/\omega_p)(1 + (a_0^2)/2)^{1/4} = 5.4\mu\text{m}$, if we account for the relativistic increase of an electron mass. Fig. 5.7 shows the pulse intensity evolution as well as the 2D Fourier spectrum of the pulse at different locations inside the plasma. Fig. 5.8 shows the formation of the electron density wake behind the propagating laser pulse at different times and Fig. 5.9 shows the axial distribution of the electric fields and density profiles at two different times. Initially, around 180 fs, when the pulse reaches the top of the ramp and enters into

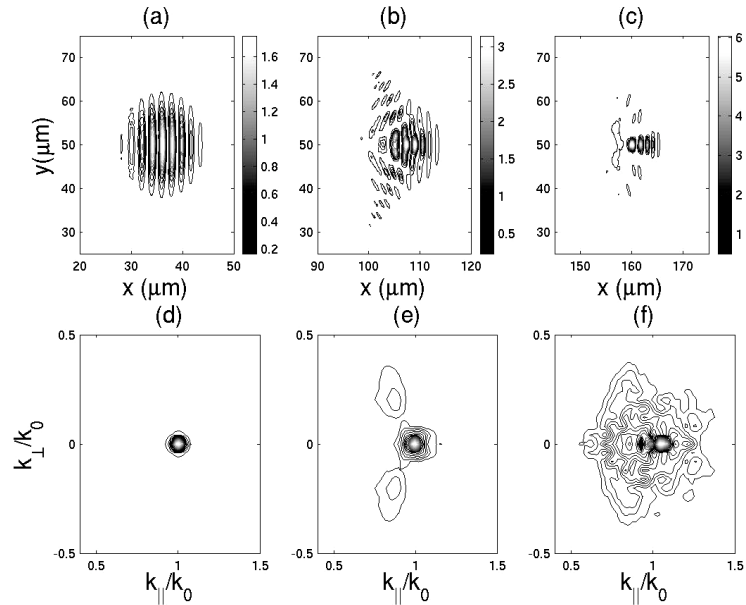


Figure 5.7 Laser pulse from 2D3V PIC simulations at different time a) $t=180\text{fs}$, b) $t=425\text{fs}$ and c) $t=606\text{fs}$, and 2D spectra of the laser pulse at the same times (d-f).

the homogeneous plasma, its shape is not modified, showing a total transverse size of around $20 \mu m$ and a longitudinal size of $18 \mu m$ [Fig. 5.7(a)]. But as can be seen in Fig.5.7(b), after $60 \mu m$ of propagation the laser pulse is modified by the stimulated Raman side-scattering instability, which can be identified by the presence of sidebands in the 2D spectrum [Fig. 5.7(e)]. This forward-scattering leads to a decrease of the light intensity in the focal region and contributes to a nonlinear pulse evolution which reduces the transverse size of the pulse. As shown in Fig. 5.7(b), after $60 \mu m$ of propagation the transverse size of the laser pulse is reduced by almost a factor 2. In addition, in our case, the power is many times the critical power for relativistic self-focusing, $P \sim 14 \times P_{crit}$ where $P_{crit} = 17 \text{ GW} \times n_e/n_c$ ($P_{crit} = 0.6 \text{ TW}$) for $\lambda = 800 \text{ nm}$ and $n_e = 5 \times 10^{19} \text{ cm}^{-3}$). As illustrated in Fig. 5.7(f), the spectrum of the pulse is broadened along the transverse and longitudinal directions, which corresponds to the relativistic self-focusing. The effect of self-focusing corresponds also to the increase of a_0 , by almost a factor 3 between the initial intensity and the maximum value observed during the simulation. During the propagation through the plasma, the laser pulse is also strongly modified along the longitudinal direction. This behavior was already observed and discussed in previous simulations [11]. The front of the pulse is steepened because of group velocity dispersion [11, 12], and it leads to pulse compression. At the same time the ponderomotive force of the leading edge accelerates electrons in front of the laser pulse leading to a density spike corresponding to an accumulation of electrons due to a snowplow effect. The front of the pulse experiences a frequency down-shift or a photon deceleration [13] due to the resultant gradient in index of refraction. The laser energy decreases while the photon number density is conserved therefore the front of the pulse experiences a frequency down-shift (photon deceleration) as can be seen in Fig. 5.9(b).

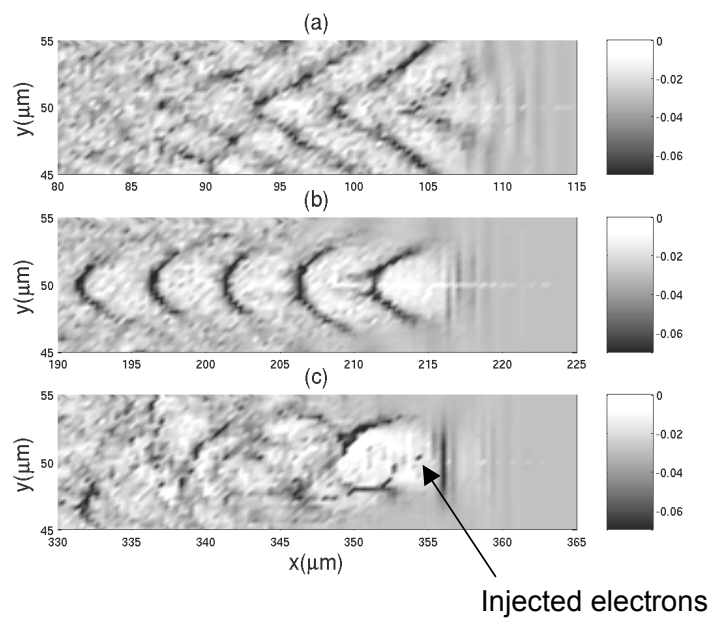


Figure 5.8 Electron density (in units n_c) for different times: a) $t = 425$ fs, b) $t = 790$ fs, and c) $t = 1273$ fs.

Fig. 5.7(f) shows the 2D spectrum of the pulse after 120 μm of propagation in the homogeneous density plateau, the part of the spectrum of the laser is strongly down-shifted to low value of k . As a result we observe a shortening of the pulse as shown in Fig. 5.7(c), where the length of the pulse is reduced by more than a factor 3. Shortening of a laser pulse during the propagation in an underdense plasma has already been measured in previous experiments [14] and attributed to a broadening of the laser spectrum due to relativistic self-phase modulation [15]. During the propagation of the pulse inside the plasma, a regular plasma wave is created [Fig. 5.8(b)] with a wavelength of almost 5 μm close to the estimated value with the relativistic corrections. These waves are curved due to the transverse wave breaking [16]. Between each wave, we observe a cavity, which contains a number of electrons [Fig 5.8(c), 5.9(a)]. A number of electrons are localized in a small spike in the front of the laser pulse [Fig 5.8(c)], represented by a small black streak). After 300 μm of propagation in the homogeneous density, the wave breaks and a number of trapped electrons are accelerated in the accelerating part of longitudinal field [Fig. 5.9(b)] (inside the first cavity). This breaking occurs for a maximum value of the longitudinal field E_x of almost 0.15 E_0 (with $E_0 = \omega_0 mc/e$), which is lower than the relativistic expression for the wave breaking (in the cold plasma approximation), given by $[2(\gamma_{ph} - 1)]^{1/2}(\omega_{pe}/\omega_0)E_0$ [17], which in our case, is around 0.5 E_0 , where γ_{ph} is the Lorentz factor associated with the plasma wave phase velocity, which for very underdense plasma is almost $(n_c/n_e)^{1/2}$. The energy spectrum of these electrons inside this cavity is illustrated in Fig 10. Just after the wave breaking, the energy spectrum shows 2 bunches of electrons with energies around 10 MeV and 20 MeV and finally it evolves to form only one peak around 30 MeV, close to the experimental results. The occasional electrons generated at 200 MeV are probably generated by the so-

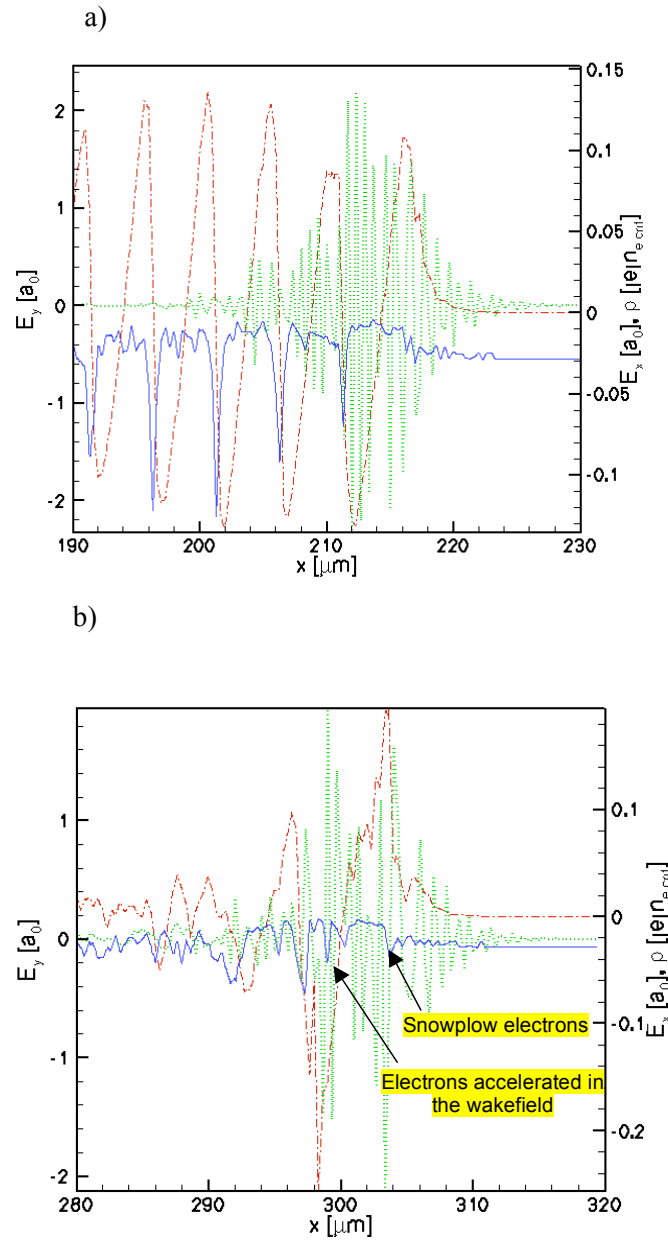


Figure 5.9 Lineouts of the longitudinal field, E_x , (dash-dot), laser field, E_y , (dotted) normalized to mc/e and electron charge density (solid line) normalized to critical density along the x axis at two different times: (a) at $t=849$ fs after propagating 180 microns in homogeneous plasma and (b) at $t=1091$ fs when the wake is already broken and trapped-electrons are accelerated in the accelerating field. The ponderomotive force also accelerates electrons in front of the laser pulse (snowplow).

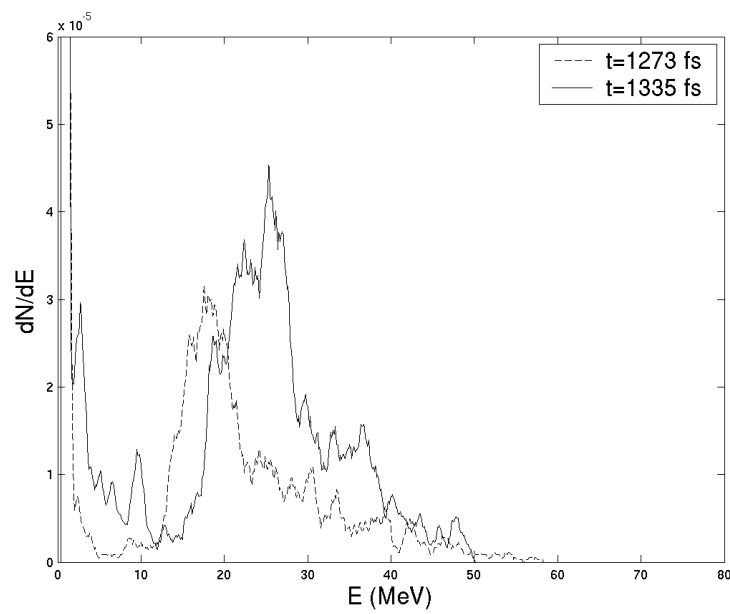


Figure 5.10 Energy spectrum of electrons inside the first wakefield cavity for 2 different times: 1273 fs and 1335 fs.

called mechanisms of the bubble acceleration [4–6], which is a wakefield acceleration in the highly nonlinear wave breaking regime. Several conditions are necessary for this mechanism. In particular, the transverse and longitudinal dimensions of the laser pulse must be not far from half of the plasma wavelength in order to be able to create this cavity (the bubble), void of electrons. A similarity theory recently introduced [18] gives a threshold for the power of the pulse in order to create this cavity: $P > P_{bubble} = [\tau(fs)/\lambda(\mu m)]^2 \times 30 \text{ GW}$. In our case we are initially well below this threshold. Nevertheless, it has been observed recently [8] that a long pulse which didn't fulfil this conditions, can evolve into a pulse which finally matches this threshold because of a shortening of its duration due to the self-modulation, leading to the observation of monoenergetic electron bunches. In our set of simulations, we observed the same evolution of the pulse, where at the end, its longitudinal size is reduced by more than a factor 3, as shown in Fig. 5.7(c). Such a reduction of pulse duration down to approximately 10 fs reduces the required power to $P_{bubble} = 4.7 \text{ TW}$. At the same time the pulse compression leads to the peak pulse power of 1.3 TW. Thus the interaction would not approach the full bubble regime in our simulations at the full background gas density. Thus, different starting conditions, such as a reduced density channel from a prepulse would be required in order to enter this regime.

Our modelling here is only 2D and it is well known that often 2D simulations underestimate the maximum electron energy [22], and fail to describe the self-focusing correctly, even if the physics and the interaction is correctly described. This self-focusing could lead to higher local laser intensities helping in the creation of bubble structures and leading to the generation of the higher laser energies.

In the present case there is another important factor limiting the maximum electron energy which can be generated. The high density in the present experiments

would lead to very short interaction lengths due to the rapid dephasing of the electron bunch and the laser wakefield. The standard scaling laws for wakefield acceleration [4] indicate that high energy electron production requires long interaction lengths at lower densities. Such long low density interaction lengths may occasionally be present in our experiment with the existence of a preplasma formed low density channel. The effect of preplasma created channels has already been reported in the literature in refs Hosokai and Giulietti [19,20], where a plasma cavity was formed by the prepulse picoseconds earlier than the main pulse. The main pulse was then guided by this cavity and formed a plasma channel, which significantly improved the generation of mono-energetic electrons. Our prepulse levels are similar to those reported by Hosokai et al. in their low prepulse case and thus we might expect similar conditions. The variability of the prepulse from shot to shot and the exacting conditions for the injection of the main pulse into such a channel would explain why only very few shots produce the high, 200 MeV, energy electrons occasionally observed.

In terms of the number of electrons observed in the PIC simulations, The energy contained in the 20 to 30 MeV bunch shown in Fig. 5.10 is $1.4 \mu j$ corresponding to 334,000 electrons. This is comparable to the number of electrons observed per electron bunch electron in the experiments of approximately 10^6 . Also, in the simulation almost all of the high energy electrons were accelerated in a cone angle of 20° . This is in approximate agreement with the observed cone angle of 10° (FWHM) for the electrons observed from the radiochromic film in the experiments. Thus, the overall number of electrons generated in the quasi-monoenergetic bunches and the overall directionality is in qualitative agreement with the experiment.

5.5 Conclusion

In conclusion, experiments show that quasi-monoenergetic electron beams with energies of the order of 10 to 50 MeV are generated in nitrogen and of energies of 25 to 100 MeV in helium for 7 TW laser pulses incident into plasma electron densities of 10^{20} cm^{-3} and $5 \times 10^{19} \text{ cm}^{-3}$ respectively. Occasionally electrons with energy over 200 MeV can be generated from laser pulses interacting with both nitrogen and helium gases. These very high energy electrons are most likely associated with the occasional occurrence of optimum preformed guide channels in the plasma due to the nanosecond and picosecond prepulse. Overall 2.5×10^9 electrons per shot were recorded in a cone angle of 10° (FWHM), while 10^6 electrons are generated in the quasi-monoenergetic bunches. 2D PIC simulations of the interaction of the laser pulse with plasma at an electron density of $5 \times 10^{19} \text{ cm}^{-3}$ indicates the production of a 20-30 MeV electron energy electrons consistent with majority of the shots in the experiment. During the interaction the pulse evolves through Raman scattering, self phase modulation and self-focusing leading to a shortening and increase in intensity. This allows the pulse to approach the threshold for the bubble regime as required for high energy electron acceleration. However, lower densities and longer interaction lengths would be required for the acceleration of electrons to very high energies of 200 MeV which would depend on the formation of a preplasma in the experiment. In the present experiments and simulations, a better understanding of the conditions required for quasi-monoenergetic electron pulses has been obtained and the possibility of controlling the generation of higher energy electrons through the use of optimum prepulses will be explored in the future.

Bibliography

- [1] T. Tajima and J. M. Dawson, *Phys. Rev. Lett.* **43**, 267 (1979).
- [2] A. F. Lifschitz, J. Faure, V. Malka, and P. Mora, *Phys. Plasmas* **12**, 093104 (2005).
- [3] W. P. Leemans, B. Nagler, A. J. Gonsalves, Cs. Toth, K. Nakamura, C. G. R. Geddes, E. Esarey, C. B. Schroeder, and S. M. Hooker, *Nature Physics* **2**, 696 (2006).
- [4] S. P. D. Mangles, C. D. Murphy, Z. Najmudin, A. G. R. Thomas, J. L. Collier, A. E. Dangor, E. J. Divall, P. S. Foster, J. G. Gallacher, C. J. Hooker, D. A. Jaroszynski, A. J. Langley, W. B. Mori, P. A. Norreys, F. S. Tsung, R. Viskup, B. R. Walton, and K. Krushelnick, *Nature* **431**, 535 (2004).
- [5] C. G. R. Geddes, Cs. Toth, J. van Tilborg, E. Esarey, C. B. Schroeder, D. Bruhwiler, C. Nieter, J. Cary, and W. P. Leemans, *Nature* **431**, 538 (2004).
- [6] J. Faure, Y. Glinec, A. Pukhov, S. Kiselev, S. Gordienko, E. Lefebvre, J.-P. Rousseau, F. Burgy, and V. Malka, *Nature* **431**, 541 (2004).
- [7] C.-T. Hsieh, C.-M. Huang, C.-L. Chang, Y.-C. Ho, Y.-S. Chen, J.-Y. Lin, J. Wang, and S.-Y. Chen, *Phys. Rev. Lett.* **96**, 095001 (2006).

-
- [8] B. Hidding, K.-U. Amthor, B. Liesfeld, H. Schwöerer, S. Karsch, M. Geissler, L. Veisz, K. Schmid, J. G. Gallacher, S. P. Jamison, D. Jaroszynski, G. Pretzler, and R. Sauerbrey, *Phys. Rev. Lett.* **96**, 105004 (2006).
- [9] R. Fedosejevs, X. F. Wang, and G. D. Tsakiris, *Phys. Rev. E* **56**, 4615 (1997).
- [10] D. V. Romanov, V. Yu. Bychenkov, W. Rozmus, C. E. Capjack and R. Fedosejevs, *Phys. Rev. Lett.* **93**, 215004 (2004).
- [11] C. D. Decker, W. B. Mori, K.-C. Tzeng and T. Katsouleas, *Phys. Plasmas* **3**, 5 (1996).
- [12] W. B. Mori, C. D. Decker and T. Katsouleas, *Phys. Rev. E* **50**, R3338 (1994).
- [13] F.S. Tsung et al. *Proc. Natl. Acad. Sci. U.S.A* **99**, 29 (2002).
- [14] J. Faure et al. *Phys. Rev. Lett.* **95**, 205003 (2005).
- [15] S.C. Wilks et al. *Phys. Rev. Lett.* **62**, 2600-2603 (1989).
- [16] S.V. Bulanov et al., *Phys. Rev. Lett.* **78**, 22 (1997).
- [17] A. I. Arkhiezer, R. V. Polovin, *Sov. Phys. JETP* **3**, 696, (1956).
- [18] S. Gordienko, A. Pukhov, *Phys. Plasmas* **12**, 043109 (2005).
- [19] T. Hosokai, K. Kinoshita, T. Ohkubo, A. Maekawa, M. Uesaka, A. Zhidkov, A. Yamazaki, H. Kotaki, M. Kando, K. Nakajima, S. V. Bulanov, P. Tomassini, A. Giulietti, and D. Giulietti, *Phys. Rev. E* **73**, 036407(2006).
- [20] A. Giulietti, P. Tomassini, M. Galimberti, D. Giulietti, L. A. Gizzi, P. Koester, L. Labate, T. Ceccotti, P. D'Oliveira, T. Auguste, P. Monot, and P. Martin, *Phys. Plasmas* **13**, 093103 (2006).

- [21] Y. M. Li and R. Fedosejevs, *Phys. Rev. E* **54**, 2167 (1996).
- [22] F. S. Tsung, W. Lu, M. Tzoufrsa, W. B. Mori, C. Joshi, J. M. Vieira, L. O. Silva, and R. A. Fonseca, *Phys. Plasmas* **13**, 056708 (2006)

Chapter 6

Summary

The main focus of this thesis was the investigation of the interaction of intense laser pulses with underdense plasma, channeling in 2D and 3D, magnetic field generation due to Inverse Faraday effect and electron acceleration.

6.1 Channeling in 2D Slab Geometry

In Chapter 2, self-channeling of circularly polarized laser light in 2D slab geometry was studied both in theory and simulation. The results of different 2D Particle-In-Cell simulations using Mandor [1] were illustrated and compared with analytical solutions. The stability of partially evacuated channels against transverse perturbations was studied. It was shown that partially evacuated channels are not stable against transverse perturbations. Excitation of surface wakes on the edges of the evacuated channels was addressed. The wavelength of surface waves was calculated in the highly relativistic regime. The wavelength of surface waves observed in simulation agreed well with theoretical estimates. We mentioned that if the ascending

part of the laser light is comparable with surface wave wavelength, the surface waves will be excited starting from the front part of the laser. The electrons will be heated and evacuation process will be terminated. At last, we showed that in higher plasma densities $n_0/n_{cr} \geq 0.1$, channeling solutions can not be reached. Transverse instability is more effective as the gain length is smaller for higher densities. The results of a sample simulation was shown.

6.2 Channeling in 3D

Self-channeling was studied in 3D in Chapter 3. 2D Self-focusing and channeling of the laser pulse in underdense plasma is different from 3D. Higher dimensionality is a very important factor, azimuthal instabilities can only be studied in 3D geometry. 3D simulations are more realistic. Self-focusing is stronger in 3D. Channeling process happens faster in 3D geometry. We studied channeling of the laser pulses in underdense plasma in theory and 3D simulations. The results of 3D simulations were shown and compared with theoretical solutions from standard models. Surface wake excitation was studied in 3D geometry. The wavelength of surface waves was calculated in cylindrical geometry and was compared with simulation results. We also studied the ring structure. They were also observed in 3D simulations, coexisting with main laser mode. The results of the simulations were compared with theoretical solutions. The stability of single channel solution and ring structure against symmetric perturbations was addressed. Approximate stability theory was used in studying asymmetric perturbation for ring structure. We showed that ring structure is not stable against azimuthal perturbations. Azimuthal perturbation can break the symmetry of the laser pulse. The results of a sample simulation was illustrated.

6.3 Magnetic Field Generation

Magnetic field generation due to inverse Faraday effect in interaction of circularly polarized laser pulse with underdense plasma was studied. The distributions of laser intensity and density channel were taken from cuts of 3D PIC simulations. Analytical functions which fit with the distributions were found and used to solve the differential equations to find the quasi-static magnetic field. The quasi-static magnetic field was also found in 3D simulations by using probes at different locations in the simulation box, recording the time evolution of the field and finally averaging over a laser period. The two magnetic fields were compared for different cases. We concluded that the strength of the quasi-static magnetic field depends strongly on the shape of the density channel and the depth and width of the channel.

6.4 Electron Acceleration

Electron wakefield acceleration was studied using 2D PIC code. The results of the simulations supporting the experimental results were presented. The energy the electrons gained in the process was peaked at 20-30 MeV close to the experimental results. However in the experiment higher energies were also measured. The occasional electrons generated at 200 MeV are probably generated by the so-called mechanisms of the bubble acceleration. In our case we are initially well below the threshold for bubble regime. Nevertheless, it has been observed that a long pulse which did not fulfill the bubble regime threshold condition, can evolve into a pulse which finally matches this threshold because of a shortening of its duration due to the self-modulation, leading to the observation of monoenergetic electron bunches.

Bibliography

- [1] D. Romanov, V. Yu. Bychenkov, W. Rozmus, C. E. Capjack and R. Fedosejevs,
Phys. Rev. Lett **93**, 215004 (2004)